Contrasting glacier behaviour, and methods for monitoring glacier change, in the northern Canadian Arctic Archipelago

Dorota MEDRZYCKA

Thesis submitted to the Faculty of Graduate and Postdoctoral Studies
in partial fulfilment of the requirements for the degree of
Doctorate of Philosophy in Geography

Department of Geography, Environment, and Geomatics
Faculty of Arts, University of Ottawa
Ottawa, Ontario, Canada

ABSTRACT

Glaciers are generally considered to be important indicators of climate, but the variability in glacier behaviour observed across the Canadian Arctic Archipelago (CAA) indicates that not all ice masses respond in the same way to external forcing. This thesis presents detailed studies on the contrasting behaviour of two ice masses with widely different characteristics: Good Friday Glacier on western Axel Heiberg Island, a large marine-terminating outlet glacier which has undergone an uninterrupted advance over the last seven decades, and Bowman Glacier in Tanquary Fiord, northern Ellesmere Island, a small mountain glacier destined to disappear within a few decades.

Changes of these glaciers are determined from field and remote sensing observations, with a particular focus on digital photogrammetry techniques applied to recent and historical aerial photography for generating topographic datasets. Strategies are presented for the flexible acquisition of high-resolution topographic data in challenging field conditions, typical of high arctic glacier environments, and a workflow is described for deriving detailed surface reconstructions, yielding centimetre-scale digital elevation models and orthomosaics of a small ice mass in the CAA. This work also demonstrates the application of current digital photogrammetry processing for deriving surface elevation information from historical aerial photography from the 1950s, enabling direct comparison with recent topographic products to calculate glacier volume change and geodetic mass balance over decadal timescales.

Observations on Good Friday Glacier show a continuous advance totalling $>$9 km since the late 1940s, representing a 5% increase in glacier area over a total basin size of 800 km^2, and ice flow rates higher than on most other marine-terminating glaciers in the CAA. In contrast, since 1959, Bowman Glacier lost 78% of its area and 60% of its volume and currently covers only 0.61 km^2. Projecting the trend in ice extent and surface thinning observed over the last decade indicates that Bowman Glacier will likely disappear entirely between 2030–60. While the ongoing advance of Good Friday Glacier is out of sync with current climatic conditions, changes at Bowman Glacier are in agreement with the dominant regional trend of accelerated mass loss and glacier retreat.

PREFACE

Thesis content

This doctoral thesis is written in article format and consists of an introductory chapter, three manuscripts as listed below, and a concluding chapter which synthesises the research presented in the articles and provides an overall summary and analysis. The complete reference list at the end includes all works cited in the thesis. The first manuscript below has been published in Journal of Glaciology, while the other two will be submitted to the listed journals shortly after deposition of the thesis.

1 **Medrzycka D**, Copland L, Van Wychen W, Burgess D (2019) Seven decades of uninterrupted advance of Good Friday Glacier, Axel Heiberg Island, Arctic Canada. Journal of Glaciology, 65(251), 440-452. doi:10.1017/jog.2019.21

2 **Medrzycka D**, Copland L, Thomson L, Smeda B, Kochtitzky W (*in prep*) Strategies for mapping remote glaciers using photogrammetry techniques in suboptimal conditions. ISPRS Open Journal of Photogrammetry and Remote Sensing

3 **Medrzycka D**, Copland L, Noël B (*in prep*) Rapid demise of a small glacier in the Tanquary Fiord region, Ellesmere Island, Canadian High Arctic. Journal of Glaciology

Author contributions

D Medrzycka is the primary author for all three manuscripts and performed the vast majority of the field data collection and data processing, worked out most of the methods, developed the photogrammetry workflow, performed the analysis and interpretation of results, and prepared the three manuscripts. L Copland provided editorial feedback for all manuscripts and the thesis as a whole. Specific contributions of co-authors are as follows:

1 W Van Wychen processed the RADARSAT-1/2 data and derived ice surface velocities from speckle tracking. D Burgess provided access to the RADARSAT-2 data through Natural Resources Canada and the Canadian Space Agency. All co-authors contributed to the final manuscript with revisions and edits, as well as two anonymous reviewers from the Journal of Glaciology.

2 L Copland, L Thomson, and B Smeda assisted with data collection and logistics in the field. W Kochtitzky contributed to data processing.

3 L Copland assisted with data collection and logistics in the field, and was responsible for the acquisition, processing, and interpretation of ground penetrating radar data. B Noël undertook modelling of RACMO2.3 climate and surface mass balance data.

Contents

List of Figures

List of Tables

ACKNOWLEDGEMENTS

This work, and in general the last seven (plus) years, have been supported by a multitude.

To my supervisor Dr. Luke Copland First and foremost, biggest thanks to you Luke! I've said it countless times: I couldn't have asked for a better supervisor. You've been brilliant! From the most lavish praise: "This version is much better than the previous one", to the harshest criticism: "Hmmm...", accompanied by slow head tilt and squint (translating into: "Yeah, I don't think so"), you've been an incredible resource and your feedback and constructive criticism instrumental in helping make some sense of the confusion.

We didn't always agree, but I was always given the freedom to roam and follow an idea, even a seemingly pointless one. I may have a tendency to get overly excited (perhaps shooting slightly too high), and I'm incredibly grateful for your patience and willingness to let me explore while yanking me back on track whenever I got too distracted.

Thank you for being a strong proponent of 'life before science' (i.e., it's ok to have a weekend), for understanding everyone's particular limitations, and for pushing us to find some balance with life outside the dark depths of the Ottawa lab and long Yellowknife winter nights. Thank you for all the trips, for the chance to run around glaciers all over the world, for always being on top of things and watching out for the small details making sure no deadlines or opportunities were missed. Very much looking forward to doing more science and working with you as a colleague!

To colleagues and collaborators I would like to thank all who have collaborated to the projects in this thesis: Dr. Wesley Van Wychen, Dr. Dave Burgess, Dr. Laura Thomson, Braden Smeda, Will Kochtitzky, Dr. Brice Noël, and to those beyond: Dr. Christine Dow, Dr. Ellie Bash, Brittany Main, and Moya Painter. Special thanks to my committee members for their time and contributions to the final version of this thesis: Dr. Dave Burgess, Dr. Denis Lacelle, Dr. André Viau, and external examiner Dr. Brian Menounos.

To funding and permitting agencies This work was supported by the Natural Sciences and Engineering Research Council of Canada, Fonds de Recherche du Québec – Nature et Technologies, Ontario Graduate Scholarship, ArcticNet Network of Centres of Excellence Canada, Northern Scientific Training Program, Polar Continental Shelf Program, Canada Foundation for Innovation, Ontario Research Fund, and the University of Ottawa. Thanks are due to the Nunavut Research Institute and the communities of Resolute Bay, Grise Fiord, Pond Inlet, and Pangnirtung for permission to undertake fieldwork on Axel Heiberg, Ellesmere, Bylot, and Baffin islands, as well as Kluane First Nation and Parks Canada for the work in Kluane National Park.

To my LCR lab mates Starting with the original few: Laura Thomson, Nicole Schaffer, Wesley Van Wychen, Adrienne White. Thank you for your invaluable insight into the inner-workings of PhD life, particularly at the beginning, and once the third year blues hit. To those who followed (roughly in order of appearance): Larissa Pizzolato, Abby Dalton, Brittany Main, Danielle Hallé, Claire Bernard-Grand'Maison, Alison Cook, Braden Smeda, Adam Garbo, Will Kochtitzky, Moya Painter, and Gabriel Partington. Many thanks for sharing the ups and downs, the laughs and rants, and for being there to talk things out. Thanks to you Luke for assembling such a fine group of people!

To all the folks I've crossed paths with in the field over the years You lot have been the instrumental in me preserving (some of) my sanity, shedding some of that restlessness, and gathering fresh motivation to plough on through the long months of staring at a screen.

To the Expedition Fjord family, most notably: Laura Thomson and Chris Omelon. While there is no other place like the Villa by the (Colour) Lake, you guys are what made all those field seasons truly fantastic. Thanks for the countless hikes to/from White Glacier, for all the chats, and for the most excellent jokes!

To the St. Elias field team: Luke Copland, Christine Dow, Ellie Bash, Brittany Main, Moya Painter, and Gabriel Partington. Thank you for constantly bringing me back to these parts and giving me heaps of extra fieldwork to keep me busy outside of the PhD. It's been an honour, and such tremendous fun!

To the Kluane Lake Research Station (KLRS) staff: Harry Penn, Matt Ayre, Bob Reich, and Kristina Miller. Thank you for the endless supply of coffee, for giving me a home away from home, a place to break the routine and escape the darkness of solitary work.

To the excellent folks from Icefield Discovery: Andy and Sian Williams, Lance Goodwin, Sherpal Singh. To the most brilliant heli pilots: Mike Taekema, Nadia Bosman, Mat Stoeckle. It is an understatement, that none of this work would have been possible without you guys.

To wrap it all up, saving the best for last Laura, Ellie: You're both absolutely brilliant people! Thank you for doing all the science with me, and for getting me excited to do more. Thanks also for being real, for letting me know I'm not alone, and for all the encouragements along the way. Inge, dude: Thank you for always calling me out on my BS. Your wisdom is unparalleled. Always wishing you were here. Karine: Thank you for popping back into my life after all these years and bringing the little family along. You're a breath of fresh air! Mat: Thanks for the chats and for a truly excellent time.

Mum, Dad, Little Brother: Thank you for tolerating me over the past years (and all those prior), for your continued support, and for believing in me even when it seemed I had lost my way. Yes, I'm finally done with school.

Niels: Ouf, sorry it took so long! Thank you for picking up all the extra slack, for digging deep and finding the patience to endure this long process through multiple dead ends and countless delays. I'm forever grateful for your support, for reminding me of what's important whenever I didn't have the wisdom to see it myself.

Lastly, as per tradition, thanks to the dogs. First came Piqsiq, borrowed from Laura, now followed by our own northern special Runa (aka mini Piqsiq). No need for more words, you guys don't speak human anyways.

1

Introduction

The northern Canadian Arctic Archipelago (NCAA), including Ellesmere, Axel Heiberg, Devon, and Melville islands, has a total glaciated area of 105,000 km^2, about 15% of global land ice area outside of the Greenland and Antarctic ice sheets (RGI Consortium, 2017). With few exceptions, glaciers and ice caps in the region have been retreating over the 20th century (Dowdeswell, 1995; Koerner, 2005). Following a period of cooler conditions in the 1970–80s, annual mass balance estimates have become increasingly negative, particularly since the start of the 21st century (Gardner et al., 2011; Lenaerts et al., 2013; Thomson et al., 2017; Noël et al., 2018; Hugonnet et al., 2021). Modelled average surface mass balance losses for the NCAA nearly tripled between 1958–95 and 1996–2015, increasing from -8.4 ± 11.0 Gt a^{-1} to -24.7 ± 11.0 Gt a^{-1} between the two periods (Noël et al., 2018). This sharp increase in mass loss is in direct response to warmer summer air temperatures and longer melt seasons enhancing surface runoff (Gardner et al., 2011; Sharp et al., 2011; Mortimer et al., 2016; Noël et al., 2018). In the CAA, most mass is lost through surface ablation and runoff, and dynamic discharge through iceberg calving represents a lesser fraction of the regional mass budget, although it remains an important mechanism of ice loss for specific glacier basins (Van Wychen et al., 2014, 2016, 2021; Millan et al., 2017). Of 211 marine-terminating glaciers in the NCAA, $>$90% experienced overall terminus retreat between 1958–2015, with a notable increase in retreat rates coinciding with increased surface mass balance losses over the last two decades (Cook et al., 2019; Kochtitzky and Copland, 2022). Meanwhile, small land-terminating glaciers have been experiencing the highest relative area losses, and several of the smallest ice masses ($<$1 km^2) have disappeared entirely since the 1960s (Thomson et al., 2011; Sharp et al., 2014; Serreze et al., 2017; White and Copland, 2018; Curley et al., 2021).

Superimposed on a regional trend of glacier retreat and gradual slowdown in response to sustained negative mass balance conditions, is a spatial and temporal variability involving both steady and unsteady ice flow regimes, with sometimes neighbouring ice masses exhibiting contrasting behaviours (Van Wychen et al., 2016, 2021). Glacier fluctuations, including changes in area and volume, primarily occur in response to climate forcing, but the magnitude and timing of the response is complicated by topographic factors and glacier geometry (size, slope, elevation range, etc.), which dictate the sensitivity and response time of individual glaciers to a change in climate (Furbish and Andrews, 1984; Jóhannesson et al., 1989; Oerlemans et al., 1998). This relationship can account for some of the spatial variability in glacier behaviour in the CAA, including the particularly rapid shrinkage of small isolated glaciers and icefields (e.g., on northern Ellesmere Island; White and Copland, 2018), and perhaps the continued

advance of a few large outlet glaciers draining the major ice caps (e.g., on western Axel Heiberg Island; Van Wychen et al., 2021). A few glaciers have also been shown to undergo significant (>20 m a^{-1}) interannual velocity variations accompanied by important changes in terminus position and ice thickness (Short and Gray, 2005; Sharp et al., 2014; Van Wychen et al., 2014, 2016, 2021; Dalton et al., 2022). While some of this variability in ice motion can be attributed to surging behaviour (Hattersley-Smith, 1969b; Müller, 1969; Copland et al., 2003), some instabilities are likely related to tidewater glacier dynamics, including both longer term advance/retreat cycles characteristic of marine-terminating glaciers, and transient pulses resembling short-lived speed-up events (Van Wychen et al., 2016, 2021; Millan et al., 2017; Dalton et al., 2022). Glacier geometry and basal topography also play a major role in controlling the dynamics of marine-terminating glaciers, modulating the timing and magnitude of changes in ice dynamics (Pfeffer, 2007; Bartholomaus et al., 2016; Catania et al., 2018; Frank et al., 2022).

These contrasting behaviours highlight the non-linear response of glacier dynamics to a common regional climate forcing, and the role of glacier specific factors in modulating ice flow. The overwhelming trend of glacier retreat in the NCAA implies that glaciers are out of equilibrium with current climate, but the variability in observed rates of change needs to be better assessed to understand the range of asynchronous glacier behaviours on a regional scale, with detailed studies on individual glaciers required to better understand the factors driving this variability. This requires observations on decadal timescales to place recent glacier fluctuations in the context of long-term trends of glacier change. An accurate baseline of past and recent glacier changes is also needed for calibrating and validating numerical models in order to improve projections of future change in an evolving climate.

1.1 BACKGROUND

Climate sensitivity and response time

Following a perturbation in climate, glaciers generally adjust towards a new steady state geometry, and glacier length fluctuations provide a general indication of changes in mass balance conditions in response to a change in temperature and/or precipitation (Oerlemans, 2005; Leclercq and Oerlemans, 2012). The magnitude and timescale of the response, however, varies depending on glacier climate sensitivity and response time, both strongly related to glacier hypsometry (i.e. distribution of area with elevation), and mass balance gradient (mass balance rate of change with altitude), along the glacier profile. Climate sensitivity refers to the relative change in specific mass balance in response to a shift in climate, whereas response time is essentially the time required for a glacier geometry to adjust and revert to a steady-state profile following a change in mass balance conditions (Furbish and Andrews, 1984; Jóhannesson et al., 1989; Bahr et al., 1998; Raper and Braithwaite, 2009; Cuffey and Paterson, 2010).

Changes at glacier margins and terminus advance/retreat are only part of the response to changes in climate, as a shift in mass balance regime implies a change in mass distribution patterns along the glacier profile, which can then lead to changes in ice surface elevation (and associated ice thickness), surface slope, and ice flow regime. Conversely, evolving glacier geometry affects mass balance characteristics through elevation mass balance feedbacks (Cuffey and Paterson, 2010). In terms of hypsometry, glaciers with the bulk of their area close to the mean equilibrium line altitude (ELA) are particularly likely to fluctuate, as relatively small changes in ELA can shift the accumulation area ratio (AAR) enough to transition from a positive to a negative mass balance regime (Furbish and

Andrews, 1984; Cuffey and Paterson, 2010). In cases where the ELA rises above the highest point of a glacier and removes the accumulation zone so that net mass loss occurs over the entire surface, the change is likely to result in the long-term disappearance of the glacier. Large outlet glaciers covering large elevation spans with sizeable accumulation areas at high altitude are comparatively less sensitive, as a similar rise in ELA causes the terminus to retreat to higher elevation where it stabilises due to cooler conditions and lower ablation rates. At the same time, continued warming enhances rates of ablation and promotes thinning, which increases the balance gradient (Cuffey and Paterson, 2010). An increase in mass flux which triggers a terminus advance will have a similar effect as more ice is pushed further into the ablation zone, which ultimately increases the balance gradient and lowers response time (Bahr et al., 1998).

Glaciers in temperate climates with higher precipitation will typically be more sensitive to ELA perturbations and have shorter response times than polar glaciers in cold and dry environments due to their higher balance gradients and increased mass flux (Oerlemans et al., 1998; Raper and Braithwaite, 2009). The regional climate in the NCAA is characterised by relatively low annual precipitation ($<$400 mm a^{-1}), with little interannual variability (Koerner, 1979). Regional patterns of ELA broadly reflect regional precipitation gradients, depending on the influence of local topography and distance to a moisture source. Precipitation is highest along coastlines facing Baffin Bay and the Arctic Ocean, and decreases with increasing elevation and distance inland (Koerner, 1979). However, it is well established that mass balance fluctuations in the region are primarily driven by changes in summer temperatures and glaciers show a comparatively low sensitivity to precipitation (Koerner, 2005; Gardner et al., 2011). There is a general consensus that, in a given climate, glaciers with steep slopes will have shorter response times, and as steep glaciers also tend to be smaller, shorter, and thinner, response time typically decreases with glacier size (Bahr et al., 1998; Oerlemans et al., 1998; Raper and Braithwaite, 2009). Based on the volume scaling approach, the response time is approximately proportional to the ratio of ice thickness to the rate of ablation at the glacier terminus (Jóhannesson et al., 1989), which gives typical response time estimates of 150–1000 years for polar glaciers and ice caps (Cuffey and Paterson, 2010).

Mass balance fluctuations in the NCAA

Evidence from ice cores and proxy records indicates that the CAA has been warming since the late 19th or early 20th century, which roughly marks the end of the of the Little Ice Age in the region (Koerner, 1977; Dowdeswell, 1995; Koerner, 2005; Wolken et al., 2008). From the analysis of trimlines corresponding to the maximum extent of land ice cover, Wolken et al. (2008) determined that, by 1960, the total area of glaciers and ice caps in the NCAA had decreased by 37%, and the regional distribution of ice cover shifted from an average elevation of $\sim$700 m a.s.l. during the Little Ice Age, to $\sim$1100 m a.s.l. in 1960. The associated rise in ELA varied between 300–600 m over Devon Island, eastern Axel Heiberg Island, and across most of Ellesmere Island. Meanwhile, the smallest change in ELA ($<$100 m) occurred on southeastern Ellesmere Island along Baffin Bay, along the northern coasts of Ellesmere and Axel Heiberg islands adjacent to the Arctic Ocean, and across the western CAA to Melville Island. In absolute terms, the highest area losses occurred on Ellesmere, Devon, and Axel Heiberg islands where most of the ice cover is concentrated in large ice caps reaching elevations $>$2000 m a.s.l., but relative losses were highest on the low-lying ($<$400 m a.s.l.) plateaus on the western islands, with some becoming entirely ice free by 1960 (Wolken et al., 2008). This pattern underlines the sensitivity of small ice masses at lower elevations, covering relatively narrow elevation

ranges, where even a modest rise in ELA can shift the entire glacier into the ablation zone. The same overall trend is evident in recent years, with particularly rapid shrinkage of small isolated ice caps at lower altitudes (Thomson et al., 2011; Sharp et al., 2014; Serreze et al., 2017; White and Copland, 2018; Curley et al., 2021). Repeat airborne laser altimetry surveys between 1995–2015 over some of the major ice caps in the NCAA indicate that thinning rates tend to decrease with altitude, with some high elevation accumulation regions either showing no change or a slight thickening (Abdalati et al., 2004; Mortimer et al., 2018). Spatial patterns of surface elevation change are more variable along large outlet glaciers where dynamic thinning/thickening related to extensive/compressive flow regimes play a larger role in modifying surface topography (Mortimer et al., 2018).

The rapid increase in glacier ice loss in the NCAA since 2005 is strongly related to an increase in summer temperatures and a lengthening of the melt season (Gardner et al., 2011; Sharp et al., 2011; Mortimer et al., 2016), associated with a pattern of strong atmospheric heat (Sharp et al., 2011; Noël et al., 2018). Over the 2000–15 period, mean summer glacier surface temperatures increased by nearly 1ºC, with glaciers at high altitudes ($>$1400 m a.s.l.) experiencing warming at a rate more than double that recorded at lower elevations ($<$1000 m a.s.l.). In recent years melt has been occurring at all elevations throughout the CAA (Mortimer et al., 2016). With continued warming and mass loss occurring at increasingly higher elevations (Sharp et al., 2014; Mortimer et al., 2016; Thomson et al., 2017), more glaciers are likely to become more sensitive to climate change as rising ELAs reach elevation bands currently in the accumulation zone of large icefields and ice caps, with important implications not only for mass balance, but also for ice dynamics.

Evolving glacier dynamics

As long-term rates of ice motion are dictated by the mass balance gradient, glaciers in the NCAA generally have low balance velocities, corresponding to the mass flux required for glaciers to maintain a steady-state profile. Overall, measured flow rates range from $<$20 m a^{-1} in the interior of ice caps to 50–100 m a^{-1} along main glacier trunks, and reach $>$300 m a^{-1} at the front of large marine-terminating outlets (Burgess and Sharp, 2008; Van Wychen et al., 2014, 2016, 2021; Millan et al., 2017). As a result of increasingly negative mass balance regimes and the associated increase in surface melt and ice surface lowering, many land-terminating glaciers have been slowing down over the last few decades (Heid and Kääb, 2012b; Schaffer et al., 2017; Thomson and Copland, 2017). For example, surface velocities in the lower reaches of White Glacier, western Axel Heiberg Island, decreased by $>$30% since the 1960s in response to high rates of ablation and glacier thinning (Thomson and Copland, 2017). Meanwhile, decreased mass flux allowed the terminus to retreat to higher elevations with lower rates of ablation, which had a stabilising effect, and under current climatic conditions White Glacier is expected to become stagnant in the terminus region within decades. The same general pattern of terminus retreat associated with negative surface mass balance conditions has also been observed over most marine-terminating glaciers in the region (Cook et al., 2019; White and Copland, 2019; Kochtitzky and Copland, 2022). For example, Cook et al. (2019) found that, between 1959–2015, overall greater retreat occurred on outlet glaciers with larger ablation areas and higher mean rates of ablation and runoff. In addition, decadally averaged retreat rates varied with temporal trends of ablation/runoff, suggesting that negative surface mass balance, glacier thinning, and decreased mass flux to the ice front also control changes in terminus position at marine margins.

Dynamic instabilities

In some cases, where flow rates deviate significantly from balance velocities over a sufficiently long period of time, glaciers fail to maintain a steady-state profile and exhibit marked variations in ice motion accompanied by important changes in glacier geometry. Where ice motion exceeds the balance velocity, dynamic thinning lowers ice surface elevation, reducing driving stress and causing flow rates to drop. Conversely, where velocities are insufficient to balance ice flux, mass buildup and/or surface steepening increase driving stress which eventually leads to fast flow conditions. The cyclic fluctuations of surging glaciers represent an extreme example of this kind of dynamic instability, where flow regimes oscillate between long (decades to centuries) quiescent periods of slow flow, and short-lived (months to years) surge periods where velocities can increase by one or two orders of magnitude, up to several kilometres per year (Meier and Post, 1969; Cuffey and Paterson, 2010). As a glacier speeds up in the surge phase, the rapid transfer of mass downglacier often results in significant terminus advance. The drawdown of mass to lower elevations and dynamic thinning decrease driving stress and allow the glacier to slow down, thus leading to surge termination. With the terminus in its most extended position, ice motion stagnates, and surface downwasting is eventually followed by terminus retreat (Meier and Post, 1969; Cuffey and Paterson, 2010). Although ice flow instabilities may not be a direct response to climate, external climatic factors may trigger an unstable dynamic response involving rapid changes in ice flux and glacier geometry.

There are several documented or suspected cases of surging behaviour in the NCAA, but only a few glaciers have been observed in both the active and quiescent phase of the surge cycle, including Otto Glacier, Northern Ellesmere Island (Hattersley-Smith, 1969b) and Iceberg Glacier, Axel Heiberg Island (Copland et al., 2003). Previous work has identified at least 51 surge-type glaciers in the region (Copland et al., 2003; Sevestre and Benn, 2015), but more recent studies suggest that not all of the observed variability fits the classic pattern of surging (Van Wychen et al., 2016, 2021). Studies on glacier surging describe a wide range of behaviours with surge duration, initiation, propagation, and termination varying between glaciers and between regions (Raymond, 1987). There are additionally cases of partial surges, or pulse-like events, with limited propagation of the surge front, where increased flow rates affect only limited regions of the glacier, resulting in more moderate changes than those usually associated with surging (Raymond, 1987; Short and Gray, 2005; Van Wychen et al., 2016, 2021). For example, Van Wychen et al. (2016, 2021) identified several marine-terminating glaciers in the CAA as pulse-type, in that unstable flow conditions develop and remain restricted to their lowermost reaches where the bed is grounded below sea level.

The response of marine-terminating glaciers to external forcing can be more variable than land-terminating glaciers, as their dynamics are controlled by a series of additional factors resulting from interactions at the ice/ocean interface and the added influence of iceberg calving processes. There, a negative mass balance regime can thin the terminus below floatation and trigger an initial increase in flow rates, followed by dynamic thinning, further acceleration, and rapid terminus retreat (Meier and Post, 1987; Pfeffer, 2007; Cuffey and Paterson, 2010). The most notable examples in the NCAA include Trinity and Wykeham glaciers flowing from the eastern Prince of Wales Icefield, southeastern Ellesmere Island, both of which have accelerated significantly and retreated several kilometres over the last two decades (Van Wychen et al., 2016, 2021; Harcourt et al., 2020; Dalton et al., 2022). Surface velocity at the terminus of Trinity Glacier more than doubled since 2000, recently reaching >1 km a^{-1}. Meanwhile, fast flow and dynamic thinning have propagated >30 km upglacier from the terminus, about the distance over which

both glaciers are grounded below sea level. This behaviour is characteristic of marine-terminating glaciers in which a positive feedback between thinning and increased ice surface velocities can lead to unstable terminus retreat and increased dynamic discharge. The dynamic response is largely controlled by subglacial topography and retreat typically continues until the terminus stabilises on a pinning point (Pfeffer, 2007; Cuffey and Paterson, 2010).

1.2 STUDY MOTIVATIONS

The wide spectrum of stable and unstable glacier behaviours documented across the NCAA underlines the non-linear response of individual glacier systems to a common climatic forcing. The role of glacier-specific factors, combined with various feedback processes between mass balance and glacier dynamics, pose a challenge for any attempts to isolate changes due to climatic perturbations from those linked to topographic and geometric factors, and/or unstable glacier dynamics. Any behaviour deviating from the overall regional trend in ice motion has traditionally been attributed to dynamic instabilities such as surging or pulsing, but given the natural variability in the sensitivity and response times of individual glacier systems, the asynchronous behaviour of different ice masses may be related to the time required for individual glaciers to adjust to continuously evolving climatic conditions. Current records of glacier change in the CAA are mainly limited to a few decades, a relatively short time span given that the response time of large glaciers and ice caps can be on centennial timescales, and that the end of the Little Ice Age occurred just over a century ago. In many cases, there are insufficient observations to determine whether variations in ice flow observed on potentially surging glaciers are indeed cyclical in nature, or part of a gradual response to past climatic conditions. In-depth studies on the response of individual glaciers on decadal and longer timescales are required to determine how the observed changes fit in the context of long-term climate fluctuations, and what the likely response might be going forward.

Ice extent and glacier length fluctuations are clear indicators of trends in climatic conditions, but the climate signal reflected in changes in terminus position is delayed, typically averaged over decadal timescales, and influenced by glacier geometry and continuously evolving glacier dynamics. Assessments of long-term glacier change therefore also require observations of ice surface elevation for determining volume and geodetic mass balance. Changes in glacier surface mass balance represent an immediate response to a shift in climate and so make detection of climatic trends more straightforward (Cuffey and Paterson, 2010), but in the NCAA, in situ measurements are mainly limited to four ice masses with (nearly) continuous direct observations since the 1960s: White Glacier, and Melville South, Meighen, and Devon ice caps (WGMS, 2021). Geodetic mass balance estimates from differencing of digital elevation models (e.g. Hugonnet et al., 2021) are invaluable in filling the gap between in situ measurements, but most existing reconstructions rely on satellite data which is often too coarse to resolve the topography of small glaciers and is typically limited in temporal coverage to the 21st century. High resolution datasets spanning multiple decades are therefore required to detect long-term trends of glacier change with any confidence.

Aerial photographs acquired during a series of surveys flown in the late 1950s and early 1960s by the Royal Canadian Air Force (RCAF) provide comprehensive coverage of the CAA and are an invaluable resource for monitoring glacier change. The photographs provided the basis for the standard 1:250,000 and 1:50,000 scale National Topographic System (NTS) maps of the region, which were used to generate the first version of the Canadian Digital Elevation Data (CDED) elevation model. However, earlier photogrammetric methods often had large errors, partic-

ularly in the accumulation area of ice caps with few bedrock features to match. On Axel Heiberg Island, for example, the CDED contained elevation errors of up to 90 m (Cogley and Jung-Rothenhäusler, 2004), making it essentially impossible to derive geodetic mass balance. To date, these aerial photos have been used to map changes in terminus position and ice extent (Copland et al., 2003; Burgess and Sharp, 2004; Sharp et al., 2014; White et al., 2015; Cook et al., 2019; Curley et al., 2021), or to infer historical ice extents from trimlines (Wolken et al., 2008; Curley et al., 2021), but ultimately, little use has been made of the potential elevation data that they could provide.

1.3 FOCUS AND OBJECTIVES

The main focus of this thesis, and the three manuscripts within, is to examine the contrasting response of different glaciers in the NCAA, particularly the difference between the continued advance of Good Friday Glacier, a 50 km long marine-terminating outlet of the Steacie Ice Cap on western Axel Heiberg Island (Chapter 2), and the rapid loss of Bowman Glacier, a small mountain glacier <1 km^2, in Tanquary Fiord, Northern Ellesmere Island (Chapter 4). This includes development of a workflow using structure from motion (SfM) photogrammetry combined with multiview stereo (MVS) processing as a tool for generating high resolution topographic data from aerial photographs, including recent imagery acquired using a digital SLR camera (Chapter 3), and historical imagery from the 1950/60s surveys (Chapter 4). This enables the determination of changes in glacier surface elevation, ice volume, and therefore geodetic mass balance, over a longer period than has previously been achieved in the NCAA.

Three main objectives are addressed in the following three manuscripts (chapters), which compose this thesis:

1. The first objective is to reconstruct the evolution of Good Friday Glacier over the last seven decades, in an attempt to determine whether its long-term advance is related to a dynamic instability as previously suggested (i.e., glacier surging; Müller, 1969; Copland et al., 2003), or whether the advance is a stable response to past climatic conditions. This work highlights the need for long-term observations of changes in ice surface elevation to enable analysis of mass redistribution patterns and ice surface thinning/thickening due to the rapid transfer of mass, which can be indicative of unstable flow regimes.
2. The second objective is to present guidelines for hardware selection and strategies for optimising the acquisition and processing of airborne imaging and positioning data in challenging field conditions (e.g., remote locations, extensive survey areas, complex topography, poor satellite performance). Case studies from two small glaciers surveyed in 2018 and 2019, namely Adams Icefield (Expedition Fiord, Axel Heiberg Island) and Bowman Glacier (Tanquary Fiord, Northern Ellesmere Island), are used to demonstrate the full SfM-MVS workflow for generating accurate high resolution topographic reconstructions in suboptimal field conditions.
3. The third objective of this work is to investigate the potential of current SfM-MVS processing techniques for deriving surface elevation information from historical aerial photographs, enabling direct comparison with recent topographic products for change detection. This uses the topographic reconstruction of Bowman Glacier generated from 1959 and 2018 imagery, and demonstrates the potential of direct comparison between two point clouds for calculating volume change and deriving geodetic mass balance over multidecadal timescales.

A discussion providing an overall summary and analysis of primary findings is included in the final concluding chapter.

2

Seven decades of uninterrupted advance of Good Friday Glacier, Axel Heiberg Island, Arctic Canada

ABSTRACT Previous studies reported that Good Friday Glacier had been actively surging in the 1950–60s, 1990s, and again in 2000–15. Based on observations of terminus position change from air photos and satellite imagery, we fill the gaps between previous studies and conclude that the glacier has been advancing continuously since 1959. Ice surface velocities extracted from optical and synthetic aperture radar satellite images show higher flow rates than on most other marine-terminating glaciers in the region. This behaviour contrasts with the regional trend of glacier retreat over this period. Possible explanations involve a delayed response to past positive mass balance conditions, or a dynamic instability. There is, however, insufficient evidence to attribute this behaviour to classical glacier surging as suggested in previous studies. Based on present day ice velocity and glacier geometry patterns in the terminus region, we reconstruct the evolution of ice motion throughout the advance, and suggest that what has previously been interpreted as a surge, may instead have been a localised response to small-scale perturbations in bedrock topography.

Reproduced from: Medrzycka D, Copland L, Van Wychen W, Burgess D (2019) Seven decades of uninterrupted advance of Good Friday Glacier, Axel Heiberg Island, Arctic Canada. Journal of Glaciology, 65(251), 440-452.

2.1 INTRODUCTION

Surge-type glaciers experience irregular flow regimes, typically cycling between long (decades to centuries) quiescent periods and short-lived (months to years) active/surge periods where velocities increase by one or two orders of magnitude above quiescent levels (Meier and Post, 1969). The classic pattern of surging involves a rapid transfer of mass downglacier, resulting in dramatic velocity increases over most of the glacier length, and significant changes in glacier geometry such as rapid terminus advance and fluctuations in ice thickness (Raymond, 1987).

Out of 51 surge-type glaciers previously inventoried in the northern Canadian Arctic Archipelago (NCAA: Ellesmere, Axel Heiberg, and Devon islands), the most dramatic terminus advances were documented on western Axel Heiberg Island, with three glaciers advancing between 4–7 km in the 1959–99 period (Copland et al., 2003). One of these, Good Friday Glacier (78°33'N, 91°30'W), is a ∼50 km long marine-terminating outlet of the Steacie Ice Cap on southern Axel Heiberg Island (Fig. 2.1). Good Friday Glacier (sometimes referred to as Good Friday Bay Glacier; henceforth GF) was first reported as actively surging in the 1950/60s (Müller, 1969), and again in the 1990s (Copland et al., 2003). Recent observations indicate that the glacier was still advancing in the 2000–15 period, with surface velocities reaching 350 m a^{-1} at the terminus (Van Wychen et al., 2014, 2016; Millan et al., 2017).

Overall there is a high spatial and temporal variability in glacier dynamics in the CAA, with most land-terminating glaciers gradually retreating and slowing over the past few decades in response to a sustained negative mass balance regime (Heid and Kääb, 2012b; Thomson and Copland, 2017; Schaffer et al., 2017; Strozzi et al., 2017). A few of the large marine-terminating glaciers have been shown to exhibit large interannual velocity variations, sometimes varying by >50 m a^{-1} between years, accompanied by changes in their terminus position and ice thickness (Van Wychen et al., 2014, 2016). While marked variations in flow rates have traditionally been attributed to surging behaviour, more recent studies suggest that not all flow variability observed in the CAA fits the classic definition of surging. Some instabilities in ice motion rather resemble short-lived pulse events, often restricted to the lower ablation area of glaciers, which may be related to tidewater glacier dynamics or basal topography (Van Wychen et al., 2014, 2016).

While previous studies indicate that the terminus of GF advanced by ∼7.7 km between 1952 and 1999 (Müller, 1969; Copland et al., 2003), the length and characteristics of the total advance remain poorly constrained due to limited observations between studies and lack of detailed knowledge of ice velocities. In this study we reconstruct the evolution of GF from previous reports and a >50 year record of remotely sensed data. Combining observations of ice surface velocities, changes in terminus position, and ice surface and basal topography, we assess whether the glacier has undergone a continuous advance over the past seven decades and whether the observed changes can be explained by surging or another mechanism.

2.2 STUDY SITE

Axel Heiberg Island, in the NCAA (Fig. 2.1), contains >1100 glaciers covering a total area of ∼11,700 km^2 and supports two major ice caps—the Müller and Steacie ice caps (Ommanney, 1969; Thomson et al., 2011). Ice surface velocities in the CAA typically range between <10 m a^{-1} in the interior of ice caps, increase to 30–90 m a^{-1} along the main trunks of tidewater glaciers, and peak at 200–400 m a^{-1} at their termini. Typical values for land-terminating glaciers in the CAA range between 20 and 50 m a^{-1} (Van Wychen et al., 2014).

Müller (1969) reported that, in the late 1940s and early 1950s, GF was land-terminating, and advancing behind a >1 km wide push moraine, at a steady rate of 20 m a^{-1}, similar to other large glaciers in the region (e.g. Thompson Glacier). During the 1952–59 period, the rate of terminus advance rose to nearly 100 m a^{-1}, and the lowermost 2 km of the glacier thickened and became crevassed. In the mid-1960s, the terminus advance reached a maximum of 200 m a^{-1}, and ice motion increased to >250 m a^{-1} (Müller, 1969). This was accompanied by a large increase in

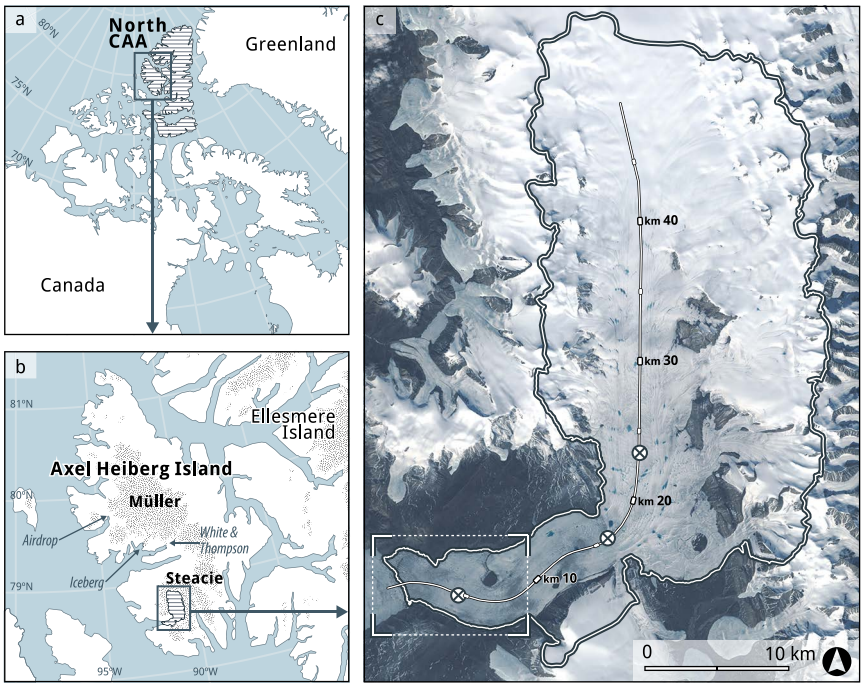

Figure 2.1. **[a]** Ice covered islands of the Northern Canadian Arctic Archipelago; **[b]** Good Friday Glacier (horizontal hatch), Axel Heiberg Island; **[c]** Good Friday Glacier. Base Image: Landsat 8, RGB composite, 07 July 2016. The black and white outline in [c] indicates the drainage basin, and the line corresponds to the glacier centreline. The dashed box marks the terminus region and the extent of Figs 2.2–2.4. The 3 round markers on the ice surface indicate the locations of 3 GPS stations installed in 2015.

the number of crevasses and a chaotically broken-up surface. About 4–6 km upglacier a rim of ice along the valley walls, 10–15 m above the glacier surface, suggested surface lowering. By the late 1960s the rate of terminus advance had decreased significantly (to $\sim$100 m a^{-1}). In the 17 years between 1952 and 1969, the terminus advanced $\sim$2 km, "overriding" most of the push moraine (Müller, 1969).

By 1999 the ice front of GF had advanced an additional $\sim$5.6 km (Copland et al., 2003). Copland et al. (2003) used this evidence, together with a heavily crevassed terminus and looped surface moraines, to classify the glacier as "confirmed surging" with an active phase of at least 10 years and perhaps >40 years. By 2015 GF had advanced an additional $\sim$2 km and continued to exhibit relatively high flow rates (>100 m a^{-1}) over the entire length of the main trunk (Van Wychen et al., 2016).

2.3 METHODS

2.3.1 Ice extent

Near-annual changes in terminus position were mapped for 1972–2018 from optical satellite imagery, namely Landsat 1–8 and ASTER Level 1 products (Table 2.1), accessed through the United States Geological Survey EarthExplorer data portal (https://earthexplorer.usgs.gov). These data products are geometrically/radiometrically corrected and accurately orthorectified, and therefore required no pre-processing. The terminus region was manually outlined in QGIS2.18 (QGIS Development Team, 2017) based on a total of 43 cloud-free images, preferentially acquired at the end of summer for minimal snow cover. No cloud-free images were available for 1994–97, resulting in a four-year data gap. Outlining was performed at single pixel precision on false colour composites, while maintaining a constant scale to minimise errors due to changes in appearance between various spatial resolutions (15 m for ASTER; 30 m for Landsat TM, ETM+, and OLI; 60 m for Landsat MSS). Errors for manual delineation are gener-

ally within one pixel, and accuracy tends to increase with image resolution and glacier size (Paul et al., 2013). Errors in ice extent were assessed by repeated delineation performed on two Landsat scenes, at different resolutions (60 m in 1972; 30 m in 2018). Each terminus was outlined five times, and the relative area difference varied between 1.14% and 0.36% for the 60 m and 30 m resolution images respectively. The 1959 terminus position was mapped from a 1:60,000 scale aerial photograph obtained from the National Air Photo Library, Ottawa, Canada, based on an original survey flown by the Royal Canadian Air Force (RCAF) at an altitude of ∼9000 m (Table 2.1). The air photo was manually coregistered to a base image (Landsat 8, 18 August 2017) using tiepoints. To better account for an irregular terminus geometry, and fluctuations in centreline position over the last six decades, area change in the terminus region was calculated from a fixed reference line (Fig. 2.2b) about 10 km upglacier from the present-day ice front.

Table 2.1. Imagery used for mapping terminus position. Sensor designations: Multispectral Scanner (MSS), Thematic Mapper (TM), Enhanced Thematic Mapper + (ETM+), Advanced Spaceborne Thermal Emission and Reflection Radiometer (ASTER), Operational Land Imager (OLI)

Date of acquisition	Mission, Sensor	Path-row	Date of acquisition	Mission, Sensor	Path-row
1959.07.28	RCAF air photo	A16754_083	1993.06.22	Landsat5 TM	50-4
1972.08.27	Landsat1 MSS	61-3	1998.06.02	Landsat5 TM	50-4
1973.05.26	Landsat1 MSS	63-2	1999.07.31	Landsat7 ETM+	52-3
1974.07.28	Landsat1 MSS	59-3	2000.06.19	Landsat7 ETM+	48-4
1975.08.06	Landsat1 MSS	55-4	2001.06.23	Landsat7 ETM+	55-3
1976.07.28	Landsat2 MSS	61-3	2002.06.12	Landsat7 ETM+	53-3
1977.08.29	Landsat2 MSS	62-2	2003.06.27	Terra ASTER	52-3
1978.07.14	Landsat2 MSS	57-3	2004.06.03	Landsat7 ETM+	51-4
1979.08.02	Landsat2 MSS	63-2	2005.07.31	Landsat7 ETM+	52-3
1980.07.06	Landsat2 MSS	60-4	2006.07.27	Landsat7 ETM+	51-4
1981.07.17	Landsat2 MSS	58-3	2007.08.18	Landsat5 TM	48-4
1982.07.04	Landsat3 MSS	59-3	2008.07.07	Landsat7 ETM+	52-3
1983.04.25	Landsat4 MSS	49-4	2009.08.24	Landsat5 TM	55-3
1984.09.23	Landsat4 MSS	52-4	2010.08.23	Landsat7 ETM+	51-4
1985.05.29	Landsat5 TM	52-4	2011.06.30	Landsat7 ETM+	52-3
1986.05.16	Landsat5 TM	52-4	2012.07.02	Landsat7 ETM+	52-3
1987.07.17	Landsat5 TM	49-4	2013.08.23	Landsat8 OLI	51-4
1988.08.09	Landsat5 TM	52-4	2014.08.31	Landsat8 OLI	54-3
1989.06.02	Landsat5 TM	51-4	2015.08.29	Landsat8 OLI	51-4
1990.09.09	Landsat5 MSS	51-4	2016.08.08	Landsat8 OLI	50-4
1991.07.08	Landsat5 TM	53-3	2017.08.18	Landsat8 OLI	51-4
1992.05.18	Landsat5 TM	50-4	2018.08.03	Landsat8 OLI	53-3

2.3.2 Ice velocities

Speckle tracking

Glacier surface velocities for 2006–18 were determined from speckle tracking on pairs of RADARSAT-1/2 images acquired on repeat 24 day orbits (Table 2.2). RADARSAT-1 imagery was obtained from the Geological Survey of Canada, and RADARSAT-2 through Natural Resources Canada and the Canadian Space Agency. Speckle tracking utilises a cross-correlation algorithm on coregistered pairs of synthetic aperture radar (SAR) images to determine surface ice displacement. We utilise a specially developed MATLAB offset and speckle tracking algorithm that has been extensively utilised for measuring glacier velocities in the CAA (e.g. Short and Gray, 2005; Van Wychen et al., 2014, 2016), and has been shown to provide comparable results to those determined by commercial software packages (e.g. GAMMA InSAR) (Schellenberger et al., 2016). Image pairs were initially coregistered either manually

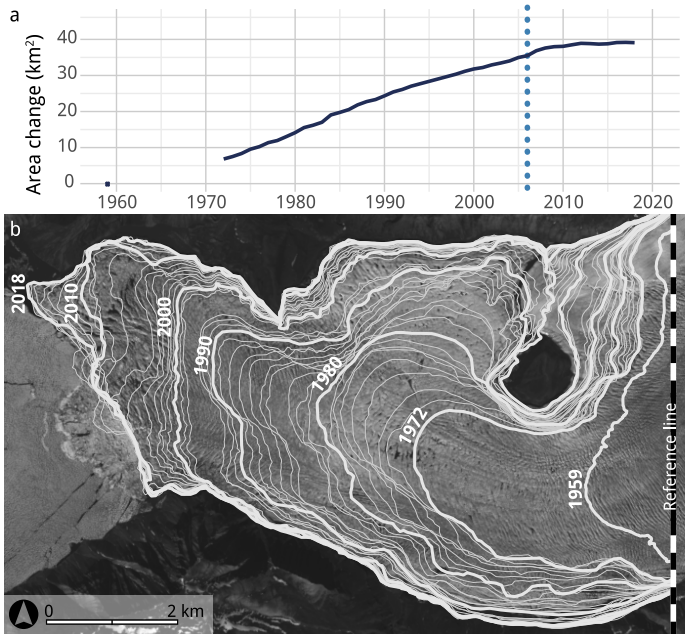

Figure 2.2. **[a]** Area change across the terminus region for 1959–2018. The vertical dotted line indicates the time when the terminus reached tidewater in 2006 and began calving. **[b]** Evolution of the terminus region over the study period, with terminus positions mapped at yearly (thin white lines), and decadal (thick white lines) intervals. Area change for all years was calculated from the dashed reference line at the right edge of the map. Base image: Landsat 8, 29 July 2017.

(RADARSAT-1) or by calculating offsets from orbital parameters (RADARSAT-2). Displacements resulting from speckle tracking were then calibrated over stationary bedrock features to remove any systematic errors. Manual inspection was undertaken to filter out erroneous displacements from mismatching errors during the cross-correlation process. Final ice surface velocities were then interpolated from the filtered point displacements to a 100 m resolution raster dataset using an inverse distance weighting algorithm. Full details of the speckle tracking method are provided in Van Wychen et al. (2014, 2016). The method is most reliable when the ice surface remains relatively unchanged (i.e. little or no melt/snowfall) between images which, for the NCAA, restricts image acquisitions to mid-to-late winter (typically January to April). The velocities derived from speckle tracking therefore reflect 'winter' velocities, and should be regarded as annual minima as they omit any seasonal speedup events associated with enhanced summer melt.

Date of acquisition		Mission,	Band/	Resolution
Image 1	Image 2	Sensor	Beam mode	(m)
1987.08.16	1988.08.09	Landsat5 TM	3	30
1991.08.09	1992.05.18	Landsat5 TM	3	30
1999.07.10	2000.06.19	Landsat7 ETM+	8	15
2006.03.06	2006.03.30	Radarsat-1	Fine	9
2007.03.02	2007.03.26	Radarsat-1	Fine	9
2009.02.17	2009.03.13	Radarsat-2	Fine	9
2010.07.06	2011.07.09	Landsat7 ETM+	8	15
2012.02.27	2012.03.22	Radarsat-2	Wide fine	9
2013.01.04	2013.01.28	Radarsat-2	Wide fine	9
2014.01.23	2014.02.18	Radarsat-2	Wide fine	9
2015.01.18	2015.02.11	Radarsat-2	Wide fine	9
2016.02.06	2016.03.01	Radarsat-2	Wide fine	9
2017.03.20	2017.04.13	Radarsat-2	Wide fine	9
2018.01.02	2018.01.26	Radarsat-2	Wide fine	9

Table 2.2. Image pairs used for deriving ice surface velocities using offset tracking.
Sensor designations: Thematic Mapper (TM), Enhanced Thematic Mapper Plus (ETM+)

Feature tracking

Additional velocities were derived from feature tracking on pairs of annually-separated Landsat images (1987/88, 1991/92, 1999/2000, 2010/11) (Table 2.2). As the method requires distinct surface features, summer images acquired in June-August were selected to ensure minimal snow cover. To enhance contrast between features and improve edge detection, a two-step filtering method was applied using the 'raster' package (Hijmans, 2017) in R 3.4.3 (R Core Team, 2017). We used a 3×3 pixel kernel, corresponding to ∼100 m on the 30 m resolution TM images, and ∼50 m on the 15 m resolution ETM+ scenes. Images were first smoothed (lowpass filtered) to reduce high frequency noise, and then sharpened (highpass filtered) to attenuate low frequencies and enhance intensity contrasts between edges of small scale surface features, mainly crevasses and melt channels, as well as large scale longitudinal foliations. Displacements between images due to ice flow were tracked using a normalised cross-correlation algorithm implemented in the image correlation software CIAS (Kääb and Vollmer, 2000; Heid and Kääb, 2012a). The resulting displacement vectors were filtered, in both direction and magnitude, by applying a median filter on a ∼500 m radius moving window using the 'raster' package (Hijmans, 2017). Incorrect matches deviating by more than 45º in direction, and ±25% in magnitude, from the median of the neighbouring vectors were removed from the dataset. Final velocities were interpolated to a 100 m resolution raster using an inverse distance weighting algorithm and the 'gstat' package (Gräler et al., 2016) in R.

Error analysis

The accuracy of both offset tracking methods was assessed from apparent displacements measured over stable terrain adjacent to the glacier. The average errors and standard deviation for feature tracking results were 19 ± 40 m a^{-1}, or 9 ± 6 m a^{-1} after filtering erroneous matches. These values compare well with error margins of ∼5–15 m a^{-1} determined here and in previous studies using the speckle tracking method in the CAA (e.g. Short and Gray, 2005; Van Wychen et al., 2014, 2016). Velocity results derived from speckle and feature tracking methods were also compared with field measurements from three dual frequency GPS (dGPS) stations mounted on poles drilled into the glacier surface ∼5, 15, and 25 km from the terminus (Fig. 2.1c). The stations recorded positions at 15 second intervals for an hour at midday each day, providing mean daily positions between July 2015 and July 2017. The difference in annual displacements derived from speckle tracking and dGPS observations from two overlapping 24-day periods in the winters of 2016 and 2017 is 3–5% (3–5 m a^{-1}). These 'winter' velocities are 6–10% lower than annual velocities derived from the mean daily dGPS observations, which include periods of high velocity fluctuations over spring/summer months. In comparison, feature tracking results from two pairs of annually-separated Landsat OLI images (2015/16, 2016/17) are within 0–12% (0–16 m a^{-1}, ∼9 m a^{-1} on average) of dGPS measurements collected over the same period.

2.3.3 Ice surface and bed elevation

Ice surface topography was extracted from the ArcticDEM (Porter et al., 2018), produced by the Polar Geospatial Centre from DigitalGlobe (Worldview-1/2/3 satellites) imagery. The DEM was generated from overlapping stereo pairs of optical images at ∼0.5 m resolution acquired between 2012 and 2015, and processed into 5 m resolution mosaics in 50×50 km tiles (https://www.pgc.umn.edu/data/arcticdem/). The reported horizontal and vertical accu-

racy of the final product is within 0.2 m of the ice surface at the time of image acquisition (Noh and Howat, 2015), and the mean vertical residual after correction with clusters of IceSAT altimetry data was −0.002 m and 0.015 m for tile 32_31, and 0.003 m for tile 32_32.

We use bed elevation data from airborne radar measurements from the Centre for Remote Sensing of Ice Sheets (CReSIS) Multichannel Coherent Data Depth Sounder (MCoRDS) operating at a frequency range of 180–210 MHz (Allen, 2013). The radar was flown at an altitude of 500–900 m above the ice surface along the full length of GF in March 2014 as part of NASA's Operation IceBridge. The data were gridded using radar tomography processing into a ∼3 km wide swath, with an along-track sample spacing of 16 m, and a cross-track spacing of ∼30 m at nadir and ∼100 m at the edge of the swath. The final product is a 25 m resolution map of basal topography (CReSIS, 2016). Tomography requires good signal to noise ratio to accurately differentiate between off-nadir echoes. Vertical accuracy therefore varies with surface roughness, and englacial/basal water content. Studies have found the uncertainty in ice thickness to be within 10–20 m (Paden et al., 2010; Wu et al., 2011; Jezek et al., 2013). Both bed and surface elevation profiles were extracted along the centreline of the glacier, with the exception of a ∼3 km long segment roughly 6 km from the terminus where the IceBridge flightline deviated from the centreline and passed over a large nunatak (Fig. 2.3). Over this region, the bed topography was extracted from the edge of the swath, with the furthest extrapolated point being ∼170 m north of the centreline.

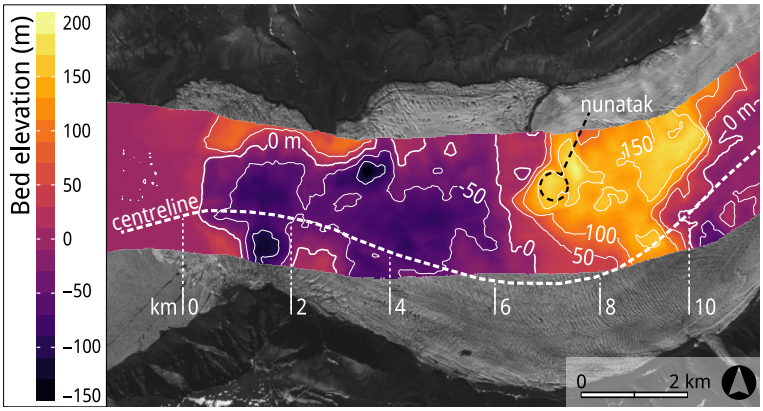

Figure 2.3. Bed elevation map from IceBridge MCoRDS tomography data. The flightline deviates from the glacier centreline 5–8 km from the terminus. Contours at 50 m intervals.

2.4 RESULTS

2.4.1 Terminus position

Results show a terminus advance of 8.6 km along the centreline of GF over the 1959–2018 period (Fig. 2.2), amounting to ∼9.3 km since the first observations in 1948. The area of the terminus region increased at a steady rate of ∼1 km^2 a^{-1} throughout the 1970–80s, slowed by 25% (to 0.73 km^2 a^{-1}) in the 1990s, and dropped by an additional 82% (to 0.18 km^2 a^{-1}) since 2006–08. The terminus increased in area by ∼39 km^2 over the last 59 years (Fig. 2.2), representing a ∼5% increase in glacier area compared to a total basin size of 800 km^2.

The 1959 air photo shows the ice front just south of the nunatak (Fig. 2.4a), ∼7 km from the current terminus position. This nunatak is the surface expression of a >150 m high ridge extending approximately north to south across the glacier channel (Fig. 2.3). In 1959, two small looped moraines were visible along the southern margin,

one immediately at the terminus (Fig. 2.4a), the other ∼4 km upglacier. Where the ice is channelled into the narrow trough south of the nunatak, the lowermost 2 km of the terminus was broken up by a field of transverse crevasses extending across the front in an arcuate pattern (concave downglacier). In comparison, the surface of the northern half of the terminus was relatively smooth with some splaying crevasses in the along-flow direction. The more advanced southern half was separated from fjord waters by a partially submerged 800 m wide push moraine. Müller (1969) reported that by 1969 the terminus had overridden most of this moraine. At the time of the first Landsat image in 1972, GF had become marine-terminating and continued to be so throughout the remainder of the 1970s (Figs 2.4b and 2.5a). However, at the beginning of the 1980s a new moraine had started to emerge at the terminus and by 2000, the ice front was once again separated from fjord waters by a ∼600 m wide moraine (Fig. 2.4c).

The terminus continued to advance behind the moraine until 2006–08. Throughout this period the surface at the glacier front remained relatively smooth with some splaying crevasses forming along the terminus. As the ice overrode the moraine between 2006–08 (Fig. 2.4d), the terminus became broken up by a field of transverse crevasses extending ∼1 km upglacier (Fig. 2.4e). From that point on, fluctuations in terminus position became highly seasonal—each winter the ice front pushes forward, splaying out into the sea ice in a large digitate lobe (Fig. 2.5b), and disintegrates within a few days as the sea ice clears the fjord the following summer. The southern portion of the terminus has become essentially stationary at approximately the position where the terminal moraine was last seen in 2006. Meanwhile, over the last decade, the northern sector has advanced by ∼1.5 km, although the rate of advance has declined considerably in the last three years (Fig. 2.2).

2.4.2 Velocity patterns

Results show a general decrease in surface velocities over the full length of the glacier since the late 1980s (Fig. 2.6b). The glacier bed first drops below sea level around km 20 (Fig. 2.6a), approximately where it changes flow direction (from southerly to south-westerly), however, this is not continuous over the full width of the channel and most of the ice remains grounded above sea level. Ice motion shows higher spatial variability downglacier from this point, with a major velocity peak immediately downglacier of the 150 m high (>50% of ice thickness) ridge extending across the glacier channel at km 9 (Fig. 2.3). The ArcticDEM surface profile (Fig. 2.6a) shows a thickening upglacier from this topographic high, and a marked steepening and 70 m elevation drop immediately downglacier from it. Flow rates at this location dropped from 470 m a^{-1} in the late 1980s, to 170 m a^{-1} in 2018, but have consistently remained 30–50% higher than on either side of the bump (Fig. 2.6). Downstream of the ridge, the ice is grounded in an overdeepening which drops to 50–70 m below sea level. The bed slope is reversed over the lowermost 1.5 km (Figs 2.3 and 2.6a).

In the 1980–90s velocities decreased towards the ice front, as is typical for land-terminating glaciers (Van Wychen et al., 2016), but starting in 2006 the pattern changed and flow rates now rapidly increased over the lowermost ∼4 km. Velocity profiles for 2006–18 show velocities ranging between 100 and 250 m a^{-1} along the main trunk of the glacier, and reaching >350 m a^{-1} at the terminus. These values are comparable to those recorded in the 1960s (∼250 m a^{-1}) in the terminus region (presently km 8) when Müller (1969) suggested that the glacier was actively surging. Despite continued fast flow, and consistently high velocities at the terminus, the glacier has slowed by ∼50–100 m a^{-1} over much of its length over the last decade (Fig. 2.6b).

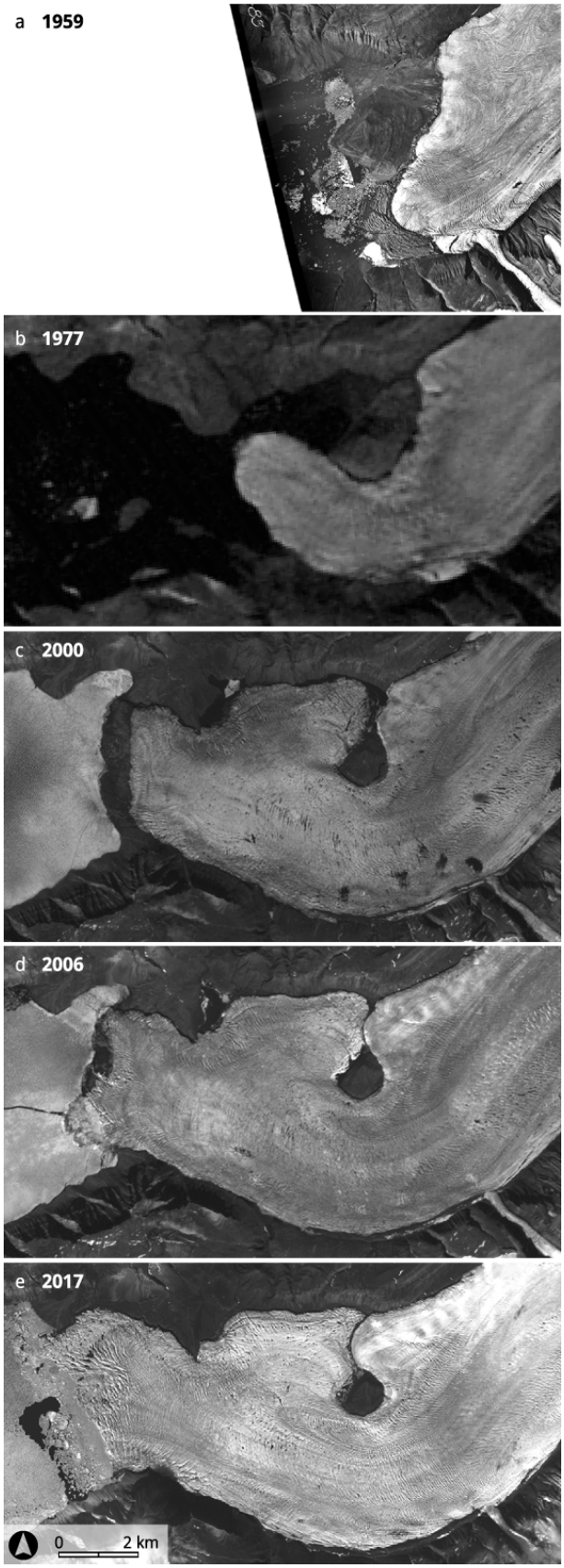

Figure 2.4. Evolution of the terminus over the study period
[a] RCAF air photo, 1959.06.29;
[b] Landsat 2, 1977.08.20;
[c] Landsat 7, 2000.06.20;
[d] Landsat 7, 2006.07.27;
[e] Landsat 8, 2017.08.14.

2.5 DISCUSSION

Good Friday Glacier is located within a region where mass balance has been dominated by a trend of accelerating mass loss (e.g. Gardner et al., 2011, 2013; Sharp et al., 2011; Lenaerts et al., 2013; Noël et al., 2018). The uninterrupted terminus advance since 1948, and the relatively high (>100 m a^{-1}) velocities recorded along the full length of the glacier (Figs 2.6b and 2.7), are therefore unexpected. This raises the question as to what mechanism(s) has been driving this asynchronous behaviour. We evaluate two factors, namely mass balance and dynamic instabilities, as potential causes for the long-term advance. We examine the spatial variability in dynamics in the terminus region in relation to local variations in bedrock topography, and propose an alternate interpretation to surging for the temporal evolution of ice motion at the glacier front throughout the advance.

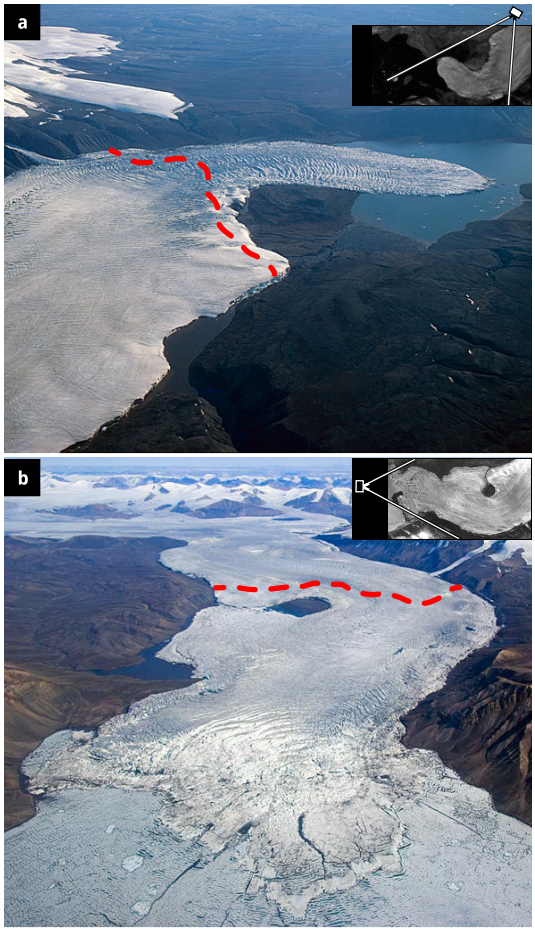

Figure 2.5. Terminus of Good Friday Glacier on **[a]** 24 August 1977 (looking southwest), and **[b]** 01 July 2008 (looking east), with the splayed lobe advancing into the sea ice. The red outlines approximate the 1959 terminus position. The two insets indicate the direction from which the photos were taken, with white lines representing the camera viewshed. Photos: Jürg Alean (www.swisseduc.ch).

2.5.1 Mass balance

Annual mass balance estimates for the NCAA have been mostly negative since the early 1960s (Koerner, 2005), and recent studies indicate accelerated mass loss in the last two decades (Gardner et al., 2011; Lenaerts et al., 2013; Millan et al., 2017; Box et al., 2018; Noël et al., 2018). Using a regional climate model Noël et al. (2018) showed that, for the 1958–95 period, glaciers and ice caps in the NCAA experienced an overall negative mass budget with losses totalling 11.9 $\pm$ 11.5 Gt a^{-1}. Since the mid-1990s, losses more than doubled, reaching 28.2 $\pm$ 11.5 Gt a^{-1}

(Noël et al., 2018). This sharp increase in mass loss has been in direct response to rising summer air temperatures, resulting in higher surface melt rates and longer melt seasons (Gardner et al., 2011; Sharp et al., 2011; Mortimer et al., 2016, 2018; Noël et al., 2018). As a result of this sustained negative mass balance regime, most land-terminating glaciers in the CAA have been retreating and slowing down (Thomson et al., 2011; Heid and Kääb, 2012b; Schaffer et al., 2017; Thomson and Copland, 2017).

An inventory of glacier change on Axel Heiberg Island from 1959 to 2000 showed a dominant trend of glacier retreat, with greatest mass loss on small independent glaciers, including the loss of 90% of ice masses smaller than 0.2 km^2 (Thomson et al., 2011). However, these losses were partially offset by glacier advances in basins dominated by outlets from the Müller and Steacie ice caps. Three of them (GF, Iceberg and Airdrop glaciers) were classified as surge-type (Copland et al., 2003), and their advances were therefore attributed to surge activity. In general, the advancing glaciers were found to be larger on average (Thomson et al., 2011). Modelling studies have shown that large arctic glaciers with shallow surface slopes generally have longer response times than smaller ice masses in the region, and therefore require centuries longer to adjust to changes in surface mass balance following a change in climatic conditions (Raper and Braithwaite, 2009). A comparison of in situ velocity measurements from the 1960–70s and 2012–16 on White Glacier, a ~14 km long mountain glacier located ~65 km N of upper GF, shows a general long-term decrease in flow rates, especially towards the glacier terminus (Thomson and Copland, 2017). While White Glacier retreated ~250 m between 1948 and 1995, the neighbouring Thompson Glacier, a land-terminating outlet of the Müller Ice Cap, advanced by ~950 m over the same period (Cogley and Adams, 2000; Thomson et al., 2011), and only started retreating at some time in the 2000s (Cogley et al., 2011). One possible explanation for this contrasting behaviour may be related to the different geometries of White vs. Thompson glaciers and the difference in their respective response times. Considering the significantly larger size of the Thompson (~390 km^2) compared to White Glacier (40 km^2), the longer advance may therefore reflect a delayed response to a positive mass balance regime driven by past cooler conditions (Cogley and Adams, 2000; Cogley et al., 2011).

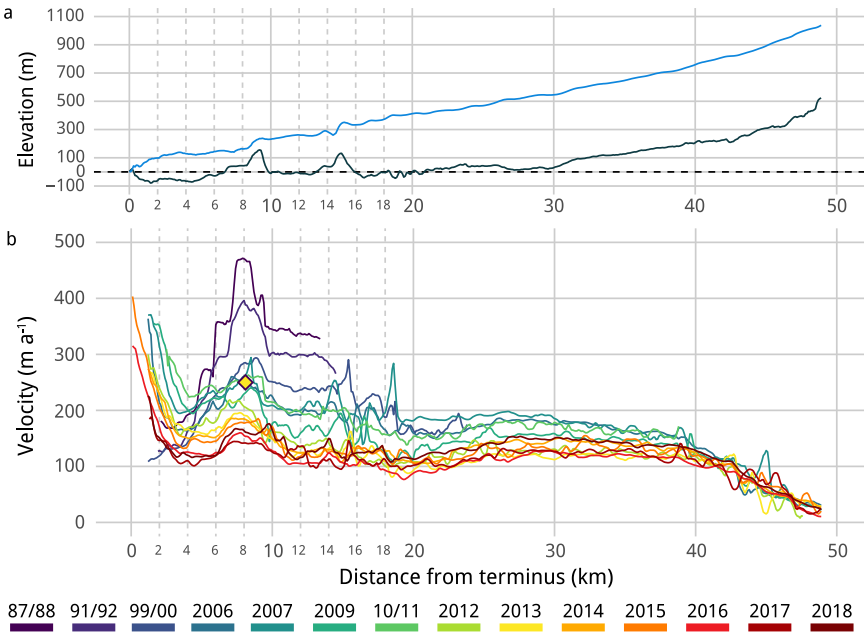

Figure 2.6. **[a]** Ice surface (blue; ArcticDEM) and bed elevation (black; Icebridge MCoRDS) profiles. **[b]** Centreline ice surface velocities for 1987–2018. Profiles spanning two consecutive years (e.g. 87/88) correspond to velocities extracted from feature tracking. Those spanning a single year were derived from speckle tracking. The yellow diamond indicates velocities recorded at the terminus in 1959.

In comparison, GF, the largest of the three glaciers (800 km^2), has been advancing continuously to this day. However, our results show that surface velocities have decreased by 50–100 m a^{-1} over much of the glacier length over the last decade, and ice motion in the terminus region has been slowing since at least the late 1980s (Fig. 2.6). Although the uninterrupted advance over the last seven decades could be related to past positive mass balance conditions, the gradual slowdown supports the idea that GF has been losing mass similarly to other glaciers in the region. Indeed, Noël et al. (2018) showed that the average surface mass balance of GF has been negative over much of its length over the 1958–2015 period. Alternatively, the asynchronous behaviour of GF, and until recently the Thompson, may instead be related to a dynamic instability, such as surging (Copland et al., 2003).

2.5.2 Dynamic instabilities

Glacier surging

Dynamic instabilities typically occur when short-term flow rates deviate (significantly) from long-term balance velocities. In these cases, glaciers fail to maintain a steady-state profile and instead experience changes in geometry while cycling between fast and slow flow regimes. On surge-type glaciers, velocity fluctuations occur in response to changes in driving stress, which typically increases along with thickening and surface steepening during quiescence, eventually initiating the surge (Raymond, 1987). The classic pattern of surging involves a downglacier propagation of a surge front, resulting in dramatic velocity increases over most of the glacier length, rapid terminus advance, and significant surface lowering. The resulting dynamic thinning eventually reduces the driving stress, allowing the glacier to slow down thus leading to surge termination. The quiescent phase typically coincides with terminus retreat (Meier and Post, 1969; Raymond, 1987).

Although glacier surges are not typically thought of as a direct response to climate, external climatic factors dictate changes in mass balance, which in turn influence the length and intensity of surges (Eisen et al., 2001; Copland et al., 2011). Surge-type glaciers in high accumulation regions with temperate thermal regimes (e.g. Alaska, Yukon) typically have a shorter active phase (1–2 years) than those in polar environments with limited snowfall and polythermal regimes such as Svalbard (Dowdeswell et al., 1991; Murray et al., 2003) and the Canadian Arctic (Copland et al., 2003; Short and Gray, 2005). On Svalbard, the surge phase generally lasts 3–10 years, and surge termination is a gradual process which can take several years (Dowdeswell et al., 1991). Previous observations of surging glaciers in the NCAA suggest that the surge phase may last anywhere from 5–10 years, to as much as 50 years (Hattersley-Smith, 1969b; Müller, 1969; Copland et al., 2003; Short and Gray, 2005; Van Wychen et al., 2016).

One issue with long surge cycles is the difficulty in identifying the period of surge initiation and termination, and therefore accurately constraining the duration of the active phase. This is partly due to the limited timespan covered by many datasets, and the generally lower velocities and more gradual changes associated with surging in polar regions. This introduces an observational bias, and few polar glaciers have been observed to surge more than once. Surge-type glaciers can be identified by the presence of surface features indicative of flow instabilities. Looped moraines and ice foliations are diagnostic of oscillatory behaviour and are therefore generally regarded as reliable signs of surging (Meier and Post, 1969; Clarke, 1987; Copland et al., 2003). Previous studies have identified 13 glaciers with signs of unstable flow on Axel Heiberg Island. Most of these were classified as likely or possibly surge-type, mainly based on the presence of said surface features. Of the 13 glaciers, the largest three (GF, Iceberg,

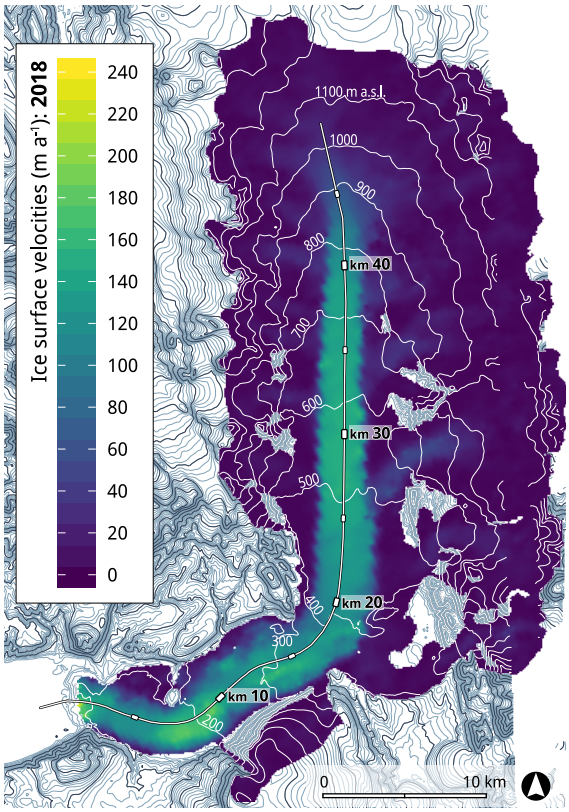

Figure 2.7. Ice surface velocities along Good Friday Glacier, derived from speckle tracking of RADARSAT-2 image pairs from 02 and 26 January 2018. Longitudinal velocity profiles were extracted along the centreline (black and white line). A ∼150 m high ridge runs south-east from the nunatak, roughly following the 200 m contour line at km 9.

Airdrop) experienced fast flow and important terminus advances (4.5–7 km) in the 1959–99 period, and were thus classified as surge-type (Copland et al., 2003). While all three have decelerated since 1999, Iceberg Glacier is the only one to have displayed a cyclic behaviour that is typical for surging glaciers (Van Wychen et al., 2016).

Iceberg Glacier is a large (∼750 km^2) marine-terminating outlet glacier which drains the western side of Müller Ice Cap, located ∼70 km NNW of the upper parts of GF. In 1959, the terminus was retreating (Ommanney, 1969) and the ice surface was heavily potholed over an extensive area, two characteristics of stagnating glaciers in the quiescent phase of the surge cycle. By 1999, the glacier had advanced ∼5 km (Copland et al., 2003). Following studies reported high flow rates over the entire trunk of the glacier (Short and Gray, 2005; Van Wychen et al., 2016), reaching up to ∼575 m a^{-1} at the terminus in the 1990s (Copland et al., 2003). This was followed by a period of terminus retreat coinciding with slowdown, which reportedly began at the terminus in the early 2000s, and had propagated over the entire trunk by ∼2010. Iceberg Glacier has been essentially stagnant since, and the terminus retreated ∼1.5–2.5 km over the 2000–14 period (Van Wychen et al., 2016). This is the only glacier on Axel Heiberg Island to have been observed in the quiescent phase of the surge cycle twice, with the evidence pointing to an active phase lasting between 10–30 years.

Iceberg Glacier and GF are the largest, and only two marine-terminating glaciers on the island. Although they are similar in their general configuration and climatic setting, the cyclic oscillations in ice motion observed on Iceberg Glacier indicate that its dynamics are at least partly decoupled from the long-term climate trend of negative mass balance since 1958 (Noël et al., 2018). This contrasts with the evidence from GF where no retreat has yet been recorded, and there are no observations of the glacier in the quiescent phase of the surge cycle. The initial speedup

in the 1950s may correspond to surge initiation, and the gradual decrease in ice motion and terminus advance of the last decade may in turn indicate that the glacier is now approaching quiescence. If GF is indeed surging, the sustained terminus advance of the last 70 years would correspond to the longest active phase ever recorded, both on a regional and global scale.

A spectrum of flow instabilities

Müller (1969) concluded that while GF exhibited some tell-tale signs of surging, including an increase in surface velocities an order of magnitude above background levels, intense surface crevassing, and a marked terminus advance, he found no clear sign of a surge front propagating downglacier. Additionally, the long active phase ($>$10 years) and the lack of evidence of previous surges distinguished it from other classic examples of surging (Meier and Post, 1969). As evidenced by Iceberg Glacier and other glaciers in the CAA, 10 years may not be particularly long for an active surge phase in polar regions, but 70 years is significantly longer than any surge reported to date.

With longer surge cycles, evidence of past surge activity becomes less evident. The heavily folded longitudinal foliations and the two small looped moraines visible near the terminus of GF on the 1959 air photo (Fig. 2.4a) may indeed be interpreted as signs of unstable flow, but do not in themselves provide evidence of past surges. The moraines may have instead formed as GF advanced into previously unglaciated terrain, entraining the snouts of slower glaciers which, until then, had been flowing unhindered onto the main valley floor below. On the other hand, the absence of characteristic surge features does not mean that a given glacier has not surged in the past. Similarly, the lack of evidence of a clear surge front propagating downglacier does not exclude the possibility that the changes in glacier geometry occurring on GF in the 1950s may correspond to a phase of surge initiation. The thickening at the terminus, the rapid advance, and thinning further upglacier may indicate fast flow conditions initiating at the terminus, and propagating upglacier instead. This behaviour has been observed on several marine-terminating glaciers on Svalbard (e.g. Murray et al., 2003; Sevestre et al., 2018), as well as in the Canadian Arctic (Van Wychen et al., 2016), but is rather unlikely to have occurred on GF at the time since the terminus was then grounded well above sea level, behind a $\sim$1 km wide and 30 m high moraine (Müller, 1969). That being said, it would appear that the ice front reached fjord waters at some time in the mid-1960s, and the terminal moraine became progressively submerged as the terminus advanced past the nunatak and into a wider section of the valley (Fig. 2.4). This approximately coincides with the area where the bed dips below sea level around kms 6–7 (Fig. 2.6a). Tidewater dynamics may have therefore played a role in encouraging fast flow in the mid-1960s, and/or contributed to the brief drop in the rate of terminus advance at the end of that decade.

Although several factors suggest a dynamic instability, there is no unequivocal evidence of surging behaviour in the classic sense of the term. However, it is well established that dynamic instabilities encompass a wide spectrum of behaviours, with the duration, initiation, propagation and termination of fast flow events varying between glaciers and regions. Glaciers can therefore experience significant interannual variations in ice motion without necessarily being classified as surge-type. Studies describe cases of partial surges, or pulse-like events, which broadly encompass all periodic episodes of unstable flow resulting in more moderate changes than those usually associated with surging (Raymond, 1987; Turrin et al., 2014; Van Wychen et al., 2016). Van Wychen et al. (2016) differentiated surging from pulsing by the velocity structure and pattern of initiation and propagation of fast flow conditions

in CAA glaciers. They identified several marine-terminating glaciers as pulse-type, as fast flow initiated at the terminus and remained restricted to their lowermost reaches where the bed is grounded below sea level.

The dynamics of large tidewater glaciers are generally more variable than for land-terminating ones, as ice motion is controlled by a series of additional factors related to the force balance at the ice/ocean interface (e.g. Pfeffer, 2007; Nick et al., 2009; Straneo et al., 2013). Marine-terminating glaciers are known to undergo asymmetric cycles of slow advance followed by rapid retreat and terminus disintegration through calving. The tidewater glacier cycle underlines the importance of glacier-specific factors, such as basal topography, in driving unstable flow behaviour (Meier and Post, 1987; Alley, 1991; Brinkerhoff et al., 2017). The key point is that the distinction between surging and other unstable flow behaviour is not clear cut, and in many cases it is a question of semantics. This underlines the importance of considering the periodic oscillations attributed to surging as part of a wider spectrum of dynamic instabilities (Raymond, 1987; Turrin et al., 2014; Van Wychen et al., 2016), including single episodes of fast flow and short-lived or localised speedup events.

2.5.3 Perturbations in bedrock topography

The idea that GF is (or was) surging mainly depends on how one interprets the changes in ice motion occurring at the glacier terminus in the 1950–60s. It is therefore useful to review the evidence for fast flow, and examine alternate mechanisms as potential triggers. The way in which present day ice velocity and glacier geometry patterns vary can provide insight into the evolution of ice motion at the terminus as it advanced into previously unglaciated terrain. On a local scale, variations in surface geometry and ice motion depend on basal conditions (bedrock topography and basal water pressure), which modulate resistance to flow through along-flow gradients in basal and lateral drag (Cuffey and Paterson, 2010). Ice typically thickens through compression upglacier from bedrock bumps, or where flow converges into narrow valley sections, and thins through extension as it flows over the obstacle, or out of the constriction. Driving stress rises with increasing surface slope, which then leads to faster flow and increased crevassing over the bump or through the constriction (Gudmundsson, 2003; Raymond and Gudmundsson, 2005; Sergienko, 2012). Longitudinal stress gradients further modulate ice flow through differential pushes and pulls, such that where velocities increase along a flowline, the faster flowing ice is held back by slower ice further upglacier, which is in turn entrained by the faster ice downstream. Through the propagation of longitudinal stresses, extensional flow in a region of low basal drag may therefore induce dynamic thinning and a velocity increase further upglacier (Cuffey and Paterson, 2010). On the downstream side of an obstacle or constriction, the ice experiences longitudinal compression as it flows into slower moving ice, and consequently slows down (Sergienko, 2012).

On GF, surface velocities increase in the vicinity of the nunatak, where ice flows over a topographic high extending across the glacier channel at km 9 (Fig. 2.6). Flow rates measured over that area reached $\sim$250 m a^{-1} in the 1960s (Müller, 1969), and have remained consistently high since the late 1980s, ranging between 160–470 m a^{-1} (Fig. 2.6). This localised velocity peak, and the variations in surface elevation, namely thicker ice on the upglacier side of the bump, and steepening and surface drop downglacier from it, are consistent with ice flow anomalies related to irregular bedrock topography (Gudmundsson, 2003; Raymond and Gudmundsson, 2005; Sergienko, 2012).

Müller (1969) observed a series of changes in ice motion in the 1950–60s, including (a) thickening at the ice front, (b) rapid frontal advance, (c) sudden speedup, and (d) increased crevassing. These occurred as the glacier front

advanced over this bedrock bump, and into the narrow trough south of the nunatak. The initial thickening at the terminus may have been related to a combination of longitudinal compression on the upstream side of the 150 m high ridge, and lateral compression where the 5 km wide ice front was channelled into the 2 km wide constriction (Fig. 2.4). Thicker ice would have encouraged fast flow, longitudinal extension, and thinning further upglacier. The sudden increase in the number of crevasses, and the chaotically broken up surface were likely a result of longitudinal and lateral compression followed by longitudinal extension (Hudleston, 2015). Similar intense crevassing has also been observed on surging glaciers following the passage of a surge front (Kamb et al., 1985; Lawson et al., 1994; Murray et al., 1998). Indeed, all these changes (a–d) can be associated with surging. It is therefore conceivable that, as the glacier reached the constriction south of the nunatak in the 1950s, the reported changes in ice motion may have been similar to those occurring during surge initiation. This was followed by a (brief) drop in the rate of terminus advance in the second half of the 1960s, which may have been related to a change in the force balance at the ice front as the glacier reached sea level. While the ice was grounded below sea level, the terminus was separated from fjord waters by the push moraine, which would have prevented calving.

Flow rates tend to increase towards the termini of tidewater glaciers and areas grounded below sea level as effective pressure, and therefore basal drag, both drop where the glacier approaches floatation (Benn et al., 2007). Lateral drag, on the other hand, is inversely proportional to trough width, and higher velocities occur where the fjord widens and flowlines diverge (Benn et al., 2007). Fjord narrowings and topographic highs both act as pinning points which can stabilise the glacier margin, thus controlling the magnitude of advance and retreat (Benn et al., 2007; Gudmundsson et al., 2012; Jamieson et al., 2012; Enderlin et al., 2013; Carr et al., 2015). Rapid advance in the mid-1960s may have occurred in response to increased basal water pressure at the terminus where the bed drops below sea level, accompanied by a drop in lateral drag where the valley widens. The presence of weak and easily deformable marine sediments at the ice/bed interface may have further enhanced basal motion (Clarke, 1987). The slowdown at the end of the decade may at least in part be explained by a reduction in driving stress induced by dynamic thinning in response to extensional flow (Cuffey and Paterson, 2010).

At the beginning of the 1970s the glacier had advanced into a basal overdeepening dipping to 70 m below sea level (Fig. 2.6a), and the rate of terminus advance increased once again. It has been argued that the advance rate of tidewater termini is influenced by sedimentation at the grounding line and the presence of a terminal moraine shoal, which can act as a pinning point, reduce calving rates and stabilise the ice front (Meier and Post, 1987; Alley, 1991; Brinkerhoff et al., 2017). The advance of the terminus into the basal overdeepening may have therefore been facilitated by the formation of a submarine sediment shoal at the grounding line. This shoal was subsequently thrust up above water level (Fig. 2.4c) by the advancing ice front where the bed slopes upward in the direction of flow between kms 2–4.

The velocity profile at the terminus for the 1980–90s was characteristic of land-terminating glaciers, with velocities decreasing towards the glacier front. Velocities for 2006–18 are markedly different, with an acceleration towards the glacier front, reflecting a pattern characteristic of marine-terminating glaciers (Fig. 2.6b). The moment when the front reached tidewater in 2006 also coincides with a change in the crevasse pattern in the terminal zone, from some longitudinal splaying crevasses, to transverse crevassing (Fig. 2.4), suggesting a transition from a compressive to an extending flow regime (Colgan et al., 2016). Longitudinal crevasses likely formed in response to longitudinal

compression and resistance to flow where the ice front advanced over an upward sloping bed. Transverse crevasses are in turn indicative of longitudinal extension and high flow rates in areas of reduced resistance to flow, such as where ice flows into deeper water and/or a widening fjord (Hambrey and Lawson, 2000; Colgan et al., 2016).

Today GF is in a stable extended position, with the terminus grounded on the moraine shoal, at the head of a wider section of the fjord, and any advance is approximately balanced out by calving losses. Since the ice entered the fjord in 2006–08, the southern portion of the glacier front started experiencing a seasonal cycle of advance/retreat linked to the presence/absence of sea ice in the fjord. A number of studies have reported the role of sea ice and ice mélange in limiting calving in the winter (e.g. Amundson et al., 2010; Howat et al., 2010; Walter et al., 2012; Cassotto et al., 2015; Krug et al., 2015). Evidence shows that sea ice can essentially act as a thin ice tongue and provide enough backstress to stabilise the terminus and prevent calved icebergs from drifting away (Amundson et al., 2010). We observe this process in the winter as the terminus of GF advances several hundred meters into the sea ice, forming a wide digitate lobe of calved ice, or ice mélange (Fig. 2.5b). This transient terminus then disintegrates rapidly (within a few days) as the sea ice clears the fjord in the summer (usually late July, early August). Without the stabilising resistive force provided by the sea ice, the southern part of the ice front is forced to retreat to its last stable position, approximately where the moraine was last seen in 2006. The asymmetry between the rate of advance of the southern and northern sections of the glacier front suggests the presence of local variations in basal/lateral drag. Until recently, the continued advance of the northern section of the front may have been facilitated by the geometry of the shoreline. However, the advance has slowed significantly over the last few years as the ice moved past the pinning point where the fjord widens.

2.6 SUMMARY AND CONCLUSIONS

Based on previous reports extending back to 1948, observations of changes in terminus position since 1959, and ice surface velocities since the late 1980s, we have reconstructed the evolution of GF over the past seven decades. Our results show an uninterrupted terminus advance of $\sim$9 km spanning the last 70 years, which is the longest advance ever observed for a Canadian glacier, and contrasts with the dominant regional trend of accelerated mass loss and glacier retreat over the past century. If this advance is interpreted as a surge it would correspond to the longest active phase ever recorded globally. The initial thickening at the ice front, followed by rapid terminus advance, increase in surface crevassing, and surface drawdown, are all features characteristic of a classic surge. The gradual slowdown of the last decade could then be interpreted as the glacier approaching the quiescent phase of the surge cycle. However, without evidence of prior fast flow events or any other periodic oscillations in ice motion, we cannot conclude that the present behaviour is cyclic in nature. Rather than the standard definition of a surge, driven by periodic changes in subglacial hydrology or basal thermal regime (Murray et al., 2003), an alternate explanation is that the glacier terminus underwent a single brief period of unstable advance associated with perturbations in bedrock topography.

The fact that velocity patterns remained spatially consistent throughout the study period underlines the role of bedrock features, including topographic highs and basal overdeepenings, in modulating ice motion. We suggest that what was interpreted as the start of a surge in the 1950s may have at least in part been initiated by the terminus advancing into previously unglaciated terrain in an area favourable to the development of fast flow conditions. The

initial thickening observed by Müller (1969) was likely triggered by mass buildup due to downstream resistance to flow where flowlines converge over the bedrock bump south of the nunatak. Fast flow first developed over the ridge in the 1950s, and was likely further encouraged once the terminus advanced into an overdeepening below sea level. The brief drop in the rate of terminus advance at the end of the 1960s, as well as the current position of the ice front at the mouth of the fjord, may both be related to the presence of basal and lateral pinning points which stabilise the terminus and therefore control the rate of frontal advance. This interpretation could explain the sudden and localised changes in ice dynamics at the ice front in the 1950–60s, although it fails to explain the continued advance over the last seven decades.

The uninterrupted advance and relatively high flow rates along the entire length of the glacier do not in themselves provide evidence of surging or other unstable flow behaviour. Without additional observations of ice surface velocities above the terminus region spanning the initiation of fast flow conditions in the 1950–60s, we are unable to confirm whether the sudden speedup was related to a dynamic instability involving the entire length of the glacier, or rather a localised response to perturbations in basal topography. However, if it were a temporary instability such as a surge or surge-like event, flow rates would have eventually dropped as a result of surface drawdown and the rapid transfer of mass towards the terminus. Additionally, the localised velocity peak remained a permanent feature, constrained over the bedrock bump, indicating continued mass input from upglacier throughout the advance. In this perspective, it is somewhat analogous to flow through an icefall, where permanent fast flow develops as a result of stress buildup at the boundary between areas of high and low basal drag.

The key point is that the behaviour of GF was, and still is, out of sync with similar ice masses in the Canadian Arctic, and with current climatic conditions. At this point, there is no evidence to suggest that the large-scale mass flux of GF deviates from steady-state flow conditions, and more investigations are required to determine the role of long-term mass balance trends in driving the ongoing advance. Whether the result of a dynamic instability, or a delayed response to past (positive) mass balance conditions, these observations confirm the fact that not all glaciers in the CAA respond in the same way to similar environmental forcings. Identifying the factors causing this variability in ice motion is required to improve understanding of how glacier dynamics might evolve in a changing climate.

3

Strategies for mapping remote glaciers using photogrammetry techniques in suboptimal conditions

ABSTRACT Structure from motion (SfM) photogrammetry coupled with multiview stereo (MVS) techniques is widely used for generating topographic data for monitoring change in surface elevation, however conducting aerial surveys in some remote field locations presents a series of challenges which can significantly impact the quality and reliability of the final products. Field sites such as the glaciers and ice caps of the Canadian High Arctic often offer suboptimal conditions, including large survey areas, complex topography, changing weather, difficult light conditions, and reduced satellite performance. Here, we outline the entire workflow, from data acquisition to SfM-MVS processing, using case studies focused around two small glaciers in the Canadian Arctic. We provide recommendations for the selection of photographic and positioning hardware and guidelines for flexible survey design using direct measurements of camera positions, thereby removing the need for ground control points. The focus is on maximising hardware performance despite inherent limitations, with the aim of optimising the quality and quantity of the source data, including image information and control measurements. We demonstrate processing steps for generating high resolution topographic reconstructions and orthomosaics of the two surveyed sites and for optimising results despite suboptimal conditions.

3.1 INTRODUCTION

In the last couple of decades, digital photogrammetry techniques have become more accessible, enabling the rapid acquisition of high resolution topographic information at low cost (e.g. Westoby et al., 2012; Fonstad et al., 2013; Smith et al., 2016a; Anderson et al., 2019). The use of structure-from-motion (SfM) algorithms coupled with multiview stereo (MVS) computer vision methods has become widespread in glacier monitoring as a tool for mapping ice extent and surface topography, and for quantifying ice volume change through time (Mölg and Bolch, 2017). As an image processing technique, SfM relies on matching features detected on multiple overlapping 2D images to estimate camera motion and the position of these given features in a 3D point cloud. MVS algorithms complement

the workflow and generate high resolution topographic reconstructions. In glacier studies, air photos acquired from single and repeat airborne surveys can be used to create digital elevation models and orthophotos representing the glacier surface. These reconstructions are useful tools for tracking ice motion (Immerzeel et al., 2014; Chudley et al., 2019; Jouvet et al., 2019), monitoring calving dynamics (Ryan et al., 2015; Jouvet et al., 2017, 2019), quantifying elevation changes and surface ablation (Bash et al., 2018), and mapping surface topography (Smith et al., 2016b), crevasse patterns (Thomson and Copland, 2016), supraglacial drainage networks (Rippin et al., 2015), and debris cover (Kraaijenbrink et al., 2016, 2018).

The flexibility of the SfM-MVS technique implies that methods, including survey design, processing steps, and settings used, differ between studies. As there is no consistent methodology, efforts have been made towards establishing general guidelines for a standardised workflow with rigorous error reporting strategies for the use of SfM in the geosciences (e.g. James et al., 2019). A number of publications summarise best practices in terms of survey design and data acquisition for optimal results under optimal conditions, including the choice of airborne platform, photographic and positioning hardware, image network geometry, and image capture settings (e.g. Eltner et al., 2016; Smith et al., 2016a; Mosbrucker et al., 2017). In theory, proper planning and careful survey design can minimise measurement errors, but in reality, several interacting factors in the field can influence the quality of final outputs, making it difficult to predetermine expected errors and identify the factors with the largest impact on accuracy. This is especially crucial where field data acquisition is performed in suboptimal conditions, and where careful survey planning is impractical or impossible as is often the case when surveying glaciers in remote locations such as, for example, the Canadian Arctic.

Accurate determination of glacier change requires detailed measurements of changes in ice volume to determine geodetic mass balance, but observations of ice extent and surface elevation change over individual glaciers remain sparse in the Canadian Arctic Archipelago (CAA). In situ measurements are time-consuming, logistically expensive, and essentially impossible to implement on more than a limited sample of glaciers. Yet, the rapid ice loss occurring on small high arctic glaciers (Sharp et al., 2014; White and Copland, 2018; Curley et al., 2021) underlines the need for improving ice surface elevation estimates, and for datasets capable of resolving small-scale changes at repeat intervals on often difficult-to-access glaciers. Air photo surveys have the potential to produce digital elevation models at high spatial and temporal resolution over large areas, and to therefore address this data gap. However, to date SfM-MVS has only been applied to two glaciers in the CAA (Thomson and Copland, 2016; Bash et al., 2018), despite this region containing the largest glaciated area in the world outside of the ice sheets.

Conditions are often suboptimal for conducting air photo surveys in the CAA due to large survey areas, rugged terrain, changing light conditions, lack of contrast over snow-covered glaciers, poor satellite reception, and proximity to the magnetic north pole that limits the operation of remotely piloted aircraft systems (RPAS) or unmanned aircraft systems (UAS). Here, we present a set of guidelines for flexible survey design in suboptimal conditions, where the aim is to optimise data acquisition and ultimately minimise the impacts of adverse fieldwork conditions on model results. For this, we use data from two air photo surveys flown from helicopters in the summers of 2018 and 2019, and build centimetre-scale digital elevation models (DEMs) and red-green-blue (RGB) orthomosaics for two small ice masses in the northern CAA (Fig. 3.1). In both cases, data acquisition was performed in less than ideal settings. In the following sections, we:

1. Describe the study sites and inherent challenges to designing an air photo survey while optimising flexibility and efficiency in remote regions.
2. Discuss key elements in hardware selection for the imaging and positioning systems.
3. Describe the survey setup and data acquisition process, including image capture and control measurements.
4. Outline processing steps to optimise image and positioning data prior to running the SfM reconstruction, including image enhancements for increased contrast and details, and camera position estimates and associated uncertainties from raw global navigation satellite system (GNSS) measurements.
5. Outline the SfM-MVS workflow and generate optimised orthomosaics and DEMs which can be used for glacier change detection.
6. Provide recommendations for optimising results for air photo surveys in suboptimal conditions.

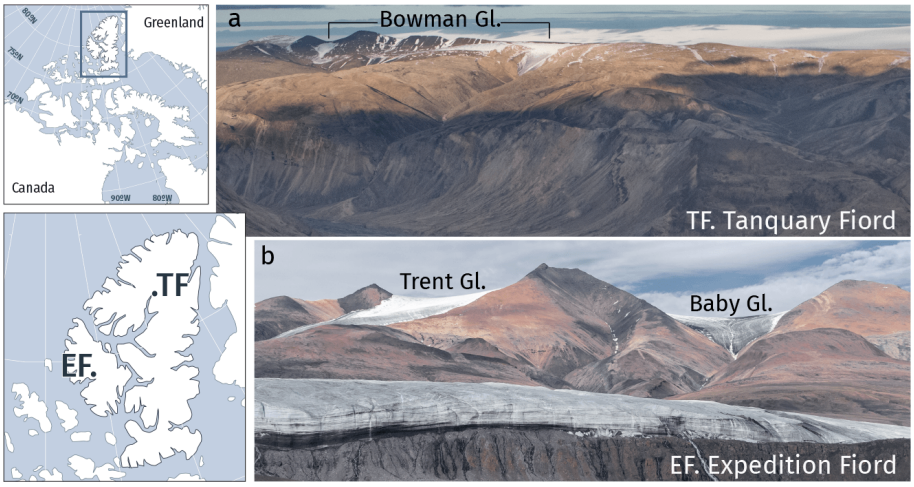

Figure 3.1. Location and overview of **[a]** Bowman Glacier, Tanquary Fiord (TF), Ellesmere Island (03 Aug. 2018) and **[b]** Adams Icefield, Expedition Fiord (EF), Axel Heiberg Island (11 July 2015).

3.2 STUDY SITES AND GENERAL SURVEY DESIGN

3.2.1 Survey sites and general challenges

The two glaciers surveyed in this study constitute challenging study sites for photogrammetry as the survey areas are spread over large elevation ranges and include steep ice and narrow valleys. Varying surface properties with a mix of snow, ice, and bare rock over rugged topography result in highly variable light conditions, changing between areas of bright snow and dark shadows. Satellite navigation represents an additional challenge at high latitudes as it can be unreliable and limited by satellite coverage and visibility, satellite-receiver geometry, and the increased impact of ionospheric effects (Leick et al., 2015; Hugentobler and Montenbruck, 2017; Langley et al., 2017).

The first study area is Bowman Glacier (81.35ºN, 76.45ºW; Fig. 3.1a), a small mountain glacier ∼10 km southeast of the Parks Canada basecamp at the head of Tanquary Fiord on northern Ellesmere Island. The glacier covers an area of <1 km^2 at an elevation range between ∼900 and ∼1200 m above sea level (a.s.l.) (Fig. 3.2a). The survey at Tanquary Fiord (henceforth referred to as the TF survey) was flown on 3 August 2018 onboard an Airbus ASTAR

350 B2 helicopter (Fig. 3.3). We covered 85 km of flightlines during an approximate flight time of 50 minutes, surveying a ∼70 km^2 area around Bowman Glacier and the main three valleys in its drainage basin (Fig. 3.2a). The survey took place around 2100–2200 local time, when the sun was quite low on the horizon, which resulted in long shadows and shooting images directly into the sun at times.

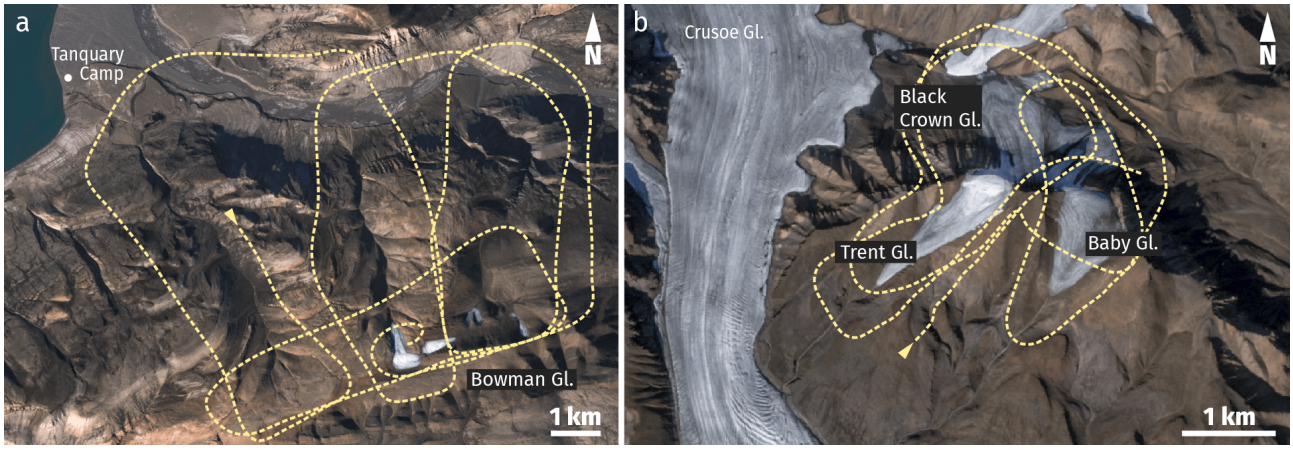

Figure 3.2. Flightpath of the **[a]** Tanquary Fiord (TF) and **[b]** Expedition Fiord (EF) air photo surveys. Base images: Sentinel 2A, July 2020.

The second site is Adams Icefield (79.44ºN, 90.59ºW; Fig. 3.1b), a small icefield in Expedition Fiord, on the western coast of Axel Heiberg Island. Covering an area of ∼3 km^2 at an elevation of ∼700–1200 m a.s.l., the icefield is composed of three mountain glaciers (Baby, Trent, and Black Crown), which flow down either side of a ridge formed by three peaks, each reaching 1100–1250 m a.s.l. (Fig. 3.2b). The Expedition Fiord survey (henceforth EF survey) was flown on 10 July 2019 onboard a Bell 206L Long Ranger helicopter (Fig. 3.3), covered a considerably smaller area of ∼10 km^2 and was surveyed in 20 minutes over 30 km of flightlines (Fig. 3.2b). Although the flight occurred around noon local time, one of the glaciers is north-facing and was therefore partially in shadow, and isolated patches of low clouds moving across the glaciers introduced an additional difficulty.

3.2.2 Airborne platform

Remotely piloted aircraft systems are becoming an increasingly common tool for performing aerial surveys, with a major advantage being the much lower acquisition and operation costs of remotely piloted aircrafts compared to the cost of chartering manned aircrafts. However, both fixed-wing and multi-rotor remotely piloted aircrafts have limitations, including limited payload and horizontal and vertical range. Large survey areas, complex topography, rugged terrain, and challenging weather patterns (including high winds, low temperatures, and atmospheric icing conditions) also represent major obstacles to RPAS operations in glaciated regions (e.g. Gaffey and Bhardwaj, 2020). Perhaps the most significant limitation is the performance of control systems and autonomous navigation: RPAS typically rely on magnetic sensors for attitude determination during navigation, but these can be severely compromised in proximity to the magnetic poles. This issue has been particularly problematic in our study region, where previous tests with at least five different RPAS have resulted in almost immediate crashes following the failure of the magnetic orientation system due to the proximity of the magnetic north pole (at times within 1000 km from Tanquary and Expedition fjords). Manned aircrafts, and particularly helicopters, are therefore the only viable

option in our study area. Major advantages of manned aircrafts include their high payload (often up to ∼1000 kg), which allows for the use of larger and higher performance photographic and positioning equipment than is typically possible with remotely piloted aircrafts, and their greater flight range.

3.2.3 Imaging system

For both surveys in this study, images were captured with the Nikon D850 digital single lens reflex (DSLR) camera, a high-resolution (45.7 megapixels) full frame (35 mm) model with a backside illuminated complementary metal oxide semiconductor (BSI CMOS) sensor. The camera was coupled with a prime lens with a fixed focal length of 24 mm and maximum aperture of f/1.8 (NIKKOR AF-S 24mm f/1.8G ED). Image quality primarily depends on the camera/lens combination and its ability to resolve fine details in all environmental conditions, regardless of ambient light or surface properties. Imaging systems with interchangeable lenses, including DSLRs and mirrorless cameras, are more flexible in terms of hardware selection and image capture settings, and therefore offer more control over data acquisition than compact cameras fitted on most consumer-grade remotely piloted aircrafts. In addition, the reduced sensor size of smaller compact cameras often translates into smaller pixel size, a key factor impacting the signal to noise ratio and the level of detail available in shadows and highlights (Rowlands, 2017). Along with focal length, sensor size also defines the ground sampling distance (GSD) and therefore the spatial resolution and maximum achievable precision of the resulting topographic reconstruction. High resolution imaging systems such as the one used in this study allow for increased flight height while ensuring sufficiently high spatial resolution. This maximises survey range and enables more efficient coverage of larger areas with fewer flightlines and/or overlapping images (Smith et al., 2016a).

3.2.4 Positioning system

The accuracy, quantity, and distribution of control measurements have a direct impact on georeferencing quality, and the accuracy of topographic products derived from SfM-MVS processing techniques. Georeferencing can be achieved either indirectly using GNSS measurements of ground control points (GCPs), or with direct GNSS measurements of camera positions synchronized with image capture. The indirect (ground-based) approach requires an appropriate number (usually at least five) of well-distributed targets or distinct features on or off the ice surface, which are then manually aligned on the captured images that they are visible in. While GCPs provide precise coordinates, the acquisition and processing of these points can be the most time-consuming steps in the workflow, and it is impractical to have many (or even any) in large and difficult to access survey areas. The direct method using airborne control measurements represents a major logistical advantage for aerial surveys in remote locations, and has been shown to produce results of similar precision to the ground-based approach where camera position information is acquired with multi-frequency survey-grade GNSS equipment (Nolan et al., 2015). Low cost single frequency GNSS receivers such as those onboard remotely piloted aircrafts generate imprecise positioning solutions, accurate only to several metres. UAV-based aerial surveys relying on integrated GNSS sensors therefore often depend on GCPs for positioning (Carbonneau and Dietrich, 2017). The precision and accuracy of GNSS measurements can be improved in real time kinematic (RTK) mode, but this requires a direct communication link to a fixed base station which restricts the survey area to a limited operating range, and is impractical over large remote glaciers.

In this study, GNSS measurements were acquired using a survey-grade dual-frequency GPS (US satellite constellation only, L1/L2 bands) system consisting of the Trimble R7 receiver and Zephyr 1 Geodetic antenna. Following the strategy of Nolan et al. (2015), we acquired direct measurements of camera positions by synchronising the GPS receiver with the camera shutter via wired connection using the Trimble Event Input Marker and 1 PPS Output device (Fig. 3.3d). We additionally recorded the position of a number of targets on the ground around both surveyed sites, to serve as checkpoints for the direct georeferencing method. We use undifferenced satellite observations from a single GNSS system processed with precise point positioning (PPP). In contrast to differential positioning (i.e., RTK and PPK), PPP requires no fixed reference station and uses precise satellite orbit and clock products to correct for biases in estimated coordinates. Removing the need for a second GNSS system on the ground therefore reduces equipment costs and provides greater operational flexibility in remote areas.

Figure 3.3. Camera position onboard the helicopter during the **[a]** TF and **[b]** EF surveys. **[c]** Image capture during the TF survey, and **[d]** imaging/positioning hardware used at both TF and EF (shown here as used in another survey not part of this study): (1) intervalometer; (2) Nikon D850 camera; (3) Trimble event marker device; (4) Trimble R7 GPS receiver.

3.3 HARDWARE SELECTION

3.3.1 Imaging hardware

In photogrammetry, the key for a high-performance setup dedicated to precision measurements is matching the camera with the right high optical quality lens to ensure maximum image resolution and sharpness, high sensitivity and dynamic range, and to minimise any aberrations and distortions. This section expands on four key elements that should be considered when selecting an imaging system, namely the camera sensor, the lens, signal processing, and camera shutter mechanism.

Sensor size & pixel pitch

A major advantage of full frame (FF) DSLRs like the Nikon D850 is the large sensor size (36×24 mm) compared to a smaller crop sensor such as the common APS-C format (23.5×15.6 mm), or to 1"-type sensors (13.2×8.8 mm) on smaller cameras that fit on most remotely piloted aircrafts. Sensor size generally increases pixel pitch, a metric measured in microns related to the distance from the centre of one pixel (photodiode) to the next. This implies that a larger number of megapixels is not necessarily a plus since, to maintain an equivalent resolution, smaller sensors must have smaller pixels (Table 3.1).

Sensor format	Sensor size (mm)	Resolution (mpix)	Pixel pitch (μm)	Nyquist limit (cy $\ln^{-1}$)	Focal multiplier
1"	13.2 × 8.8	20	2.4	208	2.7
APS-C	23.5 × 15.6	24	3.7	135	1.5
FF low	36 × 24	24	6	83	1
FF high	36 × 24	45.7	4.35	115	1
MF small	43.8 × 32.9	50	5.3	94	0.82
MF large	53.4 × 40	150	3.8	133	0.67

Table 3.1. Comparison of common sensor sizes and respective resolution limits. FF: full frame; MF: medium format. The Nikon D850 fits in the FF high category.

Sensitivity Pixel pitch is directly related to full-well capacity (i.e., the maximum number of electrons a photodiode can hold at saturation level), which determines the maximum signal to noise ratio. Reduced pixel size tends to increase overall sensor noise, resulting in reduced sensitivity and low-light performance. Smaller pixels require longer exposure times (Nakamura, 2006; Rowlands, 2017) and can therefore be a limiting factor for surveys undertaken from a moving platform and/or in suboptimal conditions, resulting in underexposed images or motion blur. However, as sensor design is a constantly evolving technology, two sensors of different generations with similar size and pixel count might not reach the same level of performance, with newer generation designs often outperforming older ones. Recent developments in CMOS technology, and the introduction of backside illuminated (BSI) sensors, for example, have resulted in significant improvements in low-light sensitivity particularly for small pixel sensors. Unlike standard front illuminated sensors, in BSI the wiring has been moved behind the photodiode, increasing the photosensitive detection area (the photosite) and improving full-well capacity (Ohta, 2020). Originally used in smartphones, BSI technology has recently been introduced in APS-C CMOS sensors, with the Nikon D850 being one of the first FF DSLRs benefitting from the technology. Full-well capacity has an additional effect on dynamic range (i.e., range of luminance values in an image) which determines performance in high contrast environments

(Nakamura, 2006; Rowlands, 2017). This is especially important where the intensity difference between a bright glacier surface and the darker bare ground along the margins is amplified by low sun angles and long shadows on the surface.

Most consumer cameras record 8–12 bits per channel, while higher performance imaging systems, including the Nikon D850, use higher resolution 12–14 bit depth data. The raw digital information can be saved without compression (preserving the original bits) in RAW image format, and/or converted through nonlinear encoding and compressed into standard 8-bit image files, typically TIFFs or JPEGs. Raw bit depth dictates the number (and size) of quantisation steps available for encoding digital data, which directly translates to tonal precision, or the number of tonal levels in an image (Yoshida, 2006; Rowlands, 2017). With a 14-bit resolution, the D850 records raw image data with 214 tonal levels per channel, significantly more than the 28 values of an 8-bit camera. The high bit depth therefore allows subtle tonal variations to be more faithfully resolved, which becomes particularly crucial in low contrast conditions and uniform surfaces such as in snow covered areas.

Resolution The modulation transfer function (MTF) is a performance metric used to describe the resolving power of an imaging system, or the ability of a camera and lens combination to reproduce fine detail at characteristic spatial frequencies. Pixel pitch (and the detection area) is the primary factor dictating the theoretical maximum resolution (or resolving power) of an imaging system. Resolution, which stands for spatial frequency, is typically defined in units of cycles (or line pairs) per mm (cy mm^{-1} or lp mm^{-1}), corresponding to the number of light/dark line pairs that can be properly resolved per unit on the focal plane (the sensor). The maximum achievable resolution is limited by the detector cut-off frequency, equivalent to twice the Nyquist frequency (0.5 cy px^{-1}) at which point the sensor MTF drops to zero and no further information can be resolved (Palum, 2009; Rowlands, 2017). Above the Nyquist frequency, an imaging system is unable to properly resolve fine details without introducing aliasing artefacts (also called moiré). With the exception of medium and large format professional cameras, many high resolution cameras were, until recently, equipped with an optical lowpass filter (or antialiasing filter) in order to minimise aliasing noise when capturing fine repetitive detail (e.g. lines or dots) above the detector Nyquist frequency. The filter cuts high spatial frequency information before it reaches the detector, essentially blurring the image and causing some resolution loss (Palum, 2009). Since patterns causing moiré are virtually absent in nature, lowpass filters are only a downside for aerial photogrammetry applications where maximum image sharpness is key. Higher pixel count and smaller pixel pitch reduce the chance of moiré, therefore lowpass filters are generally absent on cameras with smaller (non-FF) sensors and are increasingly being abandoned on newer DSLRs (including the D850) and mirrorless cameras as sensor resolution increases (Palum, 2009).

With a pixel pitch $\rho = 4.35$ µm, the detector cut-off frequency ($v_c = 1/\rho$) on the D850 is equivalent to 230 cy mm^{-1}, which places the Nyquist limit at 115 cy mm^{-1} (Fig. 3.4). This is roughly 30% higher than the 166 cy mm^{-1} cut-off frequency of a standard lower resolution FF camera such as the Nikon D750 with 24 megapixels and a pixel pitch of 6 µm. As sensor MTF is the product of detector and filter MTFs, the addition of the lowpass filter on the D750 further limits maximum system resolving power and lowers the cut-off to the Nyquist frequency of 83 cy mm^{-1} (Fig. 3.4). This implies that system resolving power increases with decreasing pixel size, although system cut-off frequency is ultimately determined by whichever component (detector/sensor or lens) has the lowest cut-off (Palum, 2009; Rowlands, 2017).

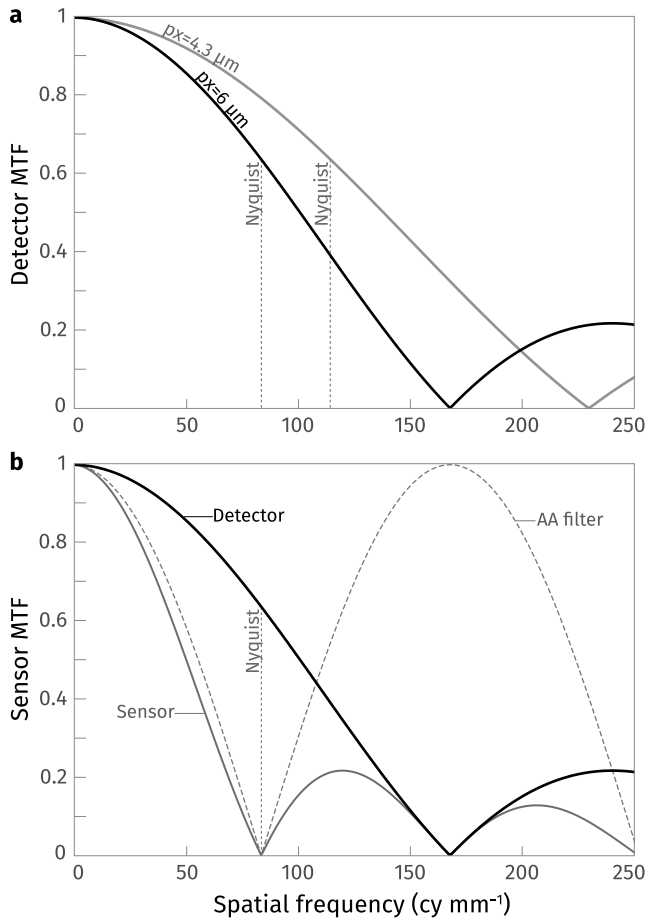

Figure 3.4.
[a] Detector frequency response as a function of pixel pitch alone for a full frame high resolution (45.7 megapixel) sensor (Nikon D850; grey line), and a full frame lower resolution (24 megapixel) sensor (Nikon D750; black line).
[b] Sensor frequency response for the D750 with the addition of a lowpass (antialiasing: AA) filter. Here, the pixel detection area is assumed to be equivalent to pixel pitch ρ= 4.35 µm (D850) and ρ= 6 µm (D750). This places the detector cut-off frequency ($v_c = 1/\rho$) at 230 cy mm^{-1} (D850) and 166 cy mm^{-1} (D750), and the Nyquist frequency at 115 cy mm^{-1} (D850) and 83 cy mm^{-1} (D750). The sensor modulation transfer function (MTF) is the product of both detector and antialiasing filter MTFs, with the cut-off coinciding with the Nyquist frequency (83 cy mm^{-1}). Notice how the addition of the AA filter also lowers the sensor MTF below the Nyquist frequency.

Lens performance

Lens MTF response is evaluated in terms of relative contrast as a function of frequency and depends on two main factors: diffraction and aberrations. In theory, a perfect lens is said to be diffraction limited (i.e., resolving power depends on diffraction alone), however, in reality, all lenses suffer from various imperfections which combine to lower the real-world lens MTF (Ray, 2002; Rowlands, 2017).

Diffraction Diffraction occurs as light passes through a circular aperture, causing waves to bend around the edge and preventing them from converging to a single point on the focal plane. Diffraction produces an Airy disk pattern (consisting of a central spot surrounded by concentric circles), which causes blurring and sets a fundamental limit on the maximum achievable resolution determined by sensor design (Rowlands, 2017). Diffraction is a function of the wavelength of the incoming light (λ), focal length (f), and aperture diameter (D), with f/D giving the f-number (N), sometimes called f-stop. By definition, the diffraction limit decreases with smaller apertures (Rowlands, 2017). Figure 3.5 shows the cut-off frequency ($\nu_c = 1/\lambda N$) and lens MTF as a function of spatial resolution (ν) for an aberration-free lens with a circular aperture given by:

$$MTF_{diff} = \frac{2}{\pi}\left[cos^{-1}\left(\frac{v}{v_c}\right) - \frac{v}{v_c}\sqrt{1-\left(\frac{v}{v_c}\right)^2}\right] \tag{3.1}$$

For example, taking the middle wavelength of natural (green) light at ∼550 nm, and an aperture of f/4, puts the diffraction limited frequency at 455 cy mm^{-1}. As this is higher than the detector cut-off frequency of 230 cy mm^{-1} calculated for the D850, the system resolving power is limited by sensor resolution. However, stopping down to f/8 reduces the limit to 227 cy mm^{-1} at which point the system resolving power becomes diffraction limited (Fig. 3.5a). Taking into account various aberrations further lowers lens MTF and therefore system resolving power.

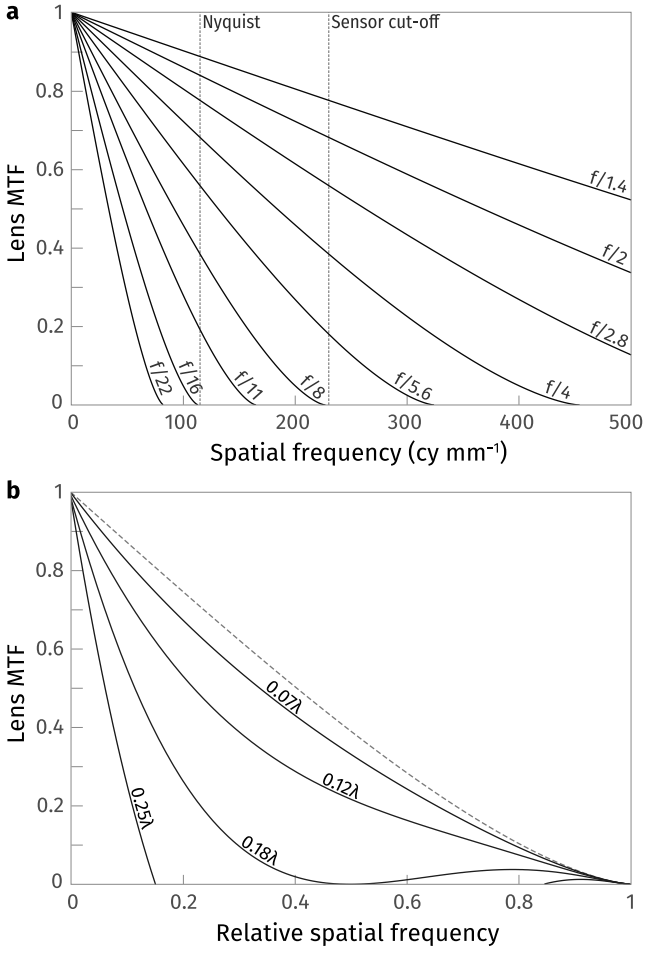

Figure 3.5.
[a] Lens modulation transfer function (MTF) as a function of spatial frequency for a diffraction limited (aberration-free) lens with a circular aperture at various f-numbers. The cut-off frequency (or in this case the diffraction limit: $\nu_c = 1/\lambda N$) is calculated for green light with a wavelength of ∼550 nm. The sensor cut-off and Nyquist frequencies (two dotted vertical lines) are those calculated for the Nikon D850, with a pixel pitch of 4.35 µm and no antialiasing filter.
[b] Lens MTF normalised for cut-off frequency with varying amounts of wavefront aberrations with RMS errors W_{RMS} in units of wavelength. The dashed line corresponds to a diffraction limited (aberration-free) lens.

Aberrations Aberrations are inherent to lens design and occur where light fails to converge at a single point on the focal plane or along the optical axis. Chromatic aberrations result from different wavelengths focusing at different positions on the focal plane causing colour fringing, most often visible as purple artefacts along high-contrast boundaries (Ray, 2002). Monochromatic aberrations include spherical aberrations, coma, astigmatism, and field curvature, all of which cause blur and contrast reduction. With the exception of spherical aberrations which affect the entire image, the other types tend to vary with field position and intensify as a function of distance from the optical axis (Ray, 2002). Lens MTF response therefore follows the same pattern and contrast reproducibility is typically highest at the centre of the frame and degrades towards the edges. While lenses tend to lose significant contrast to diffraction effects at small apertures (large f-numbers), aberrations are amplified at large apertures (small f-numbers). Therefore, the optimum aperture for maximum performance hovers around two to three stops up/down from their maximum/minimum aperture, respectively, typically around f/4 to f/5.6 (Ray, 2002).

The effects of aberrations on lens MTF can be approximated using an empirical model relating the diffraction limit to the amount of residual (root mean square: RMS) wavefront error (W_{RMS}) resulting from defocus and spherical aberrations combined (Shannon, 1995). The aberration transfer function is approximated with:

$$MTF_{aberr} = \left[1 - \left(\frac{W_{RMS}}{0.18}\right)^2 \left(1 - 4\left(\frac{v}{v_c} - 0.5\right)^2\right)\right] \tag{3.2}$$

and combined with the diffraction transfer function to give the lens MTF:
$MTF_{lens} = MTF_{diff} \times MTF_{aberr}$ (Shannon, 1995). Figure 3.5b illustrates the effect of various amounts of aberrations on lens MTF. Deviations of 0.25 wavelengths (RMS) are common in commercial lenses, while RMS wavefront errors of <0.15 are seen in high quality optics. A lens with RMS values of <0.07 wavelengths can be considered as essentially diffraction limited, as aberrations are virtually unnoticeable (Shannon, 1995).

System resolution Ultimately, system MTF is the product of the transfer functions of all individual components combined:

$$MTF_{syst} = MTF_{sensor} \times MTF_{diff} \times MTF_{aberr} \tag{3.3}$$

where $MTF_{sensor} = MTF_{detector} \times MTF_{AA}$. The system MTF has implications for determining the spatial resolution of any data products derived from images captured at a given aperture. Spatial resolution is often thought of as equivalent to the ground sampling distance (GSD), or distance between two consecutive pixel centres on the ground, calculated with:

$$GSD = \frac{H \times \rho}{f} \tag{3.4}$$

where H is height above ground level (a.g.l.), ρ is pixel pitch, and f is focal length. The GSD indicates the minimum size of a detail that can be resolved on an image, assuming that the resolution limit coincides with the spatial frequency where the sensor MTF drops to zero and omitting the influence of imaging optics or motion blur on system resolving power. Besides, the zero MTF limit is rather theoretical since, in reality, the effective cut-off frequency where resolution is sufficiently high for an image to retain any useful information is around an MTF of 9%, as implied by the Rayleigh criterion (Rowlands, 2017).

From a spatial domain point of view, diffraction becomes gradually more visible as the size of the Airy pattern (also called circle of confusion) on the focal plane increases relative to pixel pitch, and is generally tolerable up to 1.5 pixels. Based on the Rayleigh criterion, the effective cut-off frequency corresponds to the point where two Airy disks are no longer resolvable, that is, where the distance between the centres of two disks is equal to their radius: $1.22 \times \lambda N$ (Rowlands, 2017). In other words, the system becomes diffraction limited when the circle of confusion reaches a size of twice the pixel pitch ($2 \times (1.22 \times \lambda N) \geq \rho$). Therefore, taking into account diffraction effects should place a limit to the GSD equivalent to the size of the circle of confusion, giving a diffraction limited GSD of:

$$GSD_{diff} = \left(1.22 \times H \times \frac{\lambda}{D}\right) \times 2 \tag{3.5}$$

which varies with different f-numbers (Fig. 3.6). With the Nikon D850 and 24 mm lens, $\rho = 4.35$ µm, $f = 24$ mm, and taking $H = 500$ m, the GSD is 90 mm. With an aperture $N =$ f/4.0, $D = 6$ mm, and with $\lambda = 550$ nm, the

GSD_{diff} is 112 mm, meaning, despite some amount of image degradation, the optics are not limiting the GSD. However, take N = f/8 and D = 3 mm, GSD_{diff} becomes 224 mm and so the base GSD of 90 mm cannot be properly resolved. Naturally, this still represents an idealised scenario, applicable to a system with perfect optics. In general, smaller consumer cameras are more likely to have lower quality optics with greater wavefront aberrations further lowering the GSD, especially so at larger apertures. Independently from the quality of the system itself, motion blur due to camera motion combined with slow shutter speeds can put an additional limit on the GSD.

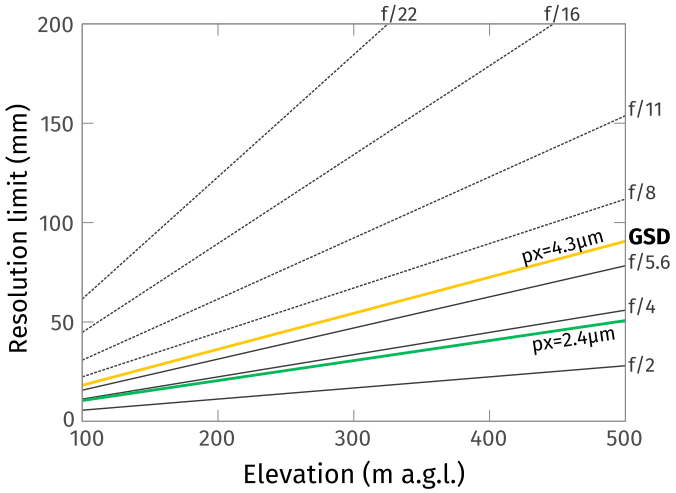

Figure 3.6. Diffraction limited ground sampling distance (GSD) at various f-numbers as a function of flying height above ground surface. The thick lines represent the standard definition of GSD based on the sensor cut-off frequency for the Nikon D850 with a pixel pitch of 4.35 µm (yellow line), and for a standard 1" sensor with a pixel pitch of 2.41 µm (green line). At H = 500 m above ground level, the D850 is (at best) able to resolve two objects 90 mm apart. Taking into account diffraction at f/8, the system can only resolve two objects up to 112 mm apart and so the theoretical GSD becomes limited. In comparison, the smaller 1" sensor is already limited at f/4.

Focal length Focal length, the distance between the optical centre of the lens and the focal plane, defines the angular field of view and object magnification for a given lens. Wide angle lenses (35 mm or less) such as the NIKKOR 24mm f/1.8 used here are well suited for aerial photography as they allow the capture of more of the scene in a single image, compared to longer lenses with a narrower field of view (Smith et al., 2016a). Effective focal length refers to the field of view of a system taking into account different sensor sizes, calculated by applying a focal length multiplier. Sensors smaller than the standard 35 mm FF format introduce a crop factor, meaning that a 24 mm lens coupled with an APS-C sensor will have an effective focal length of 24 mm multiplied by 1.5 (or 1.6 for Canon cameras), equivalent to 36 mm on a FF (35 mm no crop) sensor. Smaller sensors therefore require wider lenses for a given field of view, the downside being that short focal lengths are more prone to distortions which can affect measurement accuracy (Rowlands, 2017).

Unlike aberrations causing blur, optical distortions have no direct effect on lens MTF and cannot be compensated for by stopping down the aperture. Distortions arise from variations in magnification with field position and affect image geometry by causing straight lines to appear curved. Wide angle lenses exhibit negative (barrel) distortions which present as decreasing image magnification from the centre of the frame towards the edges, while positive (pincushion) distortions are characteristic of telephoto lenses (70 mm or above). The amount of distortion corresponds to the difference between the real image and the theoretical (undistorted) one, often reported as a percentage of image height, and generally intensifies with increasingly short/long focal lengths (Ray, 2002). Extreme wide angle and fisheye lenses such as those found on action cameras (e.g. GoPro), are therefore unsuitable for photogrammetry applications due to extreme distortions (Smith et al., 2016a). For aerial photography, effective focal lengths between 24 and 35 mm represent a decent compromise between field of view (62–84º) and optical quality.

Prime lenses with fixed focal lengths typically have higher quality optics (and therefore lower aberrations) when compared to zoom lenses at a similar price point. This is mainly because zoom lenses require more complex designs to accommodate a range of focal lengths, while prime lenses are designed for maximum performance at a specific focal length. Since aberrations tend to vary with focal length, prime lenses are by definition more suitable for applications requiring repeatable measurement (Koyama, 2006). Lens performance is even more important with smaller sensors as diffraction effects become increasing problematic with decreasing pixel pitch.

Signal processing

Converting raw image data into a standard output image format (TIFF or JPEG) with a lower bit depth involves mapping a range of raw levels to a single tonal value. While this can be achieved without degrading perceived image quality by applying a nonlinear tone curve, it can also result in visible quantisation errors and posterisation, where continuous gradients appear as a series of discrete tonal transitions (or apparent banding) (Yoshida, 2006; Rowlands, 2017). In addition to a lower bit depth, the JPEG format uses lossy compression which can introduce visible rounding errors and unwanted digital artefacts, most notably blocking and ringing. While block artefacts are particularly noticeable in relatively uniform areas with smooth colour gradients, ringing artefacts blur edges and impact sharp object boundaries (Yoshida, 2006). In-camera raw conversion essentially involves a series of irreversible adjustments designed to improve perceived image quality, including noise reduction, sharpening, aberration corrections, tone and colour mapping, and contrast enhancements. One of the main drawbacks of such a conversion process is the loss of luminance information and amplified quantisation errors, mainly in dark shadow areas (Rowlands, 2017). Selecting a camera with a high bit depth (12–14 bits) and the ability to shoot in RAW format maximises available image information and provides considerably more control over tonal and colour reproduction. Increased flexibility in postproduction allows for taking advantage of the full tonal range and retrieval of dark levels which would otherwise be lost during in-camera raw conversion (Fig. 3.7).

Using a wide colour space such as Adobe RGB 1998 or ProPhoto RGB also increases the range of available colours compared to the standard sRGB gamut. Typically used as the default with JPEG images, the sRGB colour space encompasses ∼35% of all visible colour combinations, versus ∼50% for Adobe RGB 1998, and ∼90% for ProPhoto RGB. The ProPhoto RGB gamut, which is comparable to the RAW camera colour space, preserves more colours as captured by the sensor and requires working with 16-bit TIFF images to prevent posterisation (Rowlands, 2017). Where working with the RAW image data is not possible, in-camera processing of image information should be minimised (e.g. picture mode set to ‘flat’ or ‘neutral’, colour space to Adobe RGB) and any adjustments should be disabled in camera settings. Additional corrections applied to spatial image information can be especially detrimental to photogrammetry applications. For example, in-camera raw conversion also includes corrections targeting geometric (mainly radial) distortions which alter pixel geometry (Rowlands, 2017) and can impact the camera calibration process performed by the camera model implemented in photogrammetry software (Brown, 1971; Fraser, 2013). Any additional image processing steps with the potential to modify image and/or pixel geometry should be avoided, including any optical or digital image stabilisation techniques (also called vibration reduction).

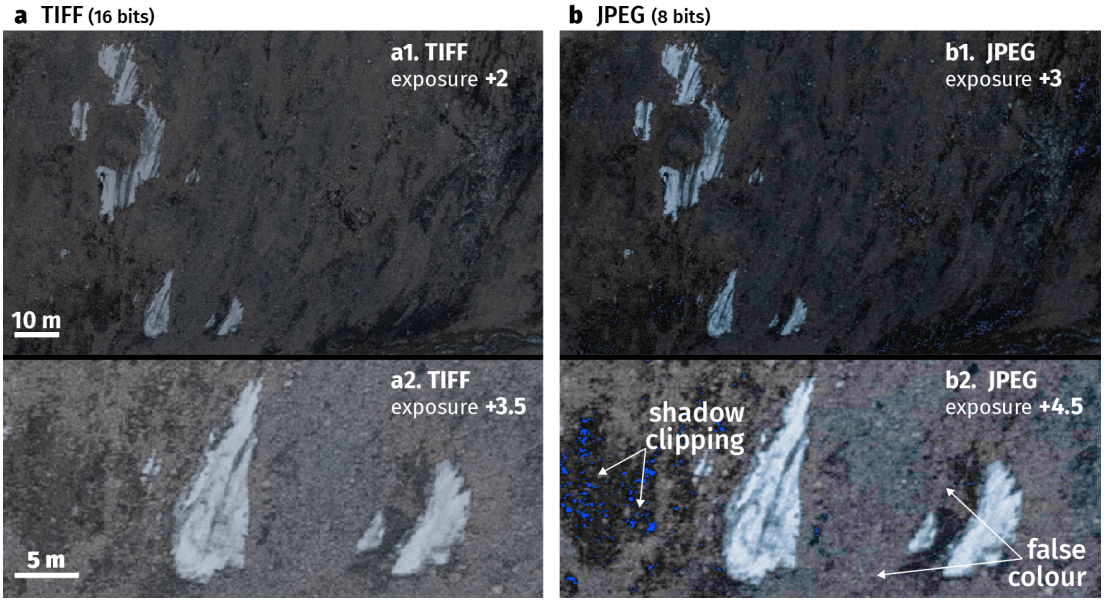

Figure 3.7. Exposure adjustments performed **[a]** directly on an underexposed 14-bit RAW image (subsequently exported as 16-bit TIFF), and **[b]** on the same image initially exported as an unedited 8-bit JPEG. Stronger adjustments are required for the JPEG (b1) to reach a comparable overall level of exposure and retrieve an equivalent amount of information to the TIFF image (a1). With more extreme adjustments, the TIFF image (a2) remains useable, while on the JPEG (b2) some information is lost in the darker shadows (bright blue pixels) and compression artefacts and false colour (purple patches) combine to degrade image quality.

Shutter

Most DSLRs, including the D850, are equipped with CMOS sensors which conventionally use mechanical vertical travel focal plane shutters, also called rolling shutters. Focal plane shutters have rigid-blade curtains which travel across the sensor at a constant rate independent of exposure time. The front curtain starts opening at the beginning of the exposure, and the rear one travels behind it after a delay equivalent to the shutter speed. The vertical travel time corresponds to the flash synchronisation speed (or X-sync speed) which is the fastest speed at which the shutter is 100% open (1/250 s for the D850). Scanlines on the sensor array are exposed and read out sequentially over the timespan corresponding to the sum of the vertical curtain travel time and the exposure time. As a result, the exposure timing of individual pixel rows shifts across the frame. When capturing moving images this rolling shutter effect can lead to geometric distortions. Assuming that shutter motion is orthogonal to the direction of travel (camera in landscape mode), motion trace has a shearing effect where straight lines appear skewed. On the other hand, where shutter motion is parallel to aircraft motion (portrait mode), as is the case in this study, the resulting image will either be compressed or stretched, depending whether the shutter curtains open and close towards or away from the direction of travel. Including the affinity and non-orthogonality coefficients in the camera calibration matrix at the image alignment stage should partially compensate for this effect. In addition, various software including Metashape, have implemented camera models to compensate for rolling shutter effects, however, to our knowledge, algorithms currently involved only deal with cases of orthogonal shutter motion. An alternative for dealing with this issue is to use a global shutter which exposes the full pixel array at the same instant. Electronic global shutters are mainly used with lower-resolution CCD sensors, including in compact cameras and older DSLRs, which are prone to smearing and diffraction effects (blooming), degrading image quality. Large format metric cameras developed for

scientific imaging applications, and those specifically engineered for airborne operations, are often equipped with mechanical global shutters and full frame CCD sensors which offer superior performance, including high dynamic range, but are highly specialised high cost equipment, not easily accessible to the average user.

With an average travel speed of 30 m s^{-1} and an X-sync speed equivalent to 4 ms (1/250 s) for the D850, camera displacement during a single exposure is ∼12 cm. The effect of camera motion on the resulting image can be estimated from the pixel displacement Δ_{px} during the curtain travel (or readout) time obtained by:

$$\Delta_{px} = \frac{v\,t\,f}{\rho H} \tag{3.6}$$

where v is aircraft velocity, t the vertical curtain travel time, f the focal length, ρ the pixel size, and H height above ground surface. Object displacement across an image due to rolling shutter effects should ideally remain below ∼1 pixel. For the D850, with t, f, and ρ equivalent to 4 ms, 24 mm, and 0.43 µm respectively, and the aircraft travelling at an average of 30 m s^{-1} and a height of 500 m a.g.l., object displacement across the image due to the rolling shutter effect averages 1.3 pixels. It is worth mentioning that electronic rolling shutters such as those in compact consumer products typically have much slower (by an order of magnitude) effective vertical travel and readout speeds which amplifies rolling shutter effects. With all things kept equal, but using a compact camera with a typical readout speed of 30 ms, the average object displacement across an image would be closer to 10 pixels.

3.3.2 Postioning hardware

The main advantage of using the direct georeferencing method (i.e., using known camera positions acquired during airborne photo surveys), is that it eliminates the need for a network of GCPs. However, kinematic positioning is typically more vulnerable to disturbances than static GNSS measurements and can produce highly variable results particularly where GNSS performance is less than ideal. The performance of GNSS systems at high latitudes is limited by satellite availability, receiver-satellite geometry, as well as increased ionospheric activity (Leick et al., 2015; Langley et al., 2017; Hugentobler and Montenbruck, 2017). The following section reviews the main factors influencing positioning quality from kinematic GNSS measurements onboard manned aircrafts, namely the performance of the GNSS hardware and its synchronisation with the camera.

GNSS receiver and antenna

Multi-constellation GNSS positioning requires observations from a minimum of four satellites to determine pseudoranges and calculate receiver position and clock offset. For PPP positioning of the type used in this study, a fifth satellite is needed to solve for the tropospheric zenith path delay. The geometric dilution of precision (GDOP) describes the effects of satellite availability and configuration on the overall quality of the solution, with wider spacing between satellites resulting in more accurate positioning (lower GDOP) and tighter, or in-line, geometries degrading positioning accuracy (higher GDOP) (Langley et al., 2017). Satellite geometry is primarily limited by orbital inclination, which dictates the maximum satellite elevation above the horizon at a given latitude. The slightly higher orbital inclination of GLONASS satellites (65º) with respect to GPS, Galileo, and BeiDou (55–56º) is an advantage in polar regions, where GLONASS satellites reach maximum elevations of ∼55º above the horizon, compared to

$\sim$45º for the remaining constellations. Overall, low satellite elevations weaken receiver-satellite geometry resulting in lower vertical position accuracy (higher VDOP). On the other hand, this situation increases satellite visibility in terms of numbers, as more orbital planes are visible at once, which improves horizontal positioning (lower HDOP) (Langley et al., 2017). Multi-constellation GNSS systems therefore benefit from increased satellite availability, which improves solution continuity and accuracy, and ensures stronger satellite geometry, even more so considering the higher orbital inclination of the GLONASS system. This is particularly valuable for kinematic applications where unpredictable motion can cause tracking issues and signal interruptions (Leick et al., 2015).

Multi-frequency Signal propagation is affected by atmospheric (tropospheric and ionospheric) propagation delays, which are amplified for low-elevation satellite signals with longer transmission paths through the atmosphere. First, signal attenuation due to transmission path loss is worse with low-incidence angles, which directly impacts the signal to noise ratio of the code and carrier phase measurements (Kouba et al., 2017; Langley et al., 2017). Second, increased ionospheric activity in the polar regions amplifies and causes more variability in atmospheric delays. As the magnitude of the delay is dependent on signal frequency, multi-frequency observations (such as L1, L2, and L5 for GPS) allow for correction of ionospheric delays (Kouba et al., 2017). GNSS signals at high latitudes are also affected by ionospheric scintillation responsible for causing irregular variability in signal phase and amplitude along the transmission path. Discontinuities in phase measurements can result in cycle slips and jumps in the carrier phase ambiguity, resulting in positioning errors of several metres or complete loss of lock. Multi-frequency observations are also used for cycle clip detection which allows the elimination of outliers and minimisation of positioning errors (Kouba et al., 2017). Multi-frequency receivers using the higher frequency L5 (GPS) band (or other equivalent frequencies from different constellations) have an additional advantage in that higher frequency signals are less affected by ionospheric effects. This results in improved signal strength due to lower overall transmission path loss (Leick et al., 2015).

Multipath mitigation Multipath effects from surface reflectors are one of the main sources of error in GNSS positioning. Errors occur when reflections from multiple sources reach the antenna along with the direct line of sight signal (Leick et al., 2015; Langley et al., 2017). GNSS antennas for geodetic applications are designed to mitigate multipath effects using, for example, variable gain patterns to attenuate low-elevation signals and maximise signal strength at zenith, and different ground plane designs (e.g. choke ring, resistive 'stealth' ground plane) to improve multipath rejection blocking signals arriving from below the horizon (Leick et al., 2015). Onboard aircrafts, satellite signal reception is additionally susceptible to airframe shadowing with the fuselage obstructing the line of sight. One solution is to position the antenna outside the aircraft, but signal dropouts can occur even in open sky conditions, either from the interference caused by helicopter rotor blades, or from disruptions due to aircraft manoeuvring. As the impacts of atmospheric propagation delays, multipath effects, and signal shadowing are particularly problematic with low signal incidence angles, satellites close to the horizon (15º or less) are usually ignored (Leick et al., 2015). However, this can be detrimental to precise positioning if satellite availability is low.

3.4 FIELD DATA ACQUISITION

While knowledge of the theoretical concepts related to photography and GNSS navigation discussed in the previous section is important when considering hardware selection, understanding the limitations of both imaging and positioning systems is essential for developing data acquisition strategies in the field. Together with the general configuration of the survey site and type of aircraft used for the study, the imaging hardware determines image network geometry and ultimately the maximum achievable resolution and scale of the topographic reconstruction. The performance of the GNSS system is in turn responsible for limiting the precision and accuracy of control measurements, directly impacting georeferencing quality. Finally, depending on the camera used, image capture settings are chosen to ensure appropriate exposure given local light conditions, surface properties, and aircraft motion. In this section we describe aspects of field data acquisition for both surveys in this study, including general survey design, control measurements, and image capture settings.

3.4.1 Survey setup

Due to the extensive area and complex topography of the two survey sites in this study, images were acquired in a convergent geometry ($>5^{o}$ off-nadir), along irregular flight paths. This differs from the more common geometry for airborne photo surveys, using nadir imagery captured in a regular grid with a relatively constant aircraft velocity and height above the ground surface, which ensures constant overlap between images and complete coverage of the area of interest. In mostly flat topography, a nadir pointing camera ensures an approximately constant GSD across all images, giving a consistent resolution and expected accuracy of the topographic reconstruction (e.g. Eltner et al., 2016; Smith et al., 2016a). Using convergent imagery in combination with a nadir dataset has been shown to strengthen image geometry and minimise errors due to doming effects common to vertical datasets (James and Robson, 2014; Nesbit and Hugenholtz, 2019). Images captured 30–50º off-nadir are typically defined as oblique. An advantage of oblique cameras is the extended footprint and the ability to cover more ground in a single flightline and to therefore reduce flying distance, time, and cost. Given the large size, complexity, and irregular relief of the two survey areas in this study, flying in a regular grid was impractical, while changing wind patterns resulted in variable flight speed, and large terrain elevation ranges caused the height above the ground surface to vary dramatically (Table 3.2). Using nadir imagery, full coverage of the survey areas would have required a significant increase in flying height and/or decrease in image capture interval. A convergent image geometry was also more suitable to survey the steep slopes and near-vertical rockfaces at both study sites, where oblique viewing angles were ultimately more orthogonal to the ground surface.

For both surveys, a rough plan of the flightpath was discussed with the helicopter pilot prior to takeoff, and the predefined route was followed as closely as possible. At TF we aimed to fly along each side of the three drainage valleys and around the summit plateau, to cover all features from each angle at least once (Fig. 3.2a). The aircraft remained at a near-constant altitude of $\sim$1400 m a.s.l., or between 50 m and 1350 m a.g.l. Images were captured in portrait (vertical) orientation out of the open back door of the helicopter, with the camera operator sitting on the floor and leaning out of the aircraft to avoid catching the skid at the bottom of each shot (Fig. 3.3a). With the camera handheld, image capture was triggered manually at 2–5 s intervals depending on aircraft altitude above ground to maintain $\sim$80% overlap between consecutive photos, for a total of 1204 images (Table 3.2). With the glacier being

	Tanquary Fiord (TF) 2018	Expedition Fiord (EF) 2019
Date	3 August 2018	10 July 2019
Aircraft	Airbus ASTAR 350 B2	Bell 206L Long Ranger
Time (local)	21:30–22:20 (50 minutes)	11:30–11:50 (20 minutes)
Area surveyed	70 km^2	10 km^2
Flight distance	85 km	30 km
Altitude	1200–1400 m a.s.l. (mean 1400 m)	950–1350 m a.s.l. (mean 1250 m)
	50–1350 m a.g.l. (mean 500 m)	75–600 m a.g.l. (mean 350 m)
Velocity	mean 30 m s^{-1} (max 40 m s^{-1})	mean 27 m s^{-1} (max 41 m s^{-1})
Number of images	1204	551
Trigger intervals	Manual trigger, 2–5 s	Intervalometer, 2 s
GPS logging rate	15 s	0.1 s (10 Hz)
Length of lever arm	2.40 $\pm$ 0.43 m	0.36 $\pm$ 0.17 m
Ground targets	2 checkered flags	2 checkered flags, 3 natural features

Table 3.2. Details for the two survey flights in this study. Lever arm refers to the physical offset between the GNSS antenna and camera sensor onboard the aircraft.

the main focus, we aimed to maximise resolution over the glaciated summit plateau by flying close to the surface (short image capture intervals, more data), and opted for a coarser GSD (longer image capture intervals) over the remainder of the drainage basin to avoid running out of space on the memory card.

At EF, flying a regular flightpath was similarly difficult, so we focused on flying around the three glaciers following each of their margins (Fig. 3.2b). Due to their small size, a single pass along each glacier margin was enough to cover the full ice extent. Here, we aimed to maintain a relatively constant height above the ground surface and fly following the topography, but in reality images were captured between 75–600 m a.g.l. It was impractical to make any further plans since, until the morning of the survey, there were still many unknowns regarding the weather and the type of helicopter that would be available for the survey. Ideally, we would have been able to open the back door and shoot more vertically as in the TF survey, but when the helicopter arrived the back door could not be opened, and we had to improvise. Images were therefore captured in portrait (vertical) mode out of the front passenger window on the left side of the aircraft (Fig. 3.3b). Image capture was triggered automatically with a wired intervalometer at regular 2 s intervals, yielding a total of 551 images (Table 3.2).

3.4.2 Control measurements

Camera positions

For both surveys, the GNSS system was initially set to record satellite observations throughout the flights at a 10 Hz logging rate, but due to a system malfunction at the start of the TF survey the receiver reset itself to factory defaults and only recorded observations at 15 s intervals. The GNSS antenna was positioned inside the aircraft. While an external mount would have been preferable for satellite visibility, mounting any equipment on the outside of a chartered aircraft in Canada is not possible without prior regulatory approval. To minimise the negative impact of airframe shadowing on satellite signal reception, the antenna was held on the passenger (left) side of the cockpit, where the larger windows offered better line-of-sight and improved satellite reception compared to the rear of the aircraft. One downside of this setup is the length of the lever arm, or the physical offset between the antenna (the recorded GPS positions) and the camera sensor (the final positions to be estimated). Variations in the orientation of the lever arm caused by aircraft motion and attitude changes have to be compensated for to determine absolute

camera positions and minimise positioning errors. At EF, with both the GNSS antenna and camera positioned on the left side of the cockpit, the measured lever arm was <0.5 m. At TF, with the camera located on the opposite side of the aircraft from the antenna, the estimated offset was 2–3 m. The methods used to account for this lever arm are presented in more detail in section 3.5.2.

Ground targets

To provide independent checkpoints to assess the quality of the direct georeferencing method (using camera positions), we recorded the position of two checkered flags (each 1×1 m in size) placed on the ice or ground surface around both survey sites (Fig. 3.8). The position of each point was measured with a Trimble R7 receiver within a few hours of the air photo survey, with a minimum occupation time of 20 minutes to ensure centimetre positional accuracy. At EF, we additionally measured the position of three distinct large boulders, on three separate occasions between one and two weeks after the survey. Since these targets were only used as validation points for the direct georeferencing method, as opposed to proper control points, only a few were collected.

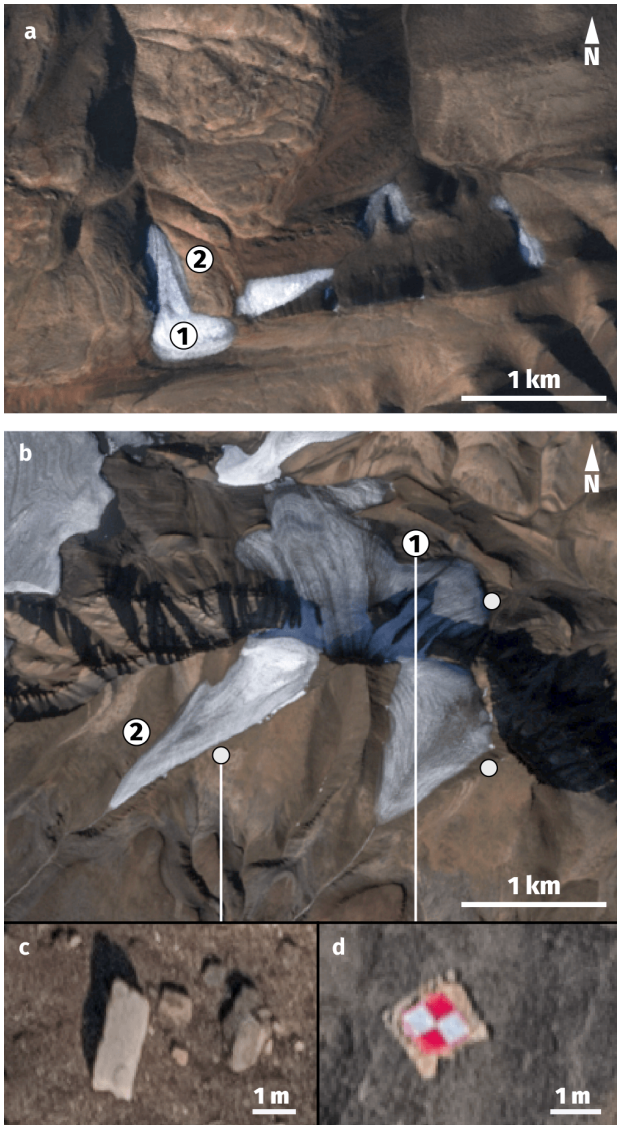

Figure 3.8. Location of ground targets at **[a]** Tanquary Fiord (TF) and **[b]** Expedition Fiord (EF) (Base images: Sentinel 2A, July 2020). **[c-d]** Images of two targets captured from the air during the EF survey (10 July 2019). The targets numbered 1 and 2 in [a] and [b] are 1×1 m checkered flags placed on the ground prior to the air photo surveys [d], while the white circles in [b] are natural features such as distinct boulders [c].

3.4.3 Image capture

Taking into consideration the main elements of an imaging system reviewed in section 3.3.1, camera settings were chosen to optimise sensitivity and resolution and maximise the quality of image data recorded. All images were captured with a Nikon D850 camera and NIKKOR AF-S 24 mm f/1.8G ED lens in Nikon RAW format (NEF), in aperture priority mode, thus letting the camera adjust the shutter speed and ISO according to changing light conditions, ensuring proper exposure in both highlights and shadows.

At TF, aperture was kept constant at f/5.6 to minimise both diffraction effects (worse at apertures of f/8 and beyond; Fig. 3.5a) and lens aberrations (amplified at large apertures; section 3.3.1). Shutter speed was adjusted automatically and limited to a minimum of 1/1000 s to avoid camera shake and motion blur. Where there was insufficient light to maintain proper exposure, the camera automatically increased the gain from the minimum native ISO of 64, up to a maximum of ISO 800 which, for the D850, still produces acceptable levels of noise. A common strategy used to maximise the signal to noise ratio in images is to expose to the right (ETTR), to essentially shift the histogram as far as possible to the right (i.e., maximise brightness) without clipping the highlights. In most cases, this allows optimisation of exposure and preservation of a maximum level of detail in the shadows (Rowlands, 2017). However, during airborne surveys where on-the-fly exposure adjustments are impractical or entirely impossible, the safer approach (used here) is to expose to the left (ETTL) as it is less likely to overexpose highlights and lose crucial information over bright ice and snow-covered areas. The idea is to slightly underexpose the scene and bring out the shadows in post processing, at the expense of introducing more noise to the image (Rowlands, 2017). This can be done by setting the exposure value (EV) compensation to negative values. For example at TF, since the sun was low over the horizon and the light was also getting low, exposure compensation was set to -1 EV which forced the camera to underexpose the scene by a full stop (Fig. 3.9). This also increases the shutter speed and lowers the risk of introducing motion blur, while also decreasing ISO which is beneficial for lower noise and preserving distinct boundaries between features.

For the EF survey, aperture was lowered to f/5.0 to prioritise faster shutter speeds (minimum 1/2000 s) while also lowering the maximum ISO (maximum ISO 400). As there was plenty of light during the midday survey, images were underexposed by 2/3 of a stop (-0.7 EV). The minimum shutter speed was selected so as to ensure aircraft motion did not introduce additional blur, degrading image quality. For example, the ground target in figure 3.8d (target 1 at EF) was captured from a distance of $\sim$260 m. With a GSD of 47 mm px^{-1}, the 1 m^2 target measures $\sim$21$\times$21 pixels on the image. Taking into account diffraction effects at an aperture of f/5.0, the circle of confusion calculated from equation 3.5 is 73 mm, the equivalent of 1.5 times the pixel pitch. The amount of additional blur b (in pixels) due to aircraft motion depends on travel velocity v and shutter speed t:

$$b = \frac{v \times t}{GSD} \tag{3.7}$$

With an average aircraft velocity of 30 m s^{-1} and minimum shutter speed of 1/2000 s, the circle of confusion is only 0.3 pixels (or 15 mm on the ground). In this case, the shutter speed is sufficiently high to avoid motion blur, meaning that diffraction effects (and other lens aberrations) would be primarily responsible for reducing the system resolving power. A certain amount of blur is expected and should be taken into consideration when devising the

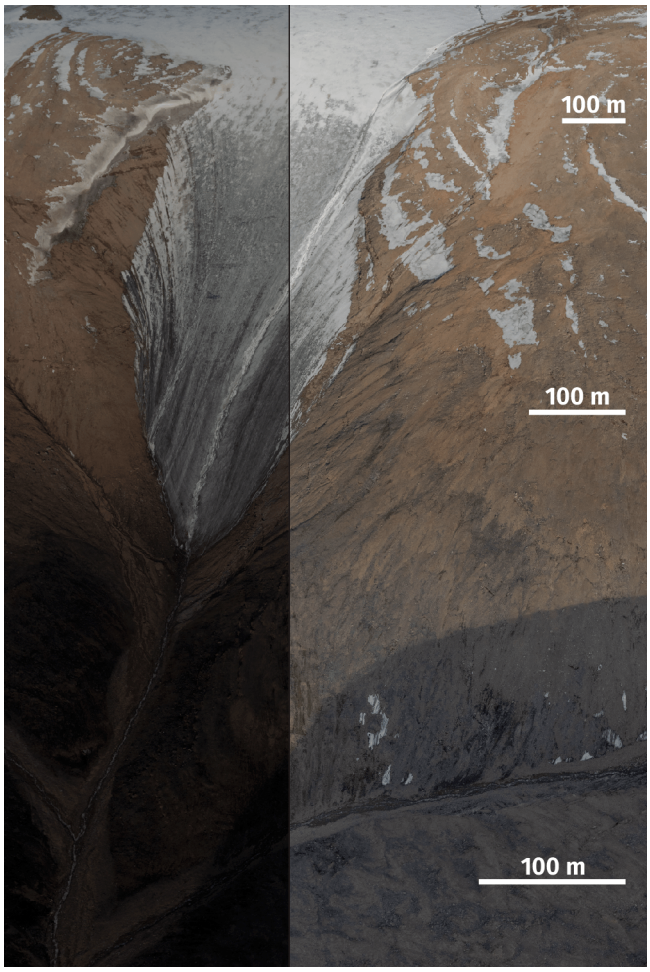

Figure 3.9. Strong shadows on an image of Bowman Glacier (TF) acquired on 3 August 2018.
[Left] Unedited RAW image and **[Right]** edited copy with exposure adjustments to bring out information from the underexposed part of the image. As the distance between the camera sensor and ground surface increases towards the top of the frame, image scale in the foreground is about twice the scale in the background.

flight plan. Considering the highly variable flying height above ground for surveys over rugged terrain, and the resulting differences in GSD, the minimum shutter speed (and target aircraft speed) should be selected in order to keep the circle of confusion due to motion blur at or below the size of the circle resulting from diffraction.

Lastly, achieving and maintaining proper focus is crucial. Here, the focus was set to infinity (by focusing on a distant feature) and switched to manual as conditions during a typical air photo survey make it difficult to ensure the proper functioning of the auto focus, which tends to pulsate in and out of focus between exposures. Unfortunately, about 10% of the TF images ended up slightly out of focus (and were discarded) due to the camera operator accidentally nicking the focus ring 20 minutes into the survey; taping the focus ring is a common strategy (and generally a good idea) often used to avoid this issue.

3.5 RAW DATA PROCESSING

Following the air photo surveys, the raw image data captured by the camera sensor were first processed to maximise the amount of visual information in order to help with feature extraction. Camera positions associated with each captured image were calculated from PPP processed GNSS measurements following a series of steps summarised further below and detailed in the Appendix.

3.5.1 Image postproduction

Initial corrections were performed on the 14-bit RAW images in Adobe Lightroom (Process Version 5) using the lens profile listed in the EXIF metadata to correct for vignetting and remove chromatic aberrations, while leaving any geometric distortions untouched. Chromatic aberration is caused by light refraction which causes colour fringing, or purple artefacts along high-contrast boundaries (Fig. 3.10). Vignetting consists of illumination falloff, a drop in light intensity towards the edges where light reaches the sensor at an angle (Ray, 2002). Since photogrammetry algorithms rely on distinct edges between features and consistent lighting conditions, compensating for both these aberrations should theoretically enhance feature detection. The digitisation process which converts sensor information into raw image data introduces some softness, which was compensated for by applying the default sharpening presets in Lightroom. Although additional sharpening can improve perceived sharpness, especially where image quality is lacking, excessive sharpening can also impact the structure of the file and introduce visible artefacts, such as halos at object edges (Rowlands, 2017). Additional digital noise reduction was performed to minimise chromatic noise (colour variations between pixels in areas of uniform colour, mostly apparent in dark shadows), which becomes more problematic with increasing ISO values. Lastly, a variable exposure gain was applied to all images to brighten underexposed areas and match total exposure of successive images. This was performed to increase the level of detail and available information for feature extraction, as well as to even out differences in illumination between images to enable a more uniform orthophoto reconstruction. Images were ultimately exported as uncompressed TIFFs with 16-bit depth in the ProPhoto RGB colour space, yielding files of >270 MB each (total dataset size of nearly 500 GB for the 1639 images from both surveys, excluding the discarded out of focus ones).

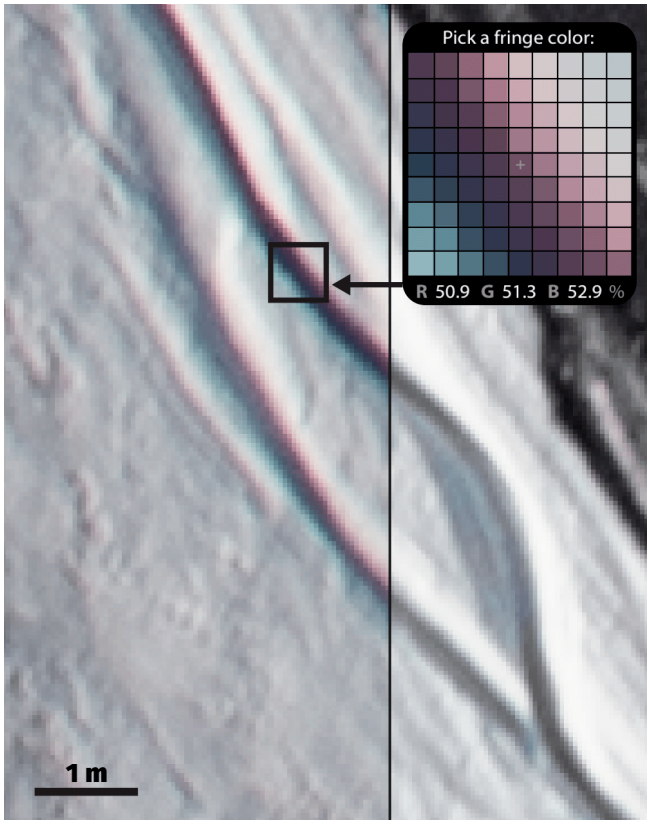

Figure 3.10. **[Left]** Uncorrected image from the Expedition Fiord (EF) survey (10 July 2019) showing chromatic aberrations with purple fringe along meltwater stream. **[Right]** Corrected image with aberrations removed.

Both surveys were flown with a convergent geometry and therefore included very few nadir images, with most being taken at a low or high oblique angle. For high oblique photos, where the horizon is included in the frame, the most time-intensive task in post-production is masking extensive swaths of sky and any terrain beyond the area of interest. A few images also included some part of the helicopter skid. In this study, all masks were generated using the Adobe Photoshop iPad app and the 'Quick selection' tool, which automatically identifies and snaps to distinct edges in an image. The resulting masks were exported as PNG files, for a total of 495 and 180 masks for EF and TF, respectively. For EF with a high proportion of high oblique images, 90% of all images required masking, compared to 17% for TF where images were captured at a low oblique angle.

3.5.2 GNSS data postprocessing

The raw (GPS) satellite observables collected by the dual-frequency (L1 and L2) Trimble R7 receiver were converted into RINEX format with the Trimble Convert to RINEX Utility and then processed in kinematic mode (i.e., with a unique position for each epoch) using the Geodetic Survey Division of Natural Resources Canada Canadian Spatial Reference System PPP (NRCan CSRS-PPP) online service (software version 3.45.0, updated 27.10.2020, https://webapp.geod.nrcan.gc.ca/geod/tools-outils/ppp.php). The steps for retrieving camera positions at the time of image capture from this data were implemented in a custom R (version 4.0.5) script and are summarised below. The uncertainty of camera positions was determined with a series of estimations to take into account various error sources, including GNSS positioning and PPP modelling errors, imprecise lever arm measurements, unmodelled aircraft attitude changes, and delays in synchronisation between the positioning and imaging systems.

PPP processing

The CSRS-PPP positioning tool takes into account observations from all satellites in view above an elevation mask angle of 7.5º and requires a minimum of five satellites for a valid position fix. The solution is derived from undifferenced code and carrier phase observations from a single GNSS receiver and relies on precise satellite orbits and clock products from the International GNSS service (IGS). It uses a sequential Kalman filter to estimate four unknown parameters: receiver position, receiver clock offset, tropospheric zenith delay, and carrier phase ambiguities. In kinematic mode, the algorithm solves for independent solutions at each observation epoch and uses backward smoothing to produce a corrected track (Kouba and Héroux, 2001). The CSRS-PPP outputs coordinates projected in the NAD83(CSRS) horizontal datum. Vertical reference includes both ellipsoidal heights based on the Geodetic Reference System 1980 (GRS80) reference ellipsoid, and orthometric heights (elevation above the geoid) projected in the Canadian Geodetic Vertical Datum 2013 (CGVD2013), based on the Canadian Gravimetric Geoid 2013 (CGG2013a) model. For compatibility and to simplify comparison with other elevation products including the ArcticDEM, we opted to work with ellipsoidal heights referenced to the WGS84 ellipsoid.

Code and carrier phase measurement residuals are calculated for each signal and satellites with large residuals, above a certain threshold, are excluded from the results. These residuals represent the difference between the measured and predicted pseudoranges and contain the receiver position error along with any modelling and measurement noise errors. The PPP output includes the position solution, as well as the predicted level of uncertainty given by the Kalman filter covariance matrix for the parameters modelled at each observation epoch, including estimated

receiver coordinates in the East, North, and Up (ENU) directions (Fig. 3.11). Position uncertainty estimates are given as 2-sigma error bounds (95% confidence level). In terms of linear error (i.e. altitude), the stated uncertainty values correspond to a 95.45% probability that the true position is within ±2–sigma bounds of the central value in any direction. We represent the two-dimensional horizontal uncertainty using the 2 drms metric, corresponding to twice the RMS radial error (1 drms), equal to the root of the sum of squares of the error components in the north and east directions ($2drms = 2\sqrt{\sigma_e^2 + \sigma_n^2}$). The confidence level associated with the 2 drms error is dependent on the eccentricity of the error ellipse (i.e., the ratio of the minor to the major semi-axes), and varies between 98.2% for a circular normal distribution (where $\sigma_e = \sigma_n$) and 95.4% in more common elliptical cases (National Geospatial Intelligence Agency, 2019).

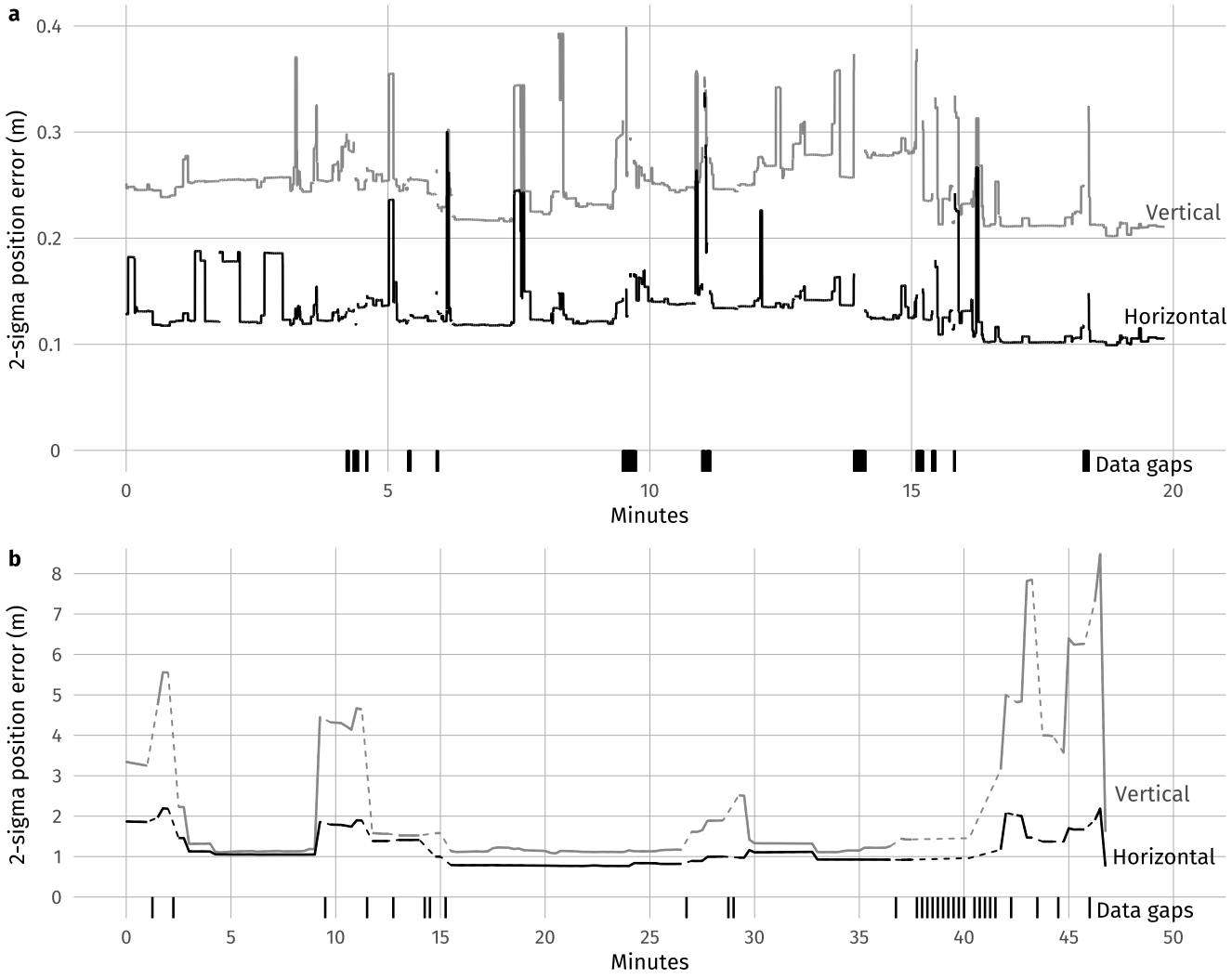

Figure 3.11. Standard deviations (2–sigma 95%) of East, North, and Up components of estimated GPS positions for **[a]** Expedition Fiord (EF), and **[b]** Tanquary Fiord (TF).

Camera positions

Synchronisation between the camera shutter and positioning system was achieved via the Trimble Event Input Marker connecting the GPS receiver to the camera hot shoe accessory mount (Fig. 3.3d). With each shutter action, the camera generates a TTL (Transistor-Transistor-Logic) level voltage signal which is generally used to activate an electronic flash unit. Here, the rising edge of the TTL pulse output by the camera was recorded by the GPS receiver as an external event, which is listed as an event flag record alongside the satellite observation records in the RINEX observation file. The PPP software estimates coordinates for epochs with valid satellite observation records but skips over all event flag records. Therefore, the position of the antenna at the precise moment of image capture has to be subsequently interpolated from the estimated GPS positions immediately before and after each external event record. Corresponding camera positions are then calculated, compensating for the physical offset (lever arm) between the GPS antenna and camera sensor. The steps used for assigning coordinates at each event flag and calculating camera positions at the time of exposure are described in detail in the Appendix.

Lever arm

The lever arm between the GPS antenna phase centre and the camera sensor was measured along three orthogonal axes fixed in the aircraft reference frame. The offsets were difficult to measure precisely, and uncertainties were estimated to be $\pm$10 cm at EF, and $\pm$25 cm at TF. With no additional sensors to keep track of aircraft attitude changes, we assumed straight and level flight conditions, with constant linear and angular velocity between estimated GPS positions. That is to say, no change in the velocity components in respect to the x, y, z axes (forward, side drift, and vertical velocity) and their corresponding rates of rotation about the same axes (roll, pitch, and yaw rate). In reality, however, aircraft motion varies in response to perturbations in wind conditions and flight dynamics, which introduces attitude errors and influences camera positions and their accuracy estimates. Here, we consider aircraft heading (i.e., the direction in which the longitudinal axis is pointed) to be parallel to the flightpath, and attitude errors about the yaw (z) axis are considered to fall within $\pm$15º of the ground track. Pitch and roll angles are assumed to be zero (horizontal) with maximal errors of $\pm$15º around the transverse (y) axis, and $\pm$30º around the longitudinal (x) axis (Fig. 3.12). These values represent upper bound error estimates and are generally regarded as the maximum yaw, pitch, and roll angles reached during normal flight conditions (Personal communication, Grech, 2019).

Synchronisation error

The synchronisation between the positioning system and camera shutter depends on the sum of delays due to the GNSS receiver clock, length of cable runs, and camera operations. As discussed in section 3.3.1, focal plane shutters (such as the one on the D850) use mechanical vertical travel shutters which expose the sensor array sequentially over a timespan corresponding to the flash synchronisation (X-sync) speed (1/250 s for the D850) after which the shutter is fully open, and the TTL signal is generated. Considering that the maximum spropagation delay and rise and fall time for a standard TTL signal are $\sim$10 ns and 50 ns, respectively (Mano and Ciletti, 2013), and that the accuracy of the timestamp logged by the GPS receiver is typically $<$1 µs (Trimble, 2009), in theory the synchronisation between camera shutter and the GPS is 0.00106 ms. However, when capturing images from a moving platform, taking into account the vertical curtain travel time and the resulting motion trace significantly

increases synchronisation uncertainty (by 3 orders of magnitude). With an average travel speed of ∼30 m s^{-1} (∼60 knots), combining the X-sync speed (1/250 s) with the slowest shutter speed used (EF 1/2000 s; TF 1/1000 s) means that, on average, the camera travelled ∼12–14 cm during a single exposure (Fig. 3.12). The computed horizontal and vertical components of the motion trace calculated for each image are therefore taken into account in the final camera position uncertainties. Camera positions interpolated over data gaps with no GNSS solution were marked as invalid and therefore not used in the following SfM processing steps.

3.6 DEM & ORTHOPHOTO GENERATION

Following post-processing of raw field data, optimised image files and corresponding camera position estimates were used to derive georeferenced DEMs and RGB orthomosaics of the study areas. The full SfM-MVS workflow described below was performed in Agisoft Metashape Pro (version 1.6), starting with feature detection (section 3.6.1) and SfM processing resulting in a sparse point cloud (section 3.6.2), followed by MVS matching and dense cloud generation (section 3.6.3). Additional point cloud filtering and the final error assessment (section 3.6.4) were undertaken in CloudCompare (version 2.11.1, cloudcompare.org).

3.6.1 Feature detection

After importing all images and corresponding masks, Metashape estimates image quality based on the sharpest area of each image relative to the full dataset. It is generally recommended to remove images with a quality below 0.5 (Agisoft, 2020). With the exception of 116 out of focus images from TF, the lowest values for all photos from both surveys were above this threshold. In Metashape the first step of the workflow, image alignment, incorporates both feature detection and SfM processing steps. The latter involves defining the geometric relationship between a given point in a 3D space and its corresponding 2D projection onto the image plane. This requires the detection of sets of pixels in individual images (keypoints), before matching them across multiple photos (tiepoints). In Metashape feature matching is based on the scale-invariant feature transformation (SIFT) algorithm (Lowe, 1999).

Keypoint detection was performed using the 'highest' accuracy setting, where images are first upsampled by a factor of four. Increasing image resolution involves interpolating pixel values which can introduce artefacts (Szeliski, 2011). It is therefore only advantageous for high resolution and high quality images where it can be helpful with identifying more features and locating corresponding tiepoints with sub-pixel precision. Tested on a subset of 20 images from the EF dataset, the average number of keypoints detected on upsampled images was 7–8 times greater than with the original resolution data (1.6 vs 0.2 million points per image), and the average number of valid tiepoints increased by a factor of four (310,000 vs 75,000 points per image). The total point count in the corresponding sparse clouds was five times greater based on the upsampled data (2.3 vs 0.46 million points each).

Here, matching was performed using the 'generic preselection' option, where the software first selects image pairs by identifying matching features at a coarser scale before refining their location at full resolution. The keypoint detection limit was set to 200,000, ignoring the masked portions of each image, and the tiepoint limit set to 20,000 points per image. Setting a limit on the maximum number of points significantly speeds up processing and helps filter out lower quality keypoints and less reliable matches.

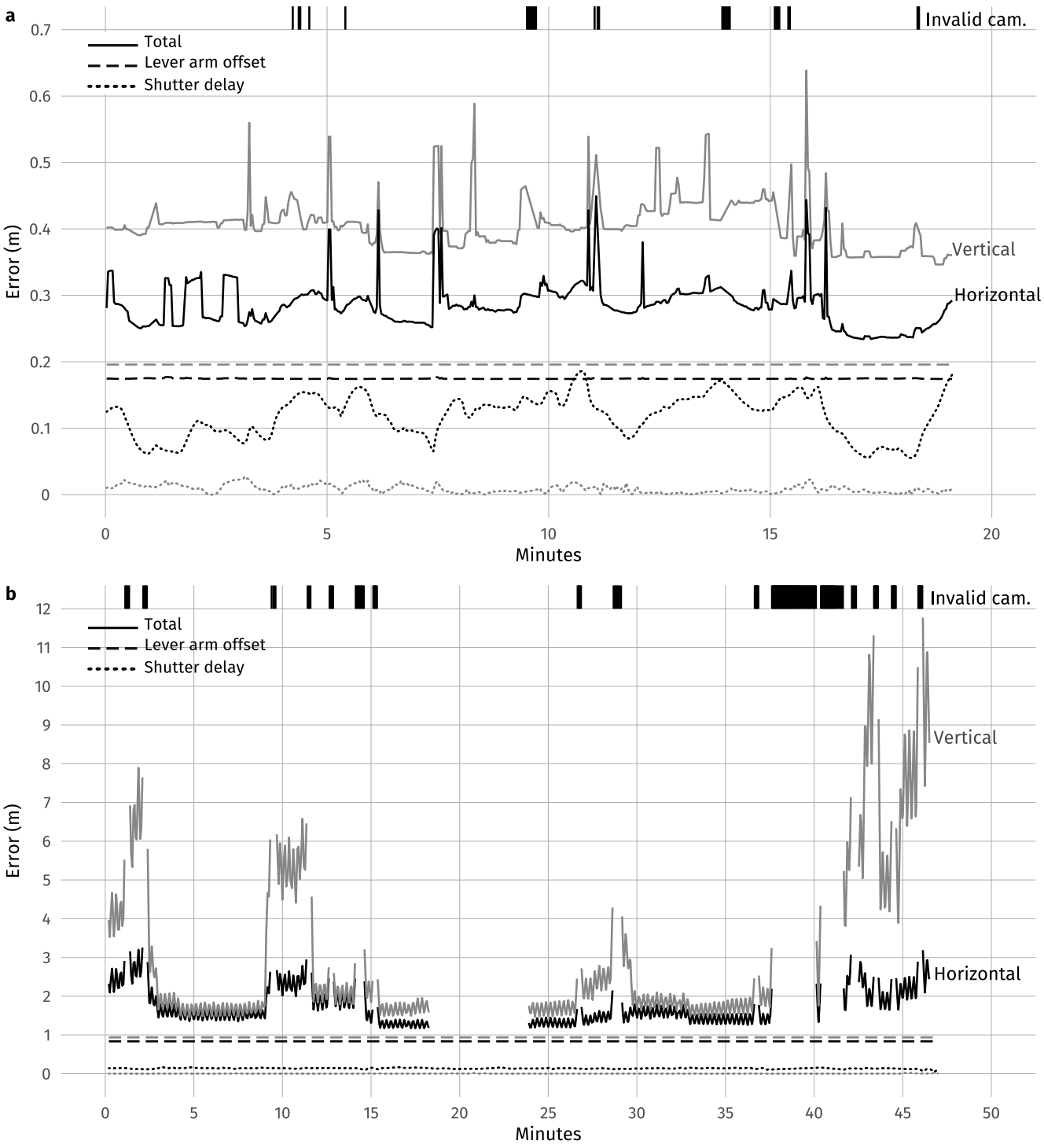

Figure 3.12. Contribution of different error sources to camera position uncertainty estimates for **[a]** Expedition Fiord (EF), and **[b]** Tanquary Fiord (TF). Horizontal (black) and vertical (grey) camera position accuracy estimates (solid lines) are based on 2-sigma PPP positioning uncertainties (Fig. 3.11) and combine: (1) errors associated with the lever arm, including imprecise offset measurements and expected aircraft attitude changes propagated down the length of the lever arm (dashed lines), and (2) synchronisation errors from camera displacement during shutter motion (dotted lines). See Appendix for further details.

3.6.2 Structure from motion

SfM processing uses the correspondence between camera centres and matched features to perform a bundle adjustment in which scene geometry, and both extrinsic (external position and orientation) and intrinsic (internal geometry) camera parameters are estimated simultaneously (Szeliski, 2011). The latter are described by the camera calibration model formulated by Brown (1971) and include principal distance (c), principal point offset (cx, cy), and the parameters accounting for lens distortions, usually three radial symmetric (k1-k3) and two decentring terms (p1-p2). Additional affinity and orthogonality (b1-b2) terms describing pixel aspect ratio and axial skew can be included to compensate for focal plane distortions. In theory, intrinsic parameters are camera-specific, and should therefore remain fixed for a given survey. However, mechanical instabilities including inadvertent changes in focus distance, cause variations in the internal geometry of the lens and therefore in the principal distance, principal point position, and in the radial and decentring lens distortion coefficients (Brown, 1971; Fraser, 1997; Sanz-Ablanedo et al., 2012). The last two parameters, affinity and orthogonality, remain constant with variations in focusing distance. Principal distance and radial distortion parameters can also vary between each of the RGB colour channels in a single image as a result of chromatic aberrations within the lens, which causes different wavelengths to shift and focus at different points on the focal plane (Fraser, 2013). In particular for imaging systems using zoom lenses with variable focal length, or when focusing distance is known to have changed during the survey, it can be helpful to allow some parameters to vary during the calibration, either for different camera groups or each individual image (Fraser, 1997).

In this study, given that the camera was refocused midway through the TF survey, we treat the images captured before and after the set of blurry ones as two distinct camera groups and allow the software to adjust the calibration coefficients (c, cx, cy, k1-k3, p1-p2) separately. For the EF survey, the coefficients are kept constant for all cameras. Following the initial alignment, a first quality check was performed to identify images with low number of projections ($<$1000 tiepoints) and high tiepoint pixel residuals ($>$1 pixel): only two images from the EF survey were removed due to a low projection count, and none from the TF survey. After deleting points far outside the area of interest, the resulting sparse point clouds counted over 2.5 and 6 million points for EF and TF, respectively (Table 3.3).

The camera reference information assigned to each image, including ENU coordinates and horizontal and vertical uncertainty estimates, was loaded from a separate file. The input camera coordinates were first used to georeference the point clouds through a series of linear transformations (translation, rotation, scaling). The reconstructions were then optimised to compensate for non-linear deformations, adjusting camera parameters and estimated tiepoint positions based on the camera reference information (weighed according to provided accuracy values). Cameras with invalid position estimates (section 3.5.2) were marked as ‘disabled’, that is, the estimated positions were excluded from the optimisation procedure and had no influence on the position of the tiepoints calculated from the corresponding image data.

For higher performance cameras it is generally reasonable to assume the sensor to be flat and mounted perpendicular to the optical axis, and so to assume square pixels and zero-skew and therefore omit both affinity and orthogonality parameters (b1-b2) from the camera model (Fraser, 1997; Sanz-Ablanedo et al., 2012). However, rolling shutter effects combined with camera motion can have an impact on image geometry, causing shear and/or extension or

compression of individual pixels. For the Nikon D850 used in this study, and a flying speed of 30 m s^{-1} at a height of 500 m a.g.l., object displacement due to rolling shutter effects averaged 1.3 pixels (section 3.3.1). This value increases with aircraft velocity but primarily depends on height above ground, and in our case generally varies between 0.96 pixels (>700 m a.g.l.) and 4.47 pixels (<150 m a.g.l.). For this reason, we optimised the alignment taking into account the additional affinity parameter (b1), aiming to minimise the sum of point reprojection errors, and both external camera position and internal calibration coefficient errors.

In each cloud, 10% of tiepoints with the highest reprojection error values (maximum 0.41 pix for EF, and 0.43 pix for TF) were removed, as well as those with high positioning uncertainty (variance >10 m), and a second optimisation was performed. The resulting sparse clouds were cropped to the region of interest prior to proceeding to dense-stereo reconstruction. All points including reprojection errors and point positioning variance were exported in ASCII file format using a custom Python script. Average tiepoint variance values in the final sparse clouds are 0.44 m for the EF survey (Fig. 3.13a) and 0.45 m for the TF survey (Fig. 3.13b), while RMS point reprojection errors are 0.53 pixels and 0.41 pixels at EF and TF (Table 3.3).

Table 3.3. Point cloud information from SfM-MVS processing performed in Metashape for the two reconstructions in this study.

	Tanquary Fiord (TF) 2018	Expedition Fiord (EF) 2019
Number of aligned images	1088	549
Keypoint limit	200,000	200,000
Tiepoint limit	20,000	20,000
Tiepoint count: total / valid	6,221,414 / 6,675,339 (93%)	2,430,740 / 2,643,663 (92%)
Tiepoint count: final	5,402,000 (87%)	2,144,040 (88%)
RMS point reprojection errors	0.41 px	0.53 px
Normalised to keypoint size	0.18	0.18
RMS camera position errors		
horizontal / vertical / total	10.55 / 2.17 / 10.77 m	0.72 / 0.58 / 0.93 m
RMS checkpoint errors		
horizontal / vertical / total	0.35 / 0.68 / 0.77 m (0.41 px)	0.46 / 0.29 / 0.56 m (0.36 px)
Average point variance	0.45 ± 0.9 m	0.44 ± 0.9 m
Average GSD	13.1 cm px^{-1}	9.87 cm px^{-1}
Dense point cloud count	1,464,754,261	406,339,550
Average surface density	13.77 ± 3.17 pt m^{-2}	24.24 ± 5.69 pt m^{-2}

3.6.3 Multiview stereo matching

In the majority of studies using SfM, including this one, MVS algorithms are used to increase point density in the sparse point cloud for high resolution reconstructions. The MVS algorithm implemented in Metashape uses depth determination as an intermediate step to provide source data for the generation of the final dense point cloud. Depth maps (also called disparity maps) are generated from the disparity of matched features in a stereo pair, using the shift of a given pixel in overlapping images in combination a known camera calibration to extract depth information (Szeliski, 2011). In this study, disparity estimation was performed for all image pairs with a minimum of 100 matching points, with a separate depth map being generated for each individual input image based on information from multiple overlapping images. Further processing of disparity maps can be performed to remove outliers and spurious points introduced by inadequate image overlap or coverage, and by noisy or out of focus, low quality images. Metashape uses a built-in algorithm to filter outliers and geometrical errors, with three presets specifying the level of noise filtering in the raw depth maps (mild, moderate, aggressive), and the option to disable filtering

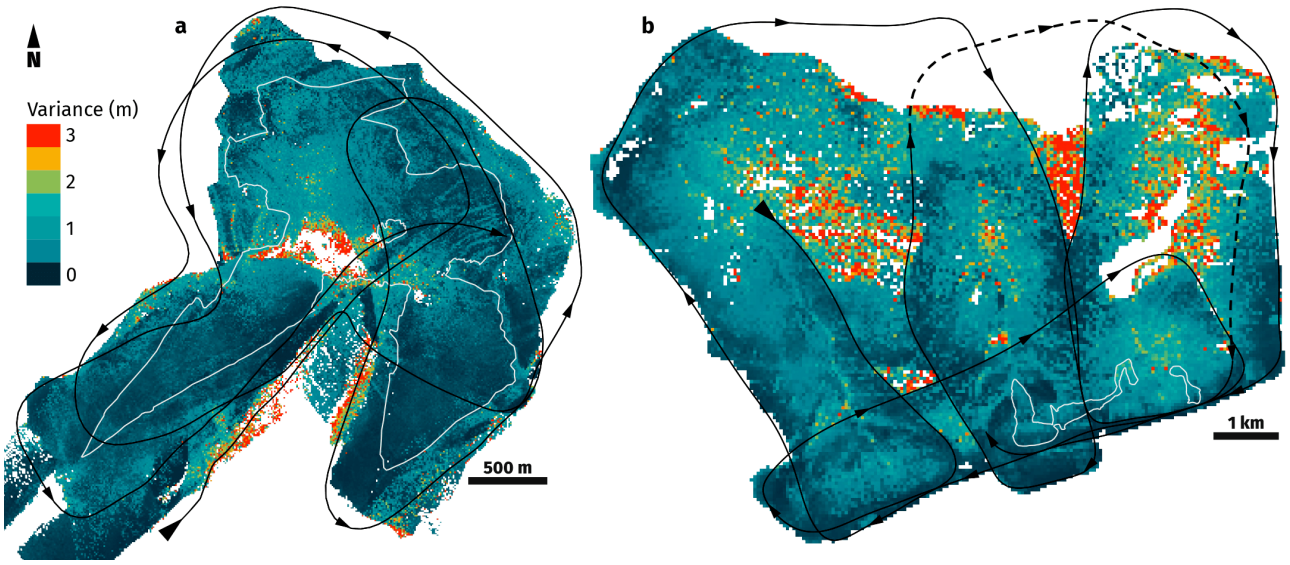

Figure 3.13. Sparse point clouds showing tiepoint variance for the **[a]** Expedition (EF) and **[b]** Tanquary Fiord (TF) surveys, including glacier outlines (white line) and flightpath with direction of aircraft travel (black line). The dashed line segment in [b] represents a 10 km segment where 116 out of focus images were removed from the dataset. Same spatial coverage as in Figs 3.14 and 3.15.

altogether. The smoothing step is based on the connected components filter, which extracts clusters of contiguous pixels (i.e. connected components) based on a set of similarity measures (e.g. intensity values) (Szeliski, 2011). There is no way for the user to adjust the connectivity parameter directly and therefore no control on the size of the components (size of neighbourhood) discarded by the filter. An issue arises where the smoothing algorithm is unable to clearly distinguish between surface roughness and noise, and where filtering unwanted noise also smooths out small details. Here, depth maps were left unfiltered and merged into a single surface reconstruction. The resulting dense point clouds were exported in LAS file format for further processing in CloudCompare in order to retain more control on the filtering process.

3.6.4 Dense reconstruction post-processing

While generating the dense point cloud, Metashape calculates a 'point confidence' parameter which refers to the number of depth maps used to generate any given point in the dense cloud. Here, we use confidence values to initially filter out points resulting from a single depth map (confidence = 1), leaving points with confidence values reaching a maximum of 115 and 85 for EF and TF, respectively. The dense point clouds were subsequently filtered using the Multiscale Model to Model Cloud Comparison (M3C2; Lague et al., 2013) plugin implemented in CloudCompare. Developed for direct cloud comparison and change detection, the M3C2 algorithm can also be used to filter a noisy point cloud surface by computing local statistics for averaging or filtering outliers. The method operates by calculating the mean or median height values of all points within a cylindrical neighbourhood of a given diameter and depth, oriented along a projected vector perpendicular to the surface (i.e. surface normal).

In this study we apply the automatic method for surface normal computation, where the optimal scale is determined based on surface roughness. While smaller scales are able to more accurately represent small surface features, in order to avoid surface normals being affected by local surface roughness, including potential geometric errors and

outliers, Lague et al. (2013) suggest the scale for normal computation to be 20–25 times the roughness calculated at the corresponding scale. Surface roughness was determined with the roughness computation tool in CloudCompare, using various scales, between 2–10 m in diameter, increasing in 1 m steps. All tested scales were at least 20 times the mean roughness of both clouds. For each point, the optimal scale for computing surface normals was automatically selected by the M3C2 algorithm. The projection scale, or the search radius used to calculate local statistics, was chosen based on point density to ensure a minimum of five points within each neighbourhood. Given a mean point spacing of 0.35 m and 0.45 m for the EF and TF point clouds respectively, median point elevations and interquartile range (IQR) were calculated within a neighbourhood of 1 m diameter and 5 m depth above and below each point in the cloud. Finally, the smoothed point clouds were gridded and exported into DEMs and RGB orthomosaic rasters at 0.5 m horizontal resolution, with each pixel representing the mean of all elevation or RGB values of all points within a given grid cell (Fig. 3.14).

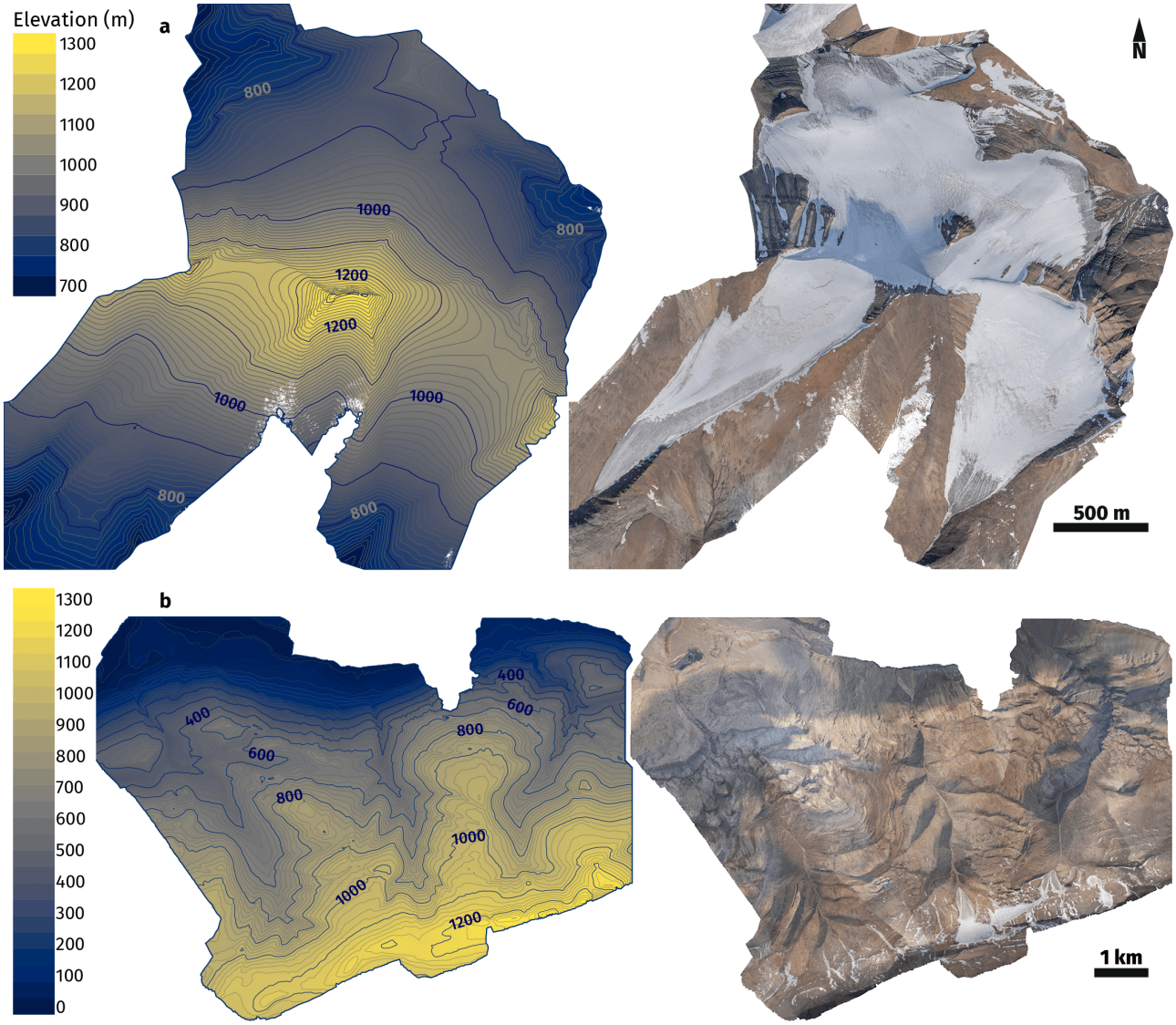

Figure 3.14. SfM-MVS outputs with elevation model (left) and RGB orthomosaic (right) of the **[a]** Expedition (EF) and **[b]** Tanquary Fiord (TF) survey areas. Elevation contour lines at 10 m spacing in [a] and 20 m in [b]. Same spatial coverage as in Figs 3.13 and 3.15.

3.6.5 Outputs

In both surveys in this study, flightlines were deliberately planned to prioritise image acquisition over ice masses and areas of lesser interest received lower coverage or were only imaged from afar. As a result, the quality of the reconstructions varies spatially and is most consistent over glaciers and adjacent areas. Where coverage is adequate and the surface uniform and fairly flat, point spacing in the final reconstruction is regular and surface density more or less constant, with an average of 13.75 ± 1 pt m^{-2} and 21.5 ± 0.8 pt m^{-2} at TF and EF, respectively (Fig. 3.15). Overall, the main difference between the two surveys is likely related to aircraft altitude above ground, which was on average higher at TF (500 m) than at EF (350 m). For a given imaging system (with a given resolving power and focal length), the distance from camera sensor to ground surface is directly related to the size of pixels on the ground (the GSD). Objects imaged at close range cover more pixels on the sensor and are relatively larger and so more detailed in image space. Higher information content in image data enhances feature detection (both quantity and quality) which in turn determines the maximum achievable point density. Low altitude surveys therefore allow for higher resolution surface reconstructions but are impractical over large study sites and those with highly variable surface topography. Steep terrain inevitably forces an aircraft to increase flying height in order to steer clear of peaks and ridges, meaning that low lying points are mostly imaged from further away. At the same time, image footprint increases with distance to object, which provides wider spatial coverage in a single pass, reducing both flying distance and survey duration.

In addition, there is considerable spatial variability in point density within each survey. At TF the reconstruction tends to be patchier between each of the three drainage valleys (Fig. 3.15b). Due to oblique image capture, the camera was able to image a single side at a time and any terrain on the opposite side, or immediately below, the aircraft was either omitted entirely or only appeared in the background of a few images. At EF, steep slopes (>30º) tend to have higher surface point density, averaging 31.5 ± 1.4 pt m^{-2} (Fig. 3.15a). Unlike the more spread out TF survey site, the EF survey was focused around a central massif which, combined with lower aircraft flying height, favoured more oblique image capture. As a result, steep vertical terrain was imaged at a more perpendicular angle, which helped minimise perspective distortions between overlapping images and allowed for more reliable extraction and consistent identification of distinct surface features in stereo matching. The widely used SIFT algorithm, which is implemented in Metashape, is efficient at matching features despite variations in scale and orientation, but is only partially invariant to illumination and affine distortions (Lowe, 2004). In general, extreme affine distortions from widely different viewpoints such as those common in low-oblique aerial imagery pose a significant challenge to robust feature matching. In addition, oblique viewing angles are more likely to cause occlusions, where distant objects are obscured by those in the foreground, further reducing matching performance (Lowe, 2004). Lower point density is also characteristic of deeply incised V-shaped valleys, as the valley bottom is often in shadows and easily obscured from view by steep slopes rising on each side.

Where point density is insufficient, setting a higher keypoint limit could enhance feature detection and help fill some gaps to enable a denser reconstruction in background areas. However, allowing the software to detect more features may increase the likelihood of false or less reliable matches, ultimately producing more poorly localised tiepoints in the cloud. While this would help increase coverage in low point density areas, it is also likely to add significant surface noise over the rest of the cloud. Including lower quality keypoints, from blurry images or based on objects

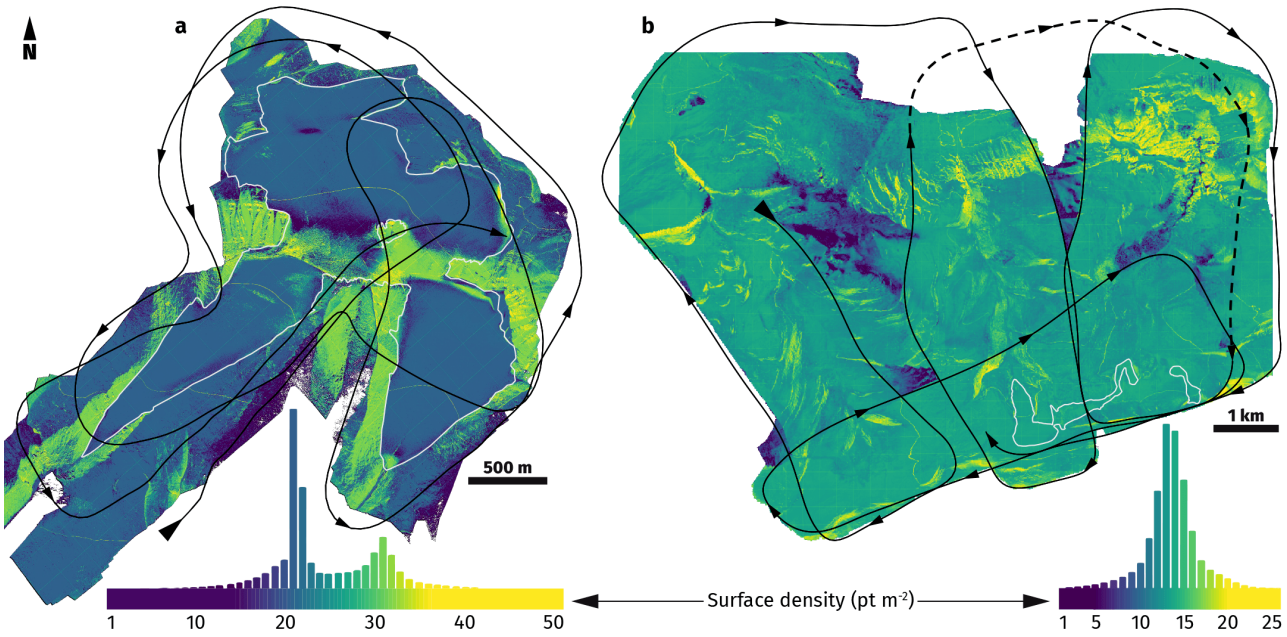

Figure 3.15. Surface point density for the **[a]** Expedition (EF) and **[b]** Tanquary Fiord (TF) dense point clouds. White outline indicates glacier ice. Solid black line shows the flightpath and direction of aircraft travel. The dashed line segment in [b] represents a 10 km segment where 116 out of focus images were removed from the dataset. Same spatial coverage as in Figs 3.13 and 3.14.

imaged from a great distance, for example, can produce outliers, including isolated points as well as overlapping false surfaces above the main point cloud surface (Fig. 3.16). Using the M3C2 tool to filter a noisy cloud surface is fairly effective at removing isolated outliers as those have little effect on the median elevation and IQR values computed within a cylindrical neighbourhood around a given point (here, the neighbourhood dimensions were 0.5 m diameter and 2 m depth). However, dealing with overlapping surfaces remains problematic. If contained within the neighbourhood, the cluster of unwanted points will increase local IQR and shift the median elevation of the main cloud surface upwards. Otherwise, if the overlapping surface is outside the specified neighbourhood depth, the M3C2 tool will compute separate median point elevations around the 'true' and false surfaces, the average of which will be gridded into the final DEM product. It is therefore preferable to remove low quality images from the dataset and mask any terrain appearing in the background, where image quality tends to degrade, in order to avoid poor quality keypoints which prevent the proper geometric representation of surface texture.

From this study it is clear that irregular survey geometry coupled with oblique image capture can give uneven coverage, with overlapping surfaces and gaps occurring in areas with false, or insufficient numbers, of correctly matched features. In general, the uncertainty of estimated tiepoint coordinates increases where point density decreases (Fig. 3.13 and Fig. 3.15). This is not necessarily representative of real accuracy as tiepoint variance, calculated from the covariance matrix obtained at the end of the bundle adjustment, is more a measure of internal consistency of the reconstruction than georeferencing quality. Likewise, point elevation IQR calculated using the M3C2 algorithm is an appropriate measure of the level of surface noise, but not a direct indication of registration errors. Still, separating random noise from the actual signal and determining the minimal level of detection is crucial in applications involving topographic change detection so as not to overestimate change.

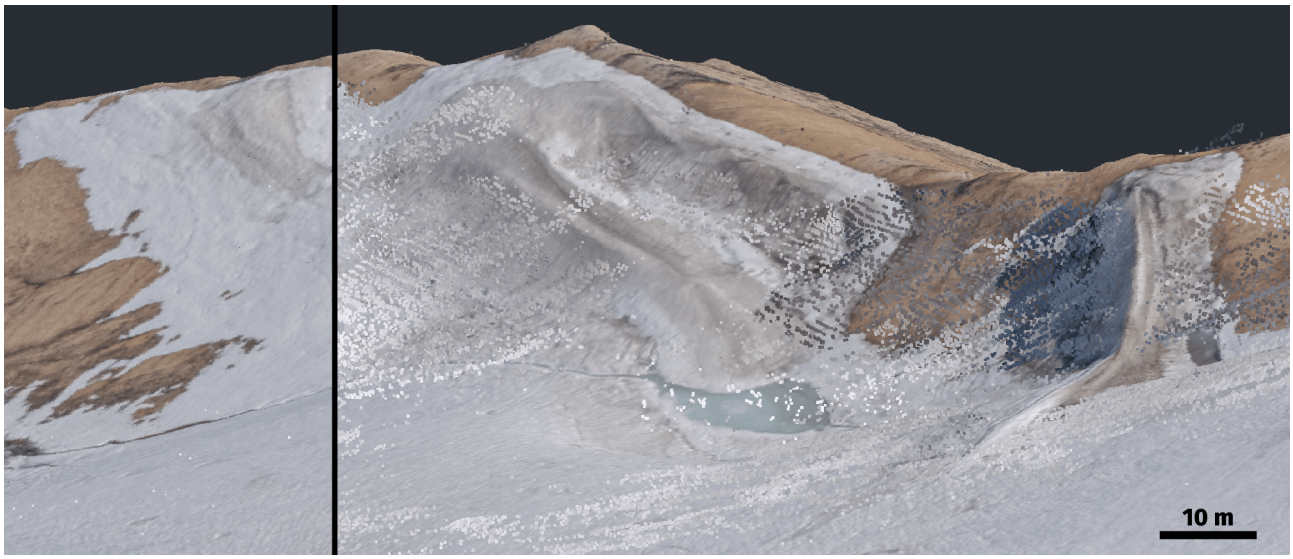

Figure 3.16. Subset of the dense point cloud near the saddle of Baby Glacier, Expedition Fiord (EF). **[Left]** Filtered dense point cloud representing the "true" surface and **[Right]** Unfiltered noisy point cloud with isolated floating points and overlapping surface features resulting from lower quality keypoints based on distant objects imaged in the background of a few images.

In this study, the only source of independent validation are the checkpoints measured in the field. Georeferencing accuracy varies spatially across the reconstruction, and so checkpoints are only representative of local registration errors. Still, the magnitude of these values is a useful indicator of the maximum expected accuracy when characterising surface topography. Here, RMS errors for the two checkpoints at the TF survey site are 0.35 m horizontal and 0.68 m vertical (0.77 m total), and for the five checkpoints at EF, 0.46 m horizontal and 0.29 m vertical (0.56 m total) (Table 3.3). Ideally, horizontal accuracy should be higher or equivalent to the spatial resolution of the final gridded products. Here, both DEMs and orthomosaics were gridded at 0.5 m resolution and horizontal checkpoint misalignment errors remain below that level for both reconstructions. Vertical accuracy requirements are project specific and depend on the level of detail necessary for a given study, but are sufficient for detecting long-term changes in the geodetic mass balance of glaciers in this study given surface thinning that can exceed >1 m yr^{-1} at low elevations in the CAA (Thomson et al., 2017).

3.7 DISCUSSION & RECOMMENDATIONS

Based on the surveys conducted at Expedition and Tanquary fjords and given our experience with hardware selection, field data acquisition strategies, postprocessing steps, and the generation of final DEM and RGB orthomosaics, it is useful to provide a critical evaluation of each aspect and develop a set of recommendations for improving aerial surveys to achieve optimal results in suboptimal conditions. These are detailed below.

3.7.1 Imaging system

Camera and lens

This study underlines the importance of selecting high performance imaging hardware to ensure high resolving power and image quality, for improved feature detection and matching performance, and in turn more accurate topographic reconstructions. A key point here is that GSD, which is often stated as the only metric for spatial resolution, is only part of the equation. The contribution of system optics including diffraction effects, aberrations, motion blur, and general defocus has to be taken into consideration prior to data acquisition in the field.

Overall, high build quality components with stricter manufacturing requirements ensure a more stable internal camera geometry, including precise alignment and perpendicularity of the optical axis to the focal plane. For the camera body and lens, magnesium alloy offers greater stability than polycarbonates and lowers the risk of mechanical instabilities from thermal effects, vibrations, and shocks. Ideally, a camera should be selected with a global shutter to avoid rolling shutter effects and ensure precise synchronisation between the camera shutter and positioning system. Otherwise, a high X-sync speed (preferably 1/250 s) is necessary to (1) minimise the distance travelled by the camera during exposure and enable more precise camera positioning, and (2) reduce equivalent displacements of imaged objects in pixels to obtain lower distortions in resulting images. Minimising sensor readout time, as well as any deviations of the optical axis, will avoid having to compensate for affinity and non-orthogonality of image pixels and remove at least one unknown parameter from the camera calibration matrix in the alignment step.

Additional key recommendations for imaging components include selecting:

- A high resolution camera with large sensor (ideally full frame) for good sensitivity and spatial resolution.
- A high bit-depth (12–14 bits) sensor for high radiometric resolution and maximal image information in highlights and shadows.
- A prime lens (with a fixed focal length) to ensure stability of the internal camera geometry. In addition, prime lenses typically have higher quality optics with lower aberrations and geometric distortions compared to zoom lenses, which results in higher image quality.
- A wide angle lens with a focal length of 24–35 mm for a wide field of view, giving a large image footprint while minimising geometric distortions.

Image data capture

Capturing high quality image information requires full control over data acquisition, and therefore a camera with the option to control exposure and other in-camera settings during the survey. For more control and flexibility in postproduction, it is important to record images in 16-bit RAW format to retain the full bit-depth as captured by the sensor and minimise the loss of information that occurs when using compressed file formats.

Specific considerations concerning image capture settings and camera configuration can be summarised as follows:

- Avoid fully automatic shooting modes; ideally use aperture priority mode to avoid the internal lens configuration changing during the survey and affecting the camera calibration matrix.

- Use an aperture of f/5.0–5.6 to minimise diffraction effects and aberrations which degrade image quality.
- Use a high shutter speed (1/2000 s should be enough on most cameras) to keep motion blur to a minimum.
- If using aperture priority mode, set EV compensation to -0.3 EV or lower depending on light conditions in order to avoid high ISO and/or slow shutter speeds.
- If capturing JPEGs or other lossy formats, minimise in-camera processing, keeping picture mode 'flat' or 'neutral'.
- Select a wide colour space such as Adobe 1998 RGB instead of sRGB.
- Disable in-camera corrections which compensate for aberrations, especially geometric distortions.
- Disable image stabilisation and other options with the potential to modify image and/or pixel geometry.
- Use an automatic intervalometer for constant image capture intervals.
- Use a sturdy tripod and avoid resting any part of the camera against the body of the aircraft, which will transfer vibrations to the camera body and lens. Alternatively, with the camera handheld, the (camera operator's) body will dampen much of the vibration.
- Use manual focus and ensure that it stays in focus, such as by taping the focus ring.
- If possible, plan for best light conditions and no strong/long shadows. Overcast sky works best for uniform lighting. Avoid early morning or late evening when sun is at a low angle.

3.7.2 Control measurements

Satellite availability

In this study, observations were limited to the 31 operational satellites in the GPS constellation, of which less than half were theoretically visible at any one time (Fig. 3.17). Combining these observations with those from the three other major GNSS constellations would have doubled that number (from $\sim$15 to $\sim$30 potentially visible satellites; https://www.gnssplanning.com). Increased satellite availability can be especially important at high latitudes where poor GDOP due to low signal incidence angles, unfavourable receiver-satellite geometry, and higher ionospheric activity combine to degrade GNSS performance (Leick et al., 2015; Hugentobler and Montenbruck, 2017; Langley et al., 2017). For most of both surveys in this study, at least ten satellites (maximum 12) were observed at any one time, however only in a few cases ($<$10% for EF and $<$5% for TF) were all of the observed satellites used in the PPP solution (Fig. 3.17). For over half of all epochs, at least two satellites were excluded either due to a low elevation angle above the horizon ($<$7.5º), incomplete observations, or large signal residuals. Considering that a minimum of five satellites is required for a valid position fix, and that $\sim$20% of all epochs in both surveys here either have the bare minimum required or are missing valid solutions entirely (Fig. 3.17), increasing satellite availability would increase data continuity while also lowering the GDOP. As of yet, the CSRS-PPP online service is only set up to process GPS and GLONASS observations, but future improvements can be expected to ensure interoperability and compatibility between multiple GNSS constellations and signal frequencies.

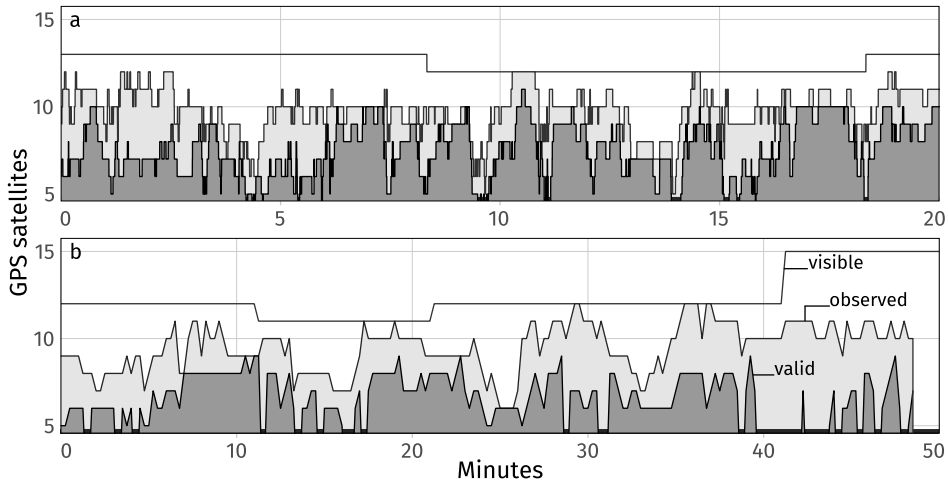

Figure 3.17. GPS satellite availability during the **[a]** EF and **[b]** TF surveys, with (1) the visible satellites (above a 7.5º elevation cutoff) according to the almanac (solid line), (2) observed satellites (light grey), and (3) satellites used in the valid PPP solution for estimating the receiver position (dark grey). Five is the minimum number of satellites required for a valid position fix.

Data logging rate

To investigate the influence of logging rate on the error distribution for PPP solutions, we compared the original EF data, with satellite observables at 10 Hz intervals, to the same observations decimated to 15 s intervals. This shows the predicted uncertainty to be strongly dependent on sampling rate, with the 2-sigma position uncertainty estimates for both the decimated 15 s EF data and the original 15 s TF observations an order of magnitude higher ($>$1–3 m) than those for the 10 Hz EF dataset ($<$0.5 m). A higher sampling rate also helps smooth out some of the variability due to noisy measurements, and more frequent measurements improve data continuity. In case of signal loss, a single missing observation from the TF survey results in a 30 s data gap, and is therefore likely to be more disruptive than a few missing observations from the 10 Hz EF dataset

Both lower logging rates and data gaps affect the performance of the PPP algorithm and are problematic for georeferencing since camera positions between two PPP estimated positions are determined using spline interpolation, with uncertainty growing over time with increasing distance from a position fix. Excluding data gaps, the average distance between any camera and the closest position fix is $<$1 m at EF, and $\sim$100 m at TF. Receiver position estimates between the original high-rate (10 Hz) and decimated (15 s) EF differ by $\pm$1 m in Easting and Northing, while the height difference grows to nearly 4 m over the duration of the survey. However, where data gaps occur the interpolated point coordinates differ by up to a few tens of metres in the horizontal. Figure 3.18 shows the misalignment between the initial reference coordinates assigned to each camera, and the adjusted camera orientations calculated during the bundle adjustment in Metashape. With the 15 s TF data, errors are at a minimum immediately before and after valid GNSS solutions and grow over time with increasing distance from control measurements. On average, errors for cameras within 1 s of a valid measurement are $<$2 m compared to 12 m for those furthest away ($>$6 s). Naturally, errors are highest over data gaps, where GNSS observations are missing or invalid, and camera positions are derived from interpolated point coordinates (Fig. 3.18b). In contrast, there is no visible pattern in the errors for the high rate EF data (Fig. 3.18a), where intervals between logged positions are sufficiently short to prevent interpolated camera positions from deviating too far from a valid position fix. Due to data gaps, 28 cameras from the 10 Hz EF survey were disabled ($\sim$5%), compared to 129 cameras (or 13%) from the 15 s TF survey.

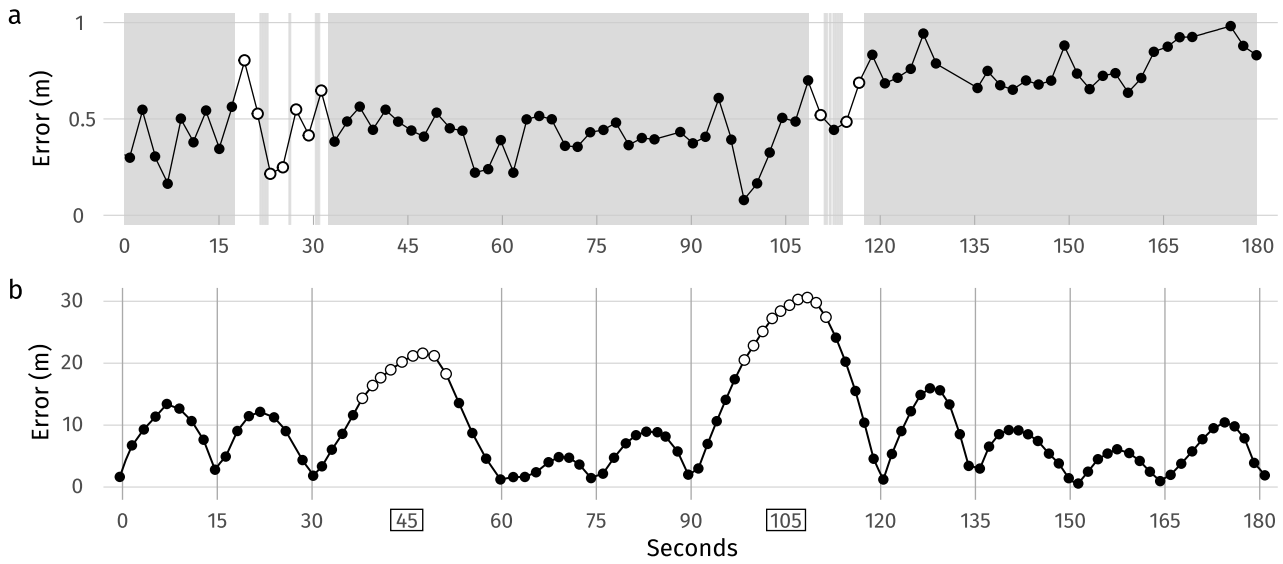

Figure 3.18. Variations in camera position errors over a three minute subset of the **[a]** EF and **[b]** TF surveys. Note differences in vertical scale. Values represent the difference between reference coordinates calculated from GNSS measurements, and positions adjusted during the bundle adjustment performed in Metashape. Solid back circles are for positions derived from valid GNSS solutions shown in [a] at 0.1 s intervals (shaded grey area) and in [b] at 15 s intervals (vertical lines). Empty white circles are for positions interpolated where GNSS solutions are missing.

These observations on the impact of GNSS signal loss and resulting data gaps underline the benefits of improving positioning data continuity. A key recommendation, particularly for surveys undertaken at high latitudes, is to use a multi-frequency and multi-constellation GNSS system, preferably one combining GPS, GLONASS, and Galileo observations. Although perhaps difficult to plan in remote field situations with limited aircraft availability, scheduling the survey during optimum satellite availability could help ensure lower GDOP for more precise measurements. Ensuring a high data logging rate ($<$1 s or better) is crucial for both data continuity and positioning precision. New GNSS receivers also offer higher sensitivity and can track weaker incoming signals and lower measurement noise, enabling higher positioning accuracy. Likewise, newer generation GNSS antennas have higher gain for stronger signal receiving power and improved multipath suppression (Leick et al., 2015). This would be particularly useful in dynamic scenarios onboard moving platforms where frequent cycle slips and high multipath errors affect positioning accuracy. If possible, mounting the antenna outside the aircraft and maintaining shallow bank angles during turns would somewhat help mitigate potential signal loss from aircraft shadowing. Antenna placement should also be considered in relation to the camera sensor, and the offset between the two should be minimised in order to reduce uncertainties in camera position estimates from aircraft attitude changes.

A significant improvement in survey performance can potentially come from integrating the GNSS system with an inertial navigation system (INS) to (1) record attitude changes during flight to account for the effects of the lever arm, and (2) improve continuity and help approximate receiver positions in case of satellite signal loss. INS measure rate of motion parameters using accelerometers (linear displacement) and gyroscopes (rotational state) and, as they require no external references, they are immune to signal disruptions especially common in kinematic positioning. Tightly coupled PPP/INS implementations (GNSS and INS data processed together) can offer improved continuity, allowing solutions to be extrapolated in the event of signal loss. In aerial surveys, loose integration with

additional sensors (data are processed separately) can be used to keep track of attitude changes (Farrell and Wendel, 2017) which removes some of the uncertainty when compensating for the effect of the lever arm. Additional linear displacement data from an accelerometer to provide information on aircraft velocity variations could help with extrapolation of more accurate position estimates over periods of poor satellite visibility.

3.8 CONCLUSIONS

In this study, we present theoretical concepts and practical considerations for the application of photogrammetry techniques for mapping remote glaciers in the Canadian Arctic, an area where aerial surveys are often performed in challenging conditions, including large study sites with complex topography, difficult light conditions, and poor GNSS navigation performance. Based on the results from two surveys conducted at Expedition Fiord and Tanquary Fiord, we identify key limitations and propose a set of recommendations to maximise the quality of results given imperfect conditions.

Together with the specific requirements and expected results of each study, the location, size, and topography of a survey site are the primary aspects determining general survey design. Hardware selection and data acquisition strategies in the field determine the quality and information content of raw data on which every other step in the processing workflow depends. Optimising results therefore requires flexible survey design and the use of high-performance imaging and positioning hardware to enable the acquisition of large quantities of high-quality raw data, with the obvious trade off being increased cost and higher processing power requirements. In terms of image data, the main aspects are high resolving power and low geometric distortions, both of which are crucial for maximising visual content and ensuring robust feature matching over variable topography, and despite perspective distortions. Key considerations for optimising direct georeferencing include positioning data continuity, which primarily depends on GNSS satellite signal availability and integrity, and data logging rate. Additional INS data could further improve positioning performance and help derive more precise control measurements which better take into account aircraft attitude. When coupled with precise synchronisation with the camera sensor, INS-aided GNSS navigation could help reduce uncertainties in camera position estimates and ensure accurate orthorectification of topographic reconstructions.

An original contribution of this study is the method for deriving camera position estimates from PPP processed positioning data, described in detail in the Appendix. The process takes into account uncertainties inherent to GNSS data processing and additional factors associated with data acquisition in the field, including flight dynamics and camera sensor technology. With direct georeferencing, understanding the various error sources which degrade positioning accuracy is necessary to avoid overfitting the topographic reconstruction to imprecise control measurements and propagating those errors to the final outputs.

The accessibility of low-cost equipment and the largely automated SfM-MVS workflow requires little expertise in photogrammetry techniques, or the related fields of GNSS technology and satellite navigation, imaging optics, and signal processing. On the other hand, unlike many remotely sensed satellite products which come pre-processed and analysis-ready, SfM-MVS processing demands one to be more than an end-user. Integrating all aspects of the workflow is challenging and data quality can be highly variable from one study to the next. A significant challenge

for undertaking a comprehensive error assessment is determining the exact contribution of all components involved and quantifying their effect on the final results. While the ultimate goal is mapping a given surface with high precision and accuracy, conducting surveys in suboptimal conditions where results are not necessarily expected to be of the highest quality, provides an opportunity for improving our understanding of those factors with the highest influence on final outputs and study outcomes.

When building long-term datasets, recording raw unprocessed data (avoiding lossy formats) is especially valuable for monitoring dynamic processes, including in glaciological studies where small ice masses are disappearing at increasing rates. Repeated surveys to monitor ongoing changes, and the collection of high-resolution data to allow continued investigations after those glaciers are gone, are invaluable for long term records.

APPENDIX

Calculation of camera positions

The following describes the detailed steps used to calculate camera positions at the time of exposure from estimated GPS receiver positions in the east, north, and up directions, with positioning uncertainties stated using 2-sigma error bounds for vertical (linear error, σu) and horizontal (radial error, $2drms = \sqrt{\sigma e^2 + \sigma n^2}$) positions. These calculations were specifically developed for PPP-processed positioning data recorded during helicopter-based air photo surveys, but in principle the same method can be applied to any GNSS data acquired onboard rotor or fixed-wing aircrafts, as long as the lever arm (offset between the camera and GNSS antenna) is known.

Where data gaps exist in the GPS data, we approximate the flightpath using spline interpolation and fill the missing information at regular time intervals corresponding to the GPS receiver logging rate. We allow the corresponding positioning errors to grow linearly with time and therefore to increase further from valid GPS positions. The same is done to calculate receiver coordinates and estimated errors based on the precise timestamp of the event flag records associated with each captured image.

Step 1: Determine aircraft ground track (bearing)
Calculate displacement along aircraft ground track in easting (e) and northing (n) to derive bearing relative to geographic north (α):

$$\Delta e = e_i - e_{i-1} \quad \text{and} \quad \Delta n = n_i - n_{i-1}$$
$$\alpha = arctan2(\Delta n, \Delta e) \tag{3.8}$$

The two-argument arctangent function $atan2(y, x)$ keeps track of the respective signs of x and y and returns and angle in $[-\pi, \pi]$ giving a single result. In comparison, the single argument $atan(y/x)$ returns an angle in $[-\pi/2, \pi/2]$ and cannot distinguish between two opposite directions, giving an ambiguous result. Here the track is referenced to the East-North-Up (ENU) coordinate system where 0º is East, and angles are positive in the counterclockwise direction and negative clockwise. Uncertainty in displacement in each direction is calculated from:

$$\delta\Delta e = \sqrt{\delta e_i^2 + \delta e_{i-1}^2} \quad \text{and} \quad \delta\Delta n = \sqrt{\delta n_i^2 + \delta n_{i-1}^2} \tag{3.9}$$

Uncertainty in estimated bearing direction is calculated following general error propagation theory and first-order Taylor series expansion, using partial derivatives with respect to each error source:

$$\delta\alpha_e = \left|\frac{\partial\alpha}{\partial\Delta e}\right| \delta\Delta e = \left|-\frac{\Delta n}{\Delta e^2 + \Delta n^2}\right| \delta\Delta e$$
$$\delta\alpha_n = \left|\frac{\partial\alpha}{\partial\Delta n}\right| \delta\Delta n = \left|\frac{\Delta e}{\Delta n^2 + \Delta e^2}\right| \delta\Delta n \tag{3.10}$$

With final bearing error: $\delta\alpha = \sqrt{\delta\alpha_e^2 + \delta\alpha_n^2}$

Step 2: Determine bearing of camera offset

The camera/antenna offset along three orthogonal axes with respect to the aircraft body reference frame with measurement error is defined as:

$x \pm \delta x$ camera offset along the longitudinal (x) axis (positive out the nose)

$y \pm \delta y$ camera offset along the transverse (y) axis (positive out the left wing)

$z \pm \delta z$ camera offset along the vertical (z) axis (positive up)

For simplicity, instead of following the convention for describing aircraft attitude in the North-East-Down (NED) coordinate system, the camera/antenna offset is directly aligned to the ENU system with the longitudinal x axis pointing east. Converting the relative offset from the local (aircraft reference frame: XYZ) to the global (world reference frame: ENU) coordinate system involves a series of rotations described by Euler angles, where yaw, pitch, and roll each represent a rotation by the ψ, θ, ϕ angles about the z, y, x axes, with aircraft attitude defined by:

$\psi \pm \delta\psi$ yaw: rotation about the vertical (z) axis, taken to be equivalent to the direction of travel $\alpha \pm 15$º

$\theta \pm \delta\theta$ pitch: rotation about the transverse (y) axis, taken to be 0º $\pm$ 15º

$\phi \pm \delta\phi$ roll: rotation about the longitudinal (x) axis, taken to be 0º $\pm$ 30º

These values for angular errors were chosen as representative of maximum yaw, pitch, and roll angles for a typical helicopter flight (Personal communication, Grech, 2019).

$$
\begin{aligned}
R_z(\psi) &= \begin{bmatrix} cos\psi & -sin\psi & 0 \\ sin\psi & cos\psi & 0 \\ 0 & 0 & 1 \end{bmatrix} \\
R_y(\theta) &= \begin{bmatrix} cos\theta & 0 & sin\theta \\ 0 & 1 & 0 \\ -sin\theta & 0 & cos\theta \end{bmatrix} \\
R_x(\phi) &= \begin{bmatrix} 1 & 0 & 0 \\ 0 & cos\phi & -sin\phi \\ 0 & sin\phi & cos\phi \end{bmatrix}
\end{aligned}
\tag{3.11}
$$

Commonly used in aeronautics, the 3-2-1 Euler angle triad combines three successive rotations in a single 3×3 rotation matrix R preserving the order of rotation: first yaw, then pitch, then roll (Collinson, 2011). Rotating the camera offset measurements x, y, z by matrix R, where ψ (yaw) is equivalent to the bearing of the aircraft and θ (pitch) and ϕ (roll) are kept at 0º, performs a rotation about the yaw axis, aligning the updated offset coordinates x', y', z' with the direction of travel. Note that in the ENU reference frame a positive rotation about the z (yaw), y (pitch), and x (roll) axes results in nose left, nose down, and left wing up respectively (which is the inverse of the direction of rotation used by convention in the NED system).

$$
\begin{bmatrix} x' \\ y' \\ z' \end{bmatrix} = R(\psi, \theta, \phi) \begin{bmatrix} x \\ y \\ z \end{bmatrix} \tag{3.12}
$$

$$R(\psi,\theta,\phi) = \begin{bmatrix} cos\psi\ cos\theta & cos\psi\ sin\theta\ sin\phi - sin\psi\ cos\phi & cos\psi\ sin\theta\ cos\phi + sin\psi\ sin\phi \\ sin\psi\ cos\theta & sin\psi\ sin\theta\ sin\phi + cos\psi\ cos\phi & sin\psi\ sin\theta\ cos\phi - cos\psi\ sin\phi \\ -sin\theta & cos\theta\ sin\phi & cos\theta\ cos\phi \end{bmatrix}$$

Camera positions are obtained by combining the updated offset x', y', z' and original antenna positions e, n, u:

$$e_{cam} = e + x' \qquad n_{cam} = n + y' \qquad u_{cam} = u + z' \tag{3.13}$$

Step 3: Camera position uncertainty

Uncertainties in aircraft attitude are computed using the matrix of partial derivatives for each row of R in respect to each of x, y, z and ψ, θ, ϕ:

$$\begin{bmatrix} \frac{\partial R_1}{\partial x} & \frac{\partial R_1}{\partial y} & \frac{\partial R_1}{\partial z} & \frac{\partial R_1}{\partial \psi} & \frac{\partial R_1}{\partial \theta} & \frac{\partial R_1}{\partial \phi} \\ \frac{\partial R_2}{\partial x} & \frac{\partial R_2}{\partial y} & \frac{\partial R_2}{\partial z} & \frac{\partial R_2}{\partial \psi} & \frac{\partial R_2}{\partial \theta} & \frac{\partial R_2}{\partial \phi} \\ \frac{\partial R_3}{\partial x} & \frac{\partial R_3}{\partial y} & \frac{\partial R_3}{\partial z} & \frac{\partial R_3}{\partial \psi} & \frac{\partial R_3}{\partial \theta} & \frac{\partial R_3}{\partial \phi} \end{bmatrix} \tag{3.14}$$

The same is then repeated for R_1, R_2, and R_3. If:

$$\begin{aligned} R_1 = {} & x\ (cos\psi\ cos\theta) \\ & +\ y\ (cos\psi\ sin\theta\ sin\phi - sin\psi\ cos\phi) \\ & +\ z\ (cos\psi\ sin\theta\ cos\phi + sin\psi\ sin\phi) \end{aligned} \tag{3.15}$$

Then:

$$\begin{aligned} \partial R_1/\partial x &= cos\psi\ cos\theta \\ \partial R_1/\partial y &= cos\psi\ sin\theta\ sin\phi - sin\psi\ cos\phi \\ \partial R_1/\partial z &= cos\psi\ sin\theta\ cos\phi + sin\psi\ sin\phi \\ \partial R_1/\partial \psi &= x\ (-sin\psi\ cos\theta) \\ &\quad + y\ (-sin\psi\ sin\theta\ sin\phi - cos\psi\ cos\phi) \\ &\quad + z\ (-sin\psi\ sin\theta\ cos\phi + cos\psi\ sin\phi) \\ \partial R_1/\partial \theta &= x\ (cos\psi\ -sin\theta) \\ &\quad +\ y\ (cos\psi\ cos\theta\ sin\phi) \\ &\quad +\ z\ (cos\psi\ cos\theta\ cos\phi) \\ \partial R_1/\partial \phi &= y\ (cos\psi\ sin\theta\ cos\phi + sin\psi\ sin\phi) \\ &\quad +\ z\ (cos\psi\ sin\theta\ -sin\phi + sin\psi\ cos\phi) \end{aligned}$$

Note that the uncertainty in the yaw angle ϕ combines both the uncertainty in the bearing of the aircraft as estimated from the uncertainty in displacement between consecutive GPS position estimates (Δe and Δn), as well as a constant attitude error estimate for yaw of $\pm$15º. After rotation, the uncertainty in the updated offset coordinates is approximated by adding all sources of error in quadrature:

$$\delta x' = \left[\left(\frac{\partial R_1}{\partial x}\delta x\right)^2 + \left(\frac{\partial R_1}{\partial y}\delta y\right)^2 + \left(\frac{\partial R_1}{\partial z}\delta z\right)^2 + \left(\frac{\partial R_1}{\partial \psi}\delta \psi\right)^2 + \left(\frac{\partial R_1}{\partial \theta}\delta \theta\right)^2 + \left(\frac{\partial R_1}{\partial \phi}\delta \phi\right)^2\right]^{\frac{1}{2}}$$
$$\delta y' = \left[\left(\frac{\partial R_2}{\partial x}\delta x\right)^2 + \left(\frac{\partial R_2}{\partial y}\delta y\right)^2 + \left(\frac{\partial R_2}{\partial z}\delta z\right)^2 + \left(\frac{\partial R_2}{\partial \psi}\delta \psi\right)^2 + \left(\frac{\partial R_2}{\partial \theta}\delta \theta\right)^2 + \left(\frac{\partial R_2}{\partial \phi}\delta \phi\right)^2\right]^{\frac{1}{2}}$$
$$\delta z' = \left[\left(\frac{\partial R_3}{\partial x}\delta x\right)^2 + \left(\frac{\partial R_3}{\partial y}\delta y\right)^2 + \left(\frac{\partial R_3}{\partial z}\delta z\right)^2 + \left(\frac{\partial R_3}{\partial \theta}\delta \theta\right)^2 + \left(\frac{\partial R_3}{\partial \phi}\delta \phi\right)^2\right]^{\frac{1}{2}}$$

Then the camera position errors for each epoch are combined with the original 2-sigma horizontal ($2drms = \sqrt{\sigma e^2 + \sigma n^2}$) and vertical ($\sigma u$) GPS receiver position errors, with those corresponding to recorded event flags combining the uncertainties of both epochs immediately before and after image capture:

$$\delta H_{cam} = \sqrt{2drms^2 + \delta xy'^2}$$
$$\delta U_{cam} = \sqrt{\sigma u^2 + \delta z'^2} \tag{3.16}$$

Finally, the uncertainty related to the synchronization between the camera shutter and GPS receiver is approximated by taking into account the curtain travel time t:

$$\delta H_{final} = \sqrt{\delta H_{cam}^2 + (\Delta h/t)^2}$$
$$\delta U_{final} = \sqrt{\delta U_{cam}^2 + (\Delta u/t)^2} \tag{3.17}$$

Final camera position accuracy estimates approximate the relative contribution of each error source, in this case combining horizontal and vertical positioning uncertainties with expected aircraft attitude errors propagated down the length of the lever arm and distance travelled during shutter motion (Table 3.4).

Table 3.4. GNSS and camera positioning errors for the two surveys in this study

	Tanquary Fiord (TF) 2018		Expedition Fiord (EF) 2019	
Lever arm measurements:				
Length X×Y×Z	−1.5 ×−1.5 ×−0.8 m		−0.17 × 0.31 × 0.07 m	
Lever arm measurement error	± 0.25 m		± 0.10 m	
Total offset	2.4 ± 0.43 m		0.36 ± 0.17 m	
Yaw pitch roll angular errors:				
Default uncertainties only	± 15º, 15º, 30º		± 15º, 15º, 30º	
Lever arm measurement uncertainty	± 6.3º, 7.6º, 8.4º		± 16.2º, 31.2º, 18º	
Yaw, pitch, roll linear errors:				
Default uncertainties only	0.59, 0.49, 0.88 m		0.09, 0.05, 0.17 m	
Total	1.17 m		0.19 m	
Including lever arm measurement uncertainty	0.64, 0.55, 0.91 m		0.14, 0.11, 0.19 m	
Total	1.25 m		0.16 m	
	Mean	Max	Mean	Max
Camera travel during shutter motion:				
Horizontal (Easting, Northing)	0.14 m	0.18 m	0.12 m	0.19 m
Vertical (Up)	<0.01 m	0.02 m	<0.01 m	0.03 m
Camera positioning errors:				
Horizontal (Easting, Northing)	1.43 m	3.14 m	0.19 m	0.39 m
Vertical (Up)	2.76 m	11.77 m	0.35 m	0.61 m
Final camera position errors:				
Horizontal (Easting, Northing)	1.68 m	3.25 m	0.28 m	0.45 m
Vertical (Up)	2.98 m	11.77 m	0.40 m	0.64 m
Total (ENU)	3.48 m	12.19 m	0.49 m	0.78 m

4

Rapid demise of a small glacier in the Tanquary Fiord region, Ellesmere Island, Canadian High Arctic

ABSTRACT In this study, we assess the long-term changes in ice extent and determine the geodetic mass balance of Bowman Glacier, a small mountain glacier currently consisting of several disconnected ice masses. We use historical and recent aerial photography and structure from motion (SfM) multiview stereo (MVS) techniques to reconstruct glacier surface topography in 1959 and 2018, and calculate ice surface elevation change over six decades. This is combined with optical satellite imagery to reconstruct the evolution in extent of the glacier over the past 60 years, and ground penetrating radar measurements of ice thickness to estimate the remaining ice volume. Between 1959 and 2020, Bowman Glacier lost 78% of its original extent (reducing from 2.75 km^2 to 0.61 km^2), while average annual area loss rates have nearly tripled in the past two decades. Over the 1959–2018 period, glacier-wide ice thickness change averaged -22.7 ± 4.7 m, corresponding to a mean specific annual mass balance of -347.0 ± 71.4 mm w.e. a^{-1}. Projecting the average rates of area and volume change into the future indicates the glacier will likely entirely disappear between 2030 and 2060. This study demonstrates the use of SfM-MVS processing techniques to generate elevation products from 1950–60s historical aerial photographs in the Canadian Arctic, which creates the potential to extend regional observations of ice elevation and glacier volume change prior to the satellite record. Quantifying geodetic mass balance is especially valuable given the rapid changes affecting small glaciers in the region, many of which, similar to Bowman Glacier, are likely to disappear within a few decades.

4.1 INTRODUCTION

Glaciers and ice caps in the Canadian Arctic Archipelago (CAA) cover $\sim$146,000 km^2, the largest ice covered area outside of the ice sheets. Ice loss in the region has accelerated in recent decades due to enhanced meltwater runoff (Gardner et al., 2011; Lenaerts et al., 2013; Noël et al., 2018), with losses for the 2000–19 period occurring at one of the highest rates in the world at -57.1 ± 9.1 Gt a^{-1} (split between -30.6 ± 4.8 Gt a^{-1} for CAA North and -26.5 ± 4.3 Gt a^{-1} for CAA South; Hugonnet et al., 2021). Regional mass balance estimates have generally

been derived from satellite altimetry (Gardner et al., 2011), gravimetry (Gardner et al., 2011; Ciracì et al., 2020), and stereoscopic imagery (Hugonnet et al., 2021), or regional climate models (Gardner et al., 2011; Lenaerts et al., 2013; Noël et al., 2018). While valuable for monitoring ice volume change on a large scale, these products generally suffer from limited spatial resolution and struggle to resolve changes on small ice masses with complex geometries. Additionally, small glaciers are notoriously underrepresented in both regional and global glacier inventories (Parkes and Marzeion, 2018). Meanwhile, smaller glaciers in the CAA are experiencing greater retreat rates and overall area loss than large ice masses, with some small glaciers disappearing entirely since 2000 (Serreze et al., 2017; Sharp et al., 2014; Thomson et al., 2011; White and Copland, 2018). For example, White and Copland (2018) reported that glaciers <1 km^2 across northern Ellesmere Island lost area at an average rate of 30.4% decade^{-1} over the period 1999–2015, compared to a mean loss rate of 0.4% decade^{-1} for glaciers >1000 km^2.

Determination of past glacier fluctuations requires long-term monitoring programs, but regular observations of changes in ice extent, surface elevation, and ice thickness exist for only a few individual glaciers across the CAA. In situ measurements are time-consuming, logistically expensive, and are understandably impossible to implement on more than a limited sample of glaciers. Yet, the current trend of accelerated mass loss highlights the importance of long-term datasets for detecting change over decadal timescales, and the need for elevation products for deriving geodetic mass balance estimates prior to the satellite record. Air photo surveys conducted by the Royal Canadian Air Force in the late 1950s and early 1960s provided the basis for the regional topographic maps for the CAA, which were then used to generate the first version of a digital elevation model (DEM) for the region, the Canadian Digital Elevation Data (CDED). However, earlier elevation products generated using photogrammetric methods contained considerable errors, particularly in the accumulation area of glaciers and ice caps with few bedrock features to match. For example, on Axel Heiberg Island in the northern CAA, the CDED contained elevation errors of >90 m (Cogley and Jung-Rothenhäusler, 2004), making it essentially impossible to derive geodetic mass balance estimates. To our knowledge, very few recent studies have made direct use of stereo photogrammetry from 1950s–60s aerial photography to derive elevation data products over glaciers in the region (Burgess and Sharp, 2008).

More recently, Structure from motion (SfM) photogrammetry coupled with multiview stereo (MVS) reconstruction techniques have been applied to two glaciers in the CAA (Thomson and Copland, 2016; Bash et al., 2018). Thomson and Copland (2016) created a DEM of the surface of White Glacier in Expedition Fiord, Axel Heiberg Island, using SfM-MVS methods applied to oblique air photos from a 2014 survey and determined geodetic mass change from comparison with a 1:10,000 topographic map derived from 1960 aerial photography (Thomson et al., 2017). Contour lines in the 1960 map were digitised to produce a DEM of the area which was then compared to the 2014 DEM (Thomson et al., 2017). The downside of this method is that manual digitisation is time consuming and impractical for large study areas, and errors in topographic map data and uncertainties associated with interpolating elevation contours are propagated to the DEM and to surface change measurements. Perhaps more importantly, Expedition Fiord is well mapped compared to most of the CAA, where few previous small-scale topographic products exist to compare with recent data. An ability to directly use 1950s–60s aerial photography in current SfM-MVS processing would allow more accurate historical topographic reconstructions to be undertaken across the CAA, and geodetic mass balance estimates to be made for previously unstudied glaciers.

Here, we assess long-term changes of Bowman Glacier, a small mountain glacier located in Tanquary Fiord, northern

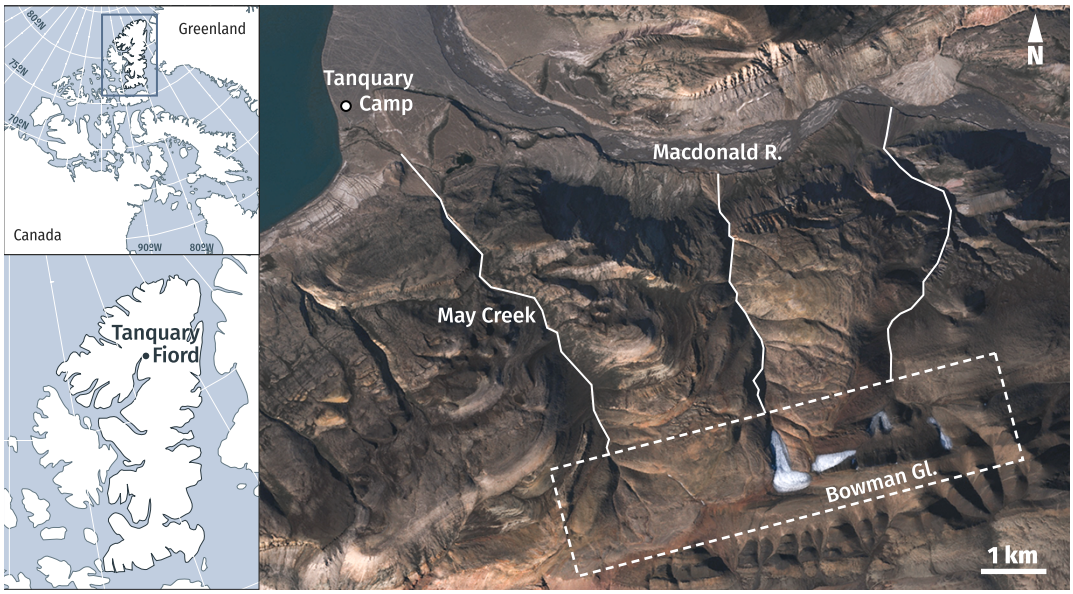

Figure 4.1. Study area near Tanquary Fiord, Ellesmere Island, with location of Bowman Glacier (dashed white box) and its three main drainage valleys (white lines), including May Creek which provides the main water supply for Tanquary camp. Base image: Sentinel 2A, 24 July 2020.

Ellesmere Island (Fig. 4.1). We use SfM-MVS processing applied to aerial photography to reconstruct glacier surface topography in 1959 and 2018, producing detailed DEMs and orthomosaics for a small ice mass in the CAA. These provide information concerning long-term ice surface elevation changes and allow determination of the geodetic mass balance of the glacier over a 60 year period. This is combined with optical satellite data to reconstruct the evolution in extent of the glacier over the past six decades, and ground penetrating radar (GPR) measurements of ice thickness to estimate the remaining ice volume. This information is compared with Regional Atmospheric Climate Model (RACMO) surface mass balance data from the last six decades, and changes are projected into the future to estimate the life expectancy of the remaining ice mass.

4.2 STUDY SITE

Bowman Glacier (81.35ºN, 76.45ºW) currently consists of several small disconnected ice masses, located about 10 km southeast of the Parks Canada basecamp at the head of Tanquary Fiord, Ellesmere Island, Nunavut, Canada (Fig. 4.1). Established in 1963 by the Defence Research Board as a scientific field station, the camp now serves as the headquarters of Quttinirpaaq National Park. Lying on a plateau that reaches ~1200 m above sea level (a.s.l.), Bowman Glacier is located on the western edge of the Hazen Plateau, a sparsely glaciated area between the Northern Ellesmere Icefields to the north, and Agassiz Ice Cap to the south. When Tanquary camp was established, Bowman Glacier drained into three main valleys, with the eastern and central drainage basins feeding into Macdonald River to the north, and the western one providing the main water supply for the camp via May Creek (Figs 4.1 and 4.2). The initial motivation for this study was to estimate the remaining life expectancy of Bowman Glacier and to determine its viability as the primary water source for Tanquary camp.

Previous observations on the glacier include only a “limited assessment of snow cover and ablation” from 1966

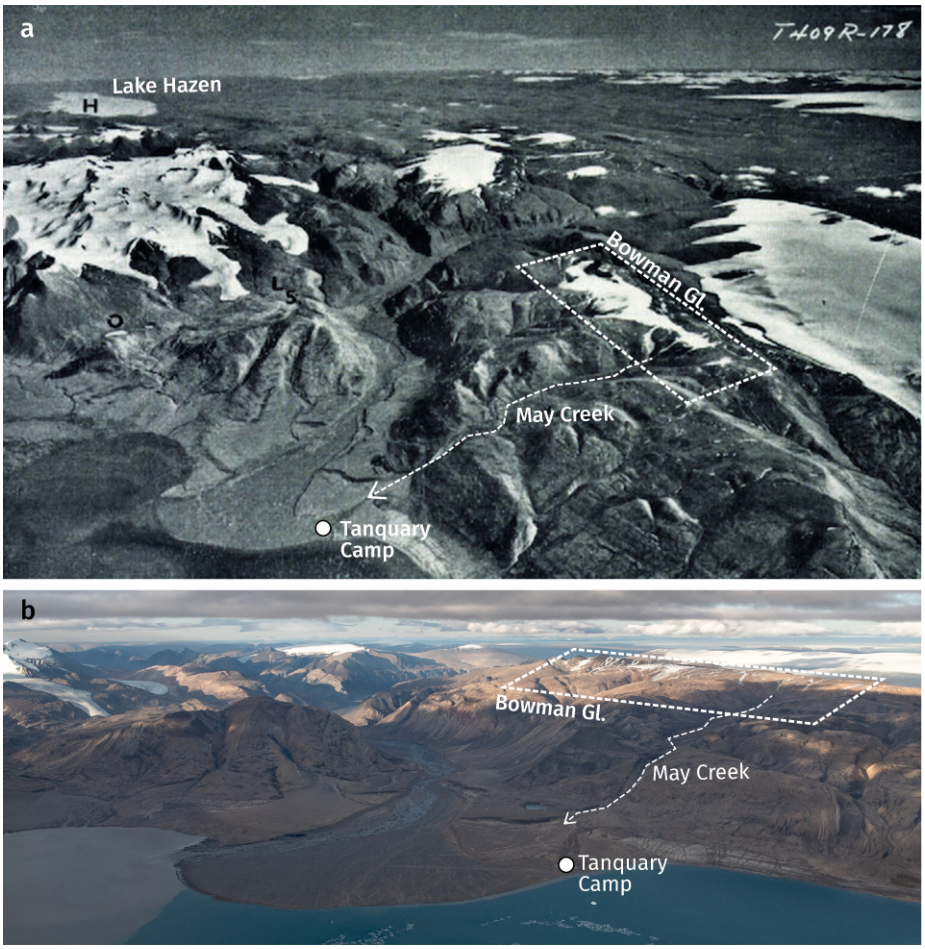

Figure 4.2. **[a]** Oblique air photo (T409R-178) from 16 July 1950 (Hattersley-Smith, 1969a), with location of Bowman Glacier, May Creek, and Tanquary camp. Lake Hazen, some 80 km to the north-east, is visible in the top left corner. **[b]** Oblique air photo taken during the helicopter survey on 3 August 2018. Dashed white box in [a] and [b] indicates same region as in Fig. 4.1.

(Hattersley-Smith and Oliver, 1967). Although Hattersley-Smith (1969a) briefly mentions Bowman Glacier as part of a regional summary of glacial features, there is no previous published work on the ice mass. The earliest known images of the glacier are from a trimetrogon survey flown by the Royal Canadian Air Force (RCAF) in July 1950 (Cogley and Adams, 2000), which include both nadir and oblique photos (Hattersley-Smith, 1969a) (Fig. 4.2a). The primary photographic record of Bowman Glacier was acquired in summer 1959, when the RCAF completed comprehensive nadir photography flights across the CAA at a scale of 1:60,000, which were used to derive the standard 1:250,000 and 1:50,000 scale maps of the region.

4.3 MATERIALS AND METHODS

4.3.1 Ice extent

A combination of aerial photographs and satellite imagery were used to reconstruct the ice extent of Bowman Glacier between 1959 and 2020 (Table 4.1; Fig. 4.3). The 1959 extent was manually outlined from an 8 m panchromatic orthomosaic (Fig. 4.3a) generated from air photos using SfM-MVS processing as detailed further in section 4.3.2. A 10 m resolution SPOT-1 (Satellite pour l'observation de la Terre) panchromatic image was used to manually outline the 1987 extent (Fig. 4.3b; Table 4.1). All manual digitisation was performed in QGIS (version 3.12.2).

Changes in ice extent since 2000 were mapped at five-year intervals from Landsat 7 ETM+ (2000–10) and Landsat 8 OLI (2015–20) multispectral imagery (Table 4.1) using raw digital number data and the normalised difference snow index (NDSI). The NDSI takes advantage of the contrast in spectral reflectance between snow-covered terrain and surrounding rock areas, and is calculated from the green and shortwave infrared (SWIR) bands from: (green – SWIR) / (green + SWIR) (e.g. Paul et al., 2015). Orthorectified Landsat data (Level 1T) were accessed through the Google Earth Engine service and processed using a custom script and the online JavaScript code editor. For each year, all suitable cloud-free images acquired in the summer months (June–August) were reprojected to a common coordinate reference system (WGS 84, UTM 18N) and used to compute band ratio images, which were then combined to generate a single median NDSI raster with 30 m pixel size. An assigned threshold value separating glacier ice from surrounding terrain was used to derive binary images indicating the presence or absence of ice.

Table 4.1. Optical satellite imagery used for mapping ice extent. SPOT-1 HRV: Satellite pour l'observation de la Terre High resolution visible; ETM+: Enhanced Thematic Mapper Plus; OLI: Operational Land Imager; SWIR: Shortwave infrared

Mission, sensor	Band	Wavelength	Year	Date range	No. of scenes	NDSI threshold
SPOT-1 HRV 2	Pan	0.51–0.73 µm	1987	Aug. 20	1	–
Landsat 7 ETM+	Green (B2)	0.52–0.60 µm	2000	June 20–28	5	0.32
	SWIR1 (B5)	1.55–1.75 µm	2005	July 11–31	9	0.30
			2010	June 29 – July 22	8	0.28
Landsat 8 OLI	Green (B3)	0.53–0.59 µm	2015	July 09 – Aug. 17	27	0.10
	SWIR1 (B6)	1.57–1.65 µm	2020	July 09 – Aug. 17	38	0.10

For 2015 and 2020, there were >25 suitable Landsat 8 scenes available for each summer season, compared to <10 Landsat 7 scenes for earlier years. Using a multitemporal image stack helps fill data gaps from the banding caused by the scanline corrector failure on the ETM+ instrument starting in 2003. Another advantage of using multiple images is a lower sensitivity to variations in illumination such as shadows due to changing sun angles, and differences in snow cover due to persistent snow patches in early summer and snowfall events later in the season. This is especially effective for 2015 and 2020 with the increased availability of Landsat 8, as the median NDSI remains more stable between years and the threshold value separating the glacier surface from ice-free terrain was kept constant at 0.10, with any pixel with a value above the threshold being classified as ice. With fewer images available for 2000–10, median NDSI values were more variable so the threshold was adjusted between 0.28–0.32. Additional factors accounting for the difference in assigned thresholds for OLI vs ETM+ imagery include the difference in the wavelengths of the green and SWIR bands (Table 4.1), and different gain values used for the two sensors.

In order to remove isolated pixels and smooth object boundaries, a morphological opening operation, consisting of an erosion followed by a dilation, was performed on the binary images. With both operations applied within the same three-pixel kernel, the erosion shrinks clusters of contiguous pixels and removes small objects, while the dilation restores larger objects, mostly preserving their shape and size. It is effective at reducing noise due to patches of seasonal snow being incorrectly classified as ice. The smoothed binary images were then vectorized to produce glacier outlines, which were exported from Google Earth Engine for further processing in QGIS.

On years when significant snow cover persisted throughout the summer (i.e., 2000 and 2005; Fig. 4.3c-d), the opening operation failed to filter some of the larger snowpatches. In those cases, we used the 1959 glacier outlines, corresponding to the maximum ice extent for the study period, and excluded all individual patches of pixels falling

entirely outside this boundary. Like other automated classification methods, the NDSI struggles with correctly identifying glacier ice in strong shadows, and some outlines (particularly near the terminus) had to be manually adjusted based on visual inspection of false colour composite Landsat images. Additional high-resolution Digital Globe imagery from the summers of 2008 (Quickbird 2, 8 June 2008, 0.6 m resolution) and 2011 (Worldview 2, 22 July 2011, 0.5 m resolution) was used as reference to help differentiate perennial snow from glacier ice. We calculate uncertainties in glacier area using a $\pm 1/2$ pixel buffer, similar to Granshaw and Fountain (2006). Relative errors increase with decreasing glacier size, and range between 4% of glacier extent for the higher resolution 1987 SPOT-1 image, and 16–24% for the coarser 30 m Landsat data for 2000–20.

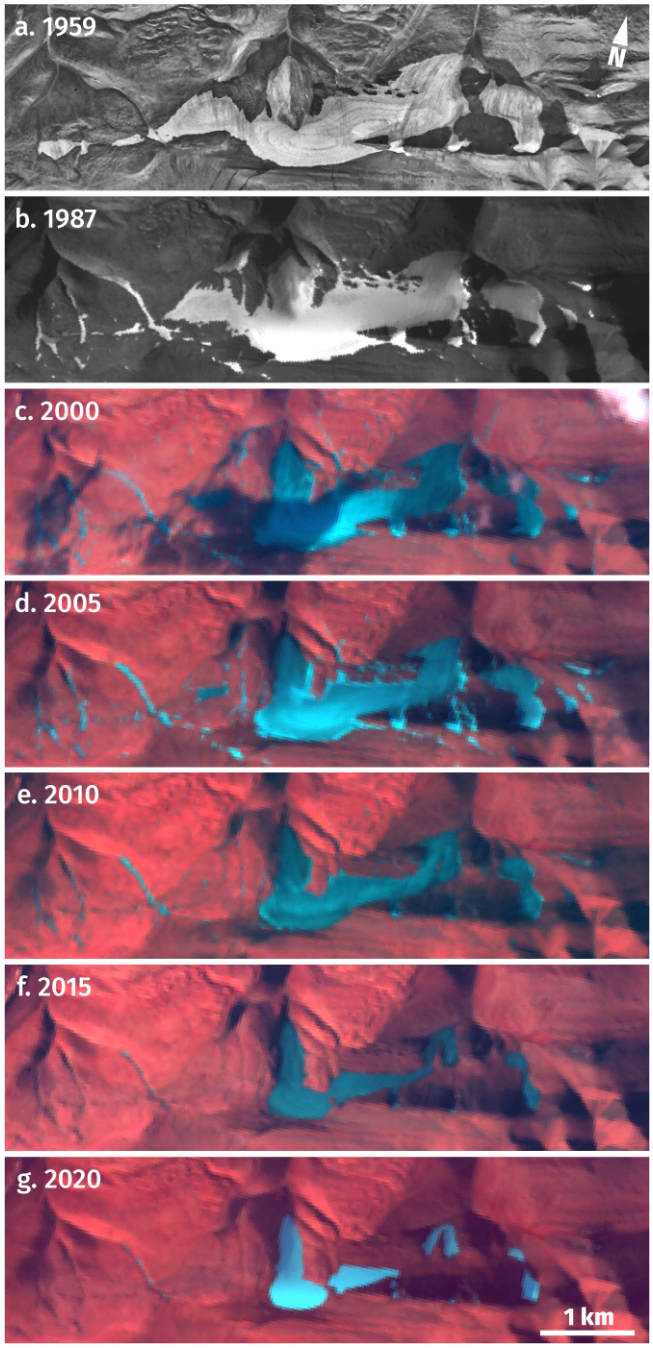

Figure 4.3. Evolution of Bowman Glacier over the period 1959–2020 from aerial photography [a], and optical satellite imagery [b-g].
Panchromatic images: **[a]** orthomosaic from August 1959 air photos; **[b]** SPOT-1 20.08.1987;
False colour composites: **[c]** Landsat 7 24.06.2000; **[d]** Landsat 7 25.07.2005; **[e]** Landsat 7 30.06.2010; **[f]** Landsat 8 25.07.2015; **[g]** Landsat 8 17.08.2020.

4.3.2 Ice surface elevation

The full SfM-MVS workflow summarised below (and detailed in Chapter 3) was performed in Agisoft Metashape Pro (version 1.6). Additional point cloud filtering and distance computations between the 1959 and 2018 point clouds were undertaken in CloudCompare (version 2.11.1). The final point clouds were used to derive georeferenced DEMs and orthomosaics of the study area.

Ice surface reconstruction: 1959

The 1959 surface topography was determined from a series of panchromatic 1:60,000 scale vertical aerial photographs from 29 July 1950 (roll A16691, photos 49–52) and 26 August 1959 (roll A16788, photos 62–65 & 77–80). Images were acquired from an altitude of 9000 m a.s.l. with a Wild RC5A aerial film camera and Aviogon lens (15 AG) with a nominal focal length of 153 mm. With each 9×9 in (22.9×22.9 cm) image scanned at 300 dpi, the pixel pitch is 84.6 µm and the equivalent ground sampling distance is $\sim$5 m. A total of 12 overlapping air photos from three different flightlines (two of which were flown on the same day) were imported into Metashape, where fiducial marks (four marks, one in each corner) were manually placed on each photo and used to automatically align and scale photos to the same dimensions. A single mask was applied to the full dataset to exclude the outer frame from the scanned photos.

After the image alignment step, the sparse cloud was georeferenced to the 2018 DEM based on 13 control points in proximity to the 1959 ice extent (Fig. 4.4a). Distinct stable bedrock features were manually selected in the 2018 dense point cloud, and subsequently identified in the 1959 air photos. Features were selected to ensure positional accuracy of 10 m or less (the equivalent of ±2 pixels), and each was positioned on 4–6 photos. The georeferenced cloud was optimised and points with reprojection errors $>$0.25 pixels were deleted (about 10% of original point count). The final cloud contained $\sim$49,000 points with root mean square (RMS) reprojection errors of 0.24 pixels. Combining all 13 control points, RMS registration errors were 6.53 m in total, or 5.75 m in horizontal and 3.09 m in vertical. The dense point cloud, generated with the ultra-high quality setting and aggressive filtering in Metashape, contained nearly 16 million points.

Ice surface reconstruction: 2018

Our aerial photo survey took place on 3 August 2018 onboard an Airbus ASTAR 350 B2 helicopter. We surveyed an area of roughly 70 km^2 over an elevation range of nearly 1000 m, including the Bowman Glacier summit plateau and the three main valleys in its drainage basin. The aircraft maintained a constant altitude of $\sim$1400 m a.s.l., or between 50 and 1350 m above ground level (a.g.l.), covering a linear distance of $\sim$85 km in just under an hour of flying time. Over 1000 oblique images were captured with a Nikon D850, a full-frame (35 mm) digital single-lens reflex camera, and a 24 mm prime lens (NIKKOR AF-S 24 mm f/1.8G ED).

Georeferencing was achieved using direct control measurements acquired with a global positioning system (GPS), including a survey-grade dual frequency (L1/L2 bands) Trimble R7 receiver and Zephyr 1 Geodetic antenna. Prior to the scheduled survey, the GPS system was used to record the precise position of two checkered flags (1×1 m) with a minimum occupation time of 30 minutes (Fig. 4.4b). The two targets were used as checkpoints for

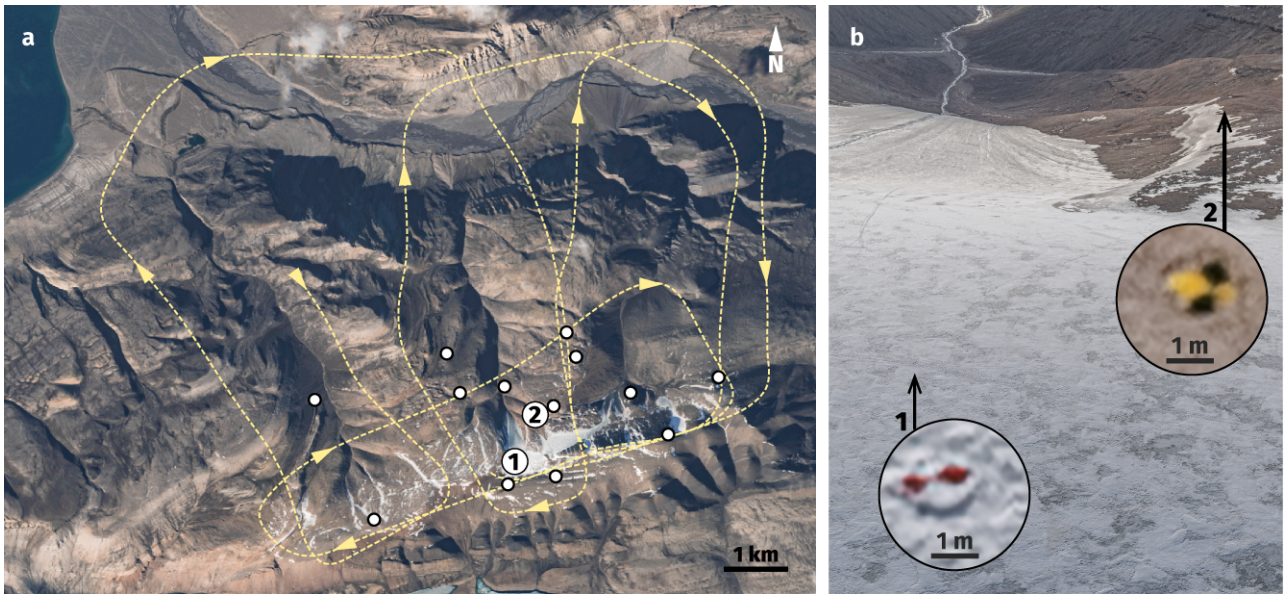

Figure 4.4. **[a]** Study area with flightpath of the 3 August 2018 air photo survey and locations of the two ground targets (numbered 1 and 2) used as checkpoints for the direct georeferencing method, and the 13 control points (white dots) used to align the 1959 and 2018 reconstructions. Base image: Sentinel 2B, 3 August 2018. **[b]** Image captured during the air photo survey (3 August 2018), with insets of surveyed targets (1×1 m checkered flags).

validating the direct georeferencing method. Throughout the survey, GPS observations were recorded at 15 second intervals. Synchronisation between the camera shutter and positioning system was achieved via the Trimble Event Input Marker, which connected the GPS receiver to the camera hot shoe accessory mount. Camera positions were subsequently calculated using interpolation based on the moment of image capture recorded by the GPS receiver. Additional details about the survey and optimisation of raw field data are described in Chapter 3.

Optimised image files and corresponding masks were imported into Metashape and used to generate a sparse point cloud, which was subsequently georeferenced using the camera position information assigned to each image. About 10% of tiepoints with the highest reprojection error values were removed and, following optimisation, RMS point reprojection errors were 0.41 pixels. Local RMS registration errors, based on the two checkpoints measured in the field, were 0.35 m horizontal and 0.68 m vertical (0.77 m total). The dense point cloud was generated in Metashape using the 'high' quality setting and the mild filtering option, in order to reduce processing time and remove some of the biggest outliers. Compared to the 6 million points in the sparse cloud, the final reconstruction contained 1.56 billion points.

Surface elevation change: 1959–2018

Point cloud data generated from image-based reconstruction techniques is inherently noisy, with outliers and geometrical errors arising from imperfections in the source data (e.g. noisy or out of focus images) or inadequate scene coverage. Filtering this surface noise and removing outliers helps to reduce artifacts and enable geometrically consistent surface reconstructions. In this study, filtering was performed using the Multiscale Model to Model Cloud Comparison (M3C2; Lague et al., 2013) plugin implemented in CloudCompare. Developed for direct cloud comparison and change detection, the M3C2 algorithm can also be used to filter point cloud data by computing local

statistics. The algorithm calculates the median height values of all points within a cylindrical neighbourhood of a given diameter and depth, oriented along a projected vector perpendicular to the surface (i.e. surface normal).

Filtering parameters in M3C2 were selected to take into account surface roughness and point density of the reconstructions, and to ensure a minimum of five points within each neighbourhood. For the 1959 point cloud, with a mean point spacing of ∼8.3 m and >99% of points being 10 m or less from their nearest neighbour, surface normals were computed over a scale of 100 m, the projection diameter was set at 20 m and maximum depth at 50 m. Given the mean point spacing, the final DEM and panchromatic orthomosaic were gridded at 8 m resolution, with each pixel representing the mean of all elevation or intensity values of all points within a given grid cell. For the 2018 point cloud, surface normals were then calculated at varying scales, between 2–10 m. Given a mean point spacing of ∼0.45 m in 2018, the projection scale was set at 1 m and the depth at 5 m. The smoothed point cloud was then gridded into DEM and RGB orthomosaic rasters at 0.5 m horizontal resolution (Fig. 4.5).

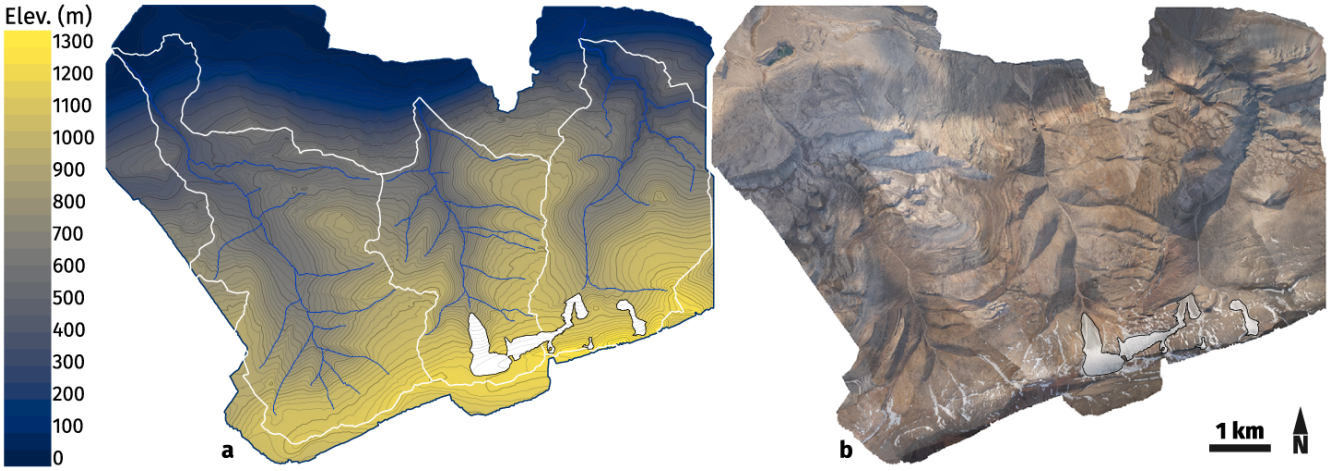

Figure 4.5. SfM-MVS workflow outputs from the 3 August 2018 air photo survey. **[a]** Elevation model of the study area including Bowman Glacier (white outline) and its drainage system with steam network (blue lines) and drainage basin boundaries (white lines). Elevation contours at 20 m. **[b]** RGB orthomosaic of the study area.

Following the filtering step, both the 1959 and 2018 point clouds were cropped to the same extent shown in figure 4.6, covering an area of 17 km^2 including Bowman Glacier and the summit plateau. Differences in ice surface elevation between 1959 and 2018 were then calculated by comparing the two point clouds in 3D using the M3C2 algorithm (Lague et al., 2013). As opposed to DEM differencing, performing change detection directly on point clouds allows the gridding step to be skipped, and therefore avoids the introduction of any additional uncertainties from interpolation of elevation values. Surface change was estimated from median point elevations calculated along the same surface normals computed on the 1959 cloud in the filtering step, while also keeping the same projection scale and maximum search depth (20 m and 50 m). Uncertainties were determined taking into account a 3 m registration error, corresponding to the vertical component of the misalignment errors calculated over the 13 control points used to align the two clouds. In combination with this 3 m error applied uniformly across the entire cloud, M3C2 uses local surface roughness characteristics computed at the projection scale to calculate a spatially variable level of detection at 95% confidence for each distance measurement, which can be used to determine the statistical significance of any detected change (Lague et al., 2013). The corresponding data were gridded into 8 m resolution rasters which were then used to calculate ice thickness and volume loss estimates.

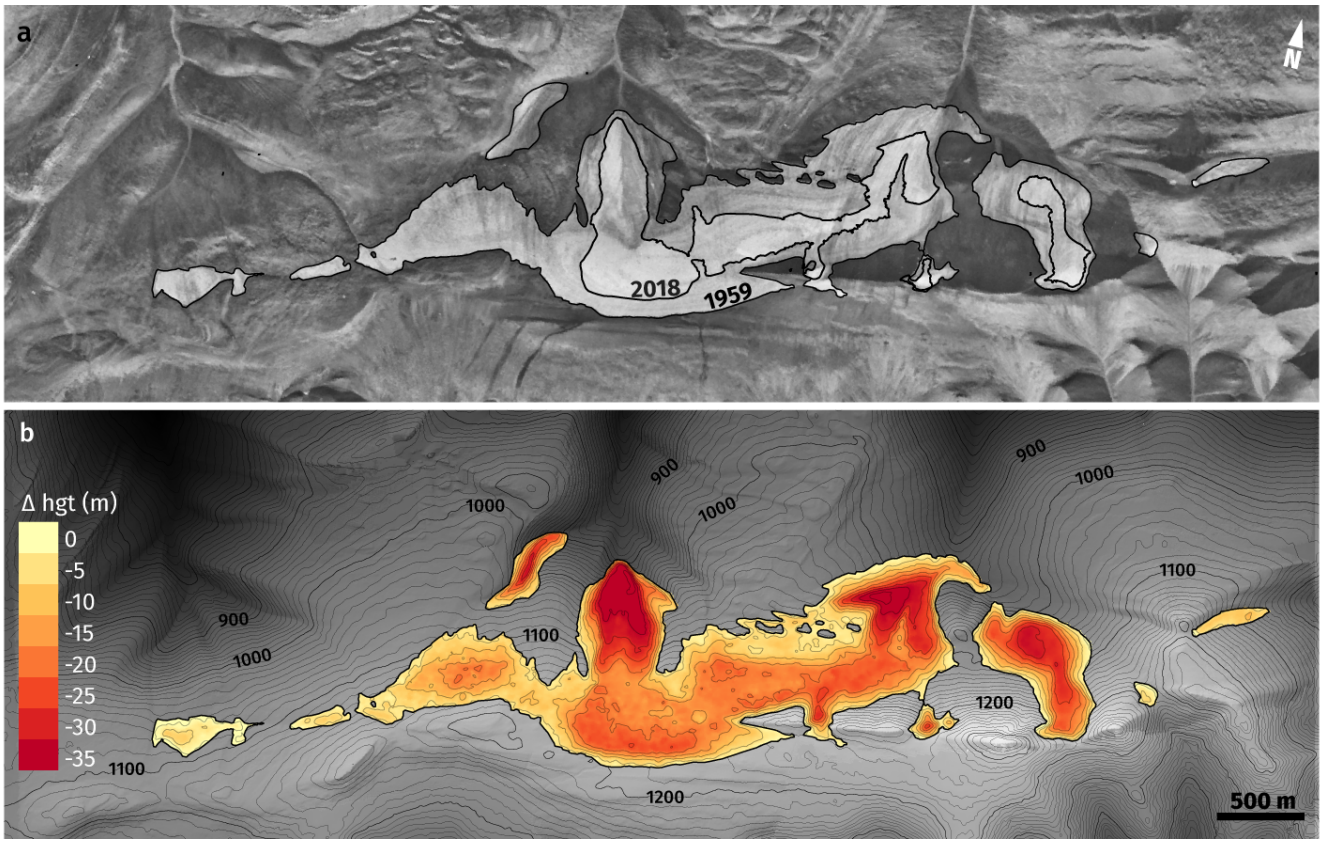

Figure 4.6. **[a]** Panchromatic orthomosaic of Bowman Glacier generated from the 1959 air photos, showing the 1959 and 2018 glacier extents (black outlines). **[b]** Ice surface elevation change between 1959–2018 from dense point cloud comparison. Elevation contours at 10 m over stable terrain, and 5 m over ice.

4.3.3 Ice thickness from GPR measurements

The current volume of Bowman Glacier was estimated from spot ice thickness measurements made with a 10 MHz ground penetrating radar (GPR) system on 3 August 2018. The system consists of a monopulse transmitter based on the design of Narod and Clarke (1994), and a TekTronix THS720A digital oscilloscope as the receiver, with images of the radar returns recorded with a digital camera. A handheld GPS unit was used for horizontal positioning, with an estimated accuracy of $<$10 m; the elevation of the measurement points was extracted from the 2018 SfM DEM. A total of 11 points, spaced $\sim$100 m apart, were measured along two transects, one running east-west across the top of the main ice mass, the other north-south along the centreline. A radio-wave velocity of 0.171 m ns^{-1} was used to convert GPR returns to true ice thickness, based on the mean of 12 common mid-point surveys undertaken by Copland and Sharp (2000) at John Evans Glacier, 200 km south of Bowman Glacier.

4.3.4 Surface mass balance

Surface mass balance (SMB) was derived from the regional climate model (RACMO) version 2.3 following the method detailed by Noël et al. (2018). To more accurately resolve complex topography and small isolated ice masses such as Bowman Glacier, daily SMB components (precipitation, melt, runoff, refreezing, sublimation, and drifting snow erosion) were downscaled from the original 11 km RACMO2.3 model output to 1 km resolution.

Elevation and albedo biases affecting surface melt and runoff components were corrected using DEM data, glacier outlines, and bare ice albedo information. Model results were evaluated and calibrated using field measurements from 1959–2010 from 198 sites across the northern CAA. Daily SMB estimates were obtained by summing the individual components and combined into monthly values spanning the 1958–2019 period. In this dataset, Bowman Glacier is represented by a single 1 km^2 pixel approximately centered over the main basin, and any changes in ice extent and glacier hypsometry due to mass loss over the study period are therefore not accounted for.

4.4 RESULTS

4.4.1 Ice extent and thickness change

Ice cover mapping from aerial photography and satellite imagery shows that Bowman Glacier shrank over the past six decades (Figs 4.3 and 4.7). In 1959, the glacier consisted of seven independent ice masses, of which three (including the main one) drained into May Creek. By 2000, the two westernmost ice masses had virtually disappeared, and only a small portion ($\sim$0.058 km^2) of the main glacier remained in the May Creek basin. By 2005 this remnant in May Creek had also disappeared, leaving glacier ice in only the central and eastern basins, which drain to Macdonald River and not to Tanquary camp. Over the past 61 years, the total ice covered area has decreased from 2.75 km^2 in 1959 to 0.61 km^2 in 2020, corresponding to a 78% area loss. In the 41 years between 1959–2000, total ice loss was 0.89 km^2, while in the period 2000–20 total loss was 1.26 km^2, meaning that average annual area loss nearly tripled between the two periods (0.022 km^2 a^{-1} vs 0.063 km^2 a^{-1}).

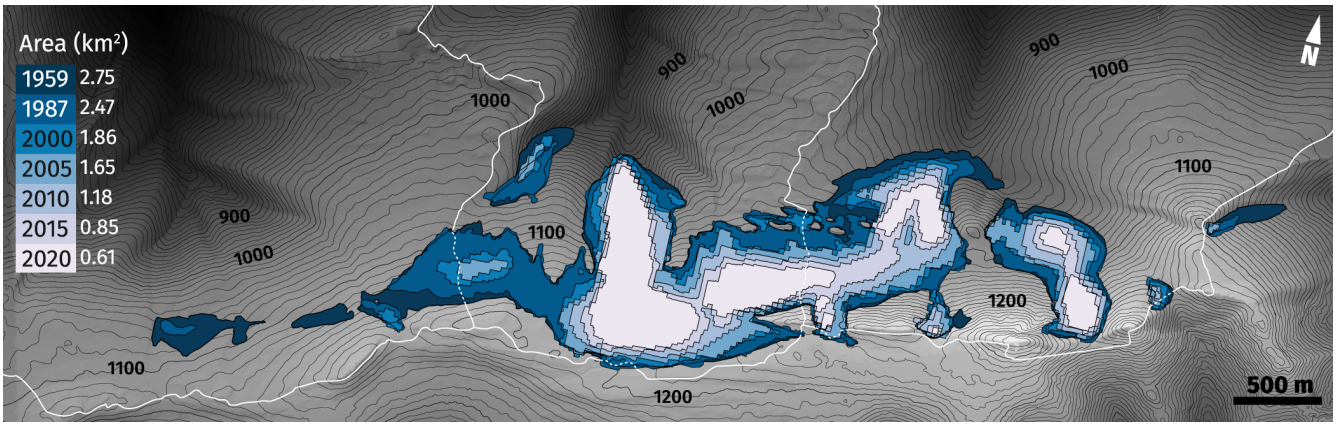

Figure 4.7. Evolution of ice extent of Bowman Glacier for 1959–2020. The white lines show the boundaries of the three drainage basins, with the western one providing the main water supply to Tanquary Camp. In 2000 a small remnant ice patch still drained into May Creek. By 2005 all the ice had retreated out of the western basin. Elevation contours at 10 m.

Results from differencing the 1959 and 2018 reconstructed ice surface show average elevation changes over the glacier of -14.7 m with a standard deviation (σ) of 9.2 m, and maximum losses reaching $>$40 m near the main terminus (Fig. 4.6b). Losses also reached over 30 m in the lower regions of the easternmost ice masses. Random error in the elevation change measurements is calculated from apparent change computed over an 11.35 km^2 area of stable ground adjacent to Bowman Glacier, including all pixels within a 1 km distance of the glacier limits. The average elevation difference over this whole area is -0.03 m, and the RMS error 2.8 m.

Figure 4.8 shows the hypsometry for 1959 and 2018 in 25 m elevation bands, as well as ice thickness and volume change for the same bands. In terms of ice cover, the largest losses occurred in the middle elevation bands of 1075–1125 m a.s.l., where <20% of the 1959 ice covered area remained in 2018. As most of the 1959 ice cover was concentrated above 1100 m, total volume losses are highest in those elevation bands. In comparison, surface lowering is highest between 1000–1050 m a.s.l., with average elevation losses reaching >20 m (Fig. 4.8).

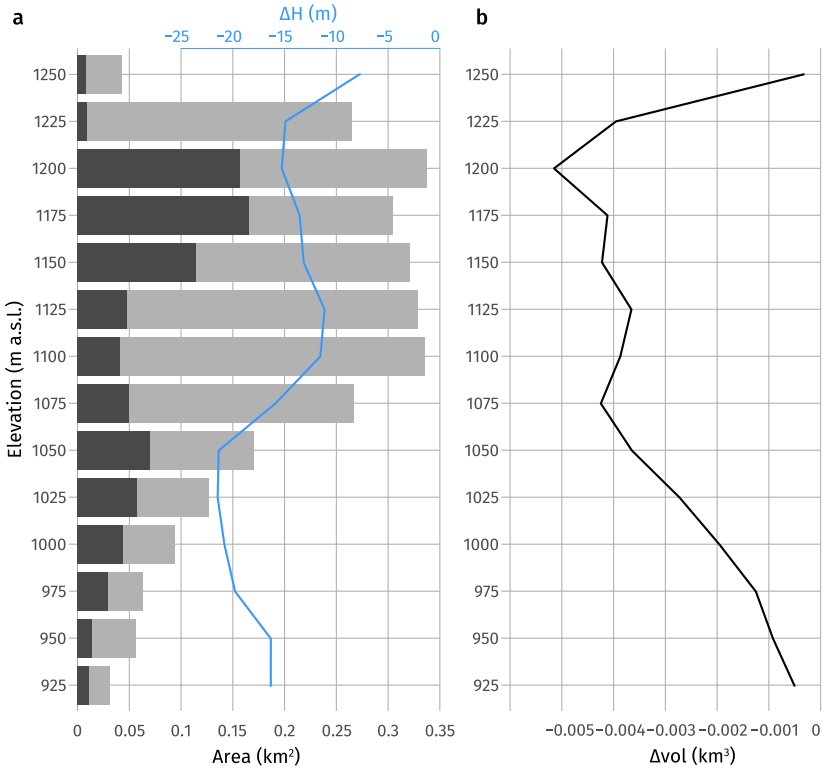

Figure 4.8. **[a]** Bowman Glacier hypsometry in 25 m elevation bands for 1959 (light grey bars) and 2018 (dark grey bars), and average ice surface elevation change (blue line) for the same bands. **[b]** Average ice volume loss for 1959–2018 per elevation band. Values on the vertical axis represent the midpoint elevation of each band.

Ice thickness measurements from 2018 GPR data average ∼25 m in the upper part of the basin (previously the accumulation area of the glacier), and ∼42 m in the lower part, with an overall average of 34.1 m. Comparison of the 1959 and 2018 ice surface elevations along the GPR transects suggests that the mean ice thickness in 1959 would have been 44 m in the upper part, and 65 m lower down, for an average of 55.5 m. This corresponds to an average ice surface elevation loss of 21.5 m, meaning that the mean ice depth remaining in 2018 was ∼60% of the 1959 thickness (Fig. 4.9).

4.4.2 Ice volume and mass loss

The 1959–2018 total ice volume loss over the full extent of the glacier, determined as the sum of the product of height differences for all pixels within the 1959 glacier extent and their corresponding area, is 0.041 ± 0.0083 km^3. The uncertainty term (± 0.0083 km^3) is based on 95% confidence interval calculated for each cloud-to-cloud distance measurement within the 1959 extent. Given the absence of snow cover on the ice surface on the 1959 air photos and in more recent satellite imagery from 2010–20, it is reasonable to assume that the full extent of Bowman Glacier lies in the ablation area, and consequently has no significant accumulation zone. We therefore convert volume to mass change assuming a constant density profile and using a conversion factor approaching ice density, of 900 kg

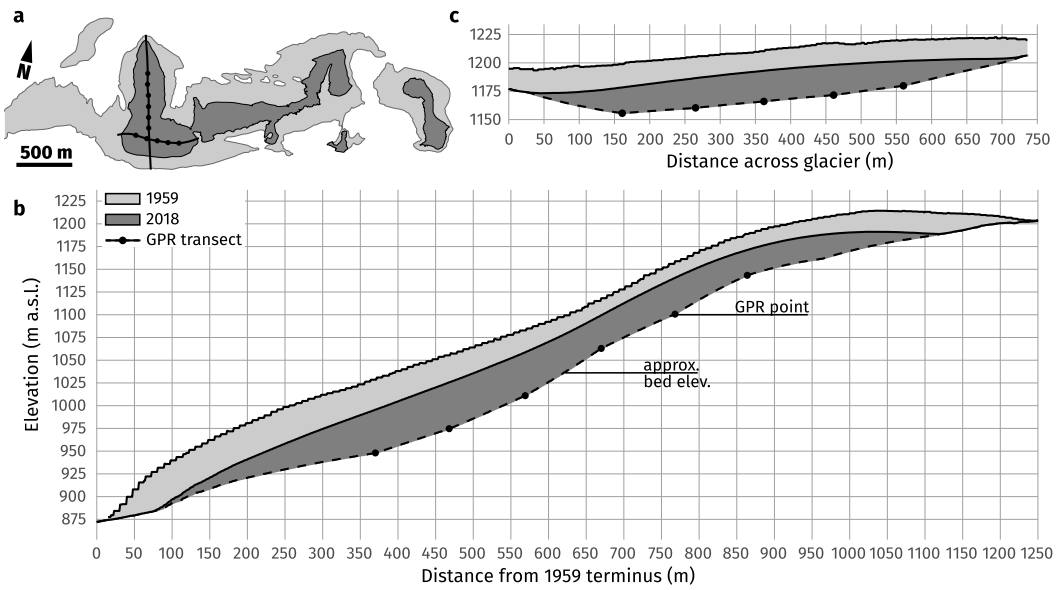

Figure 4.9. **[a]** Location of 11 ground penetrating radar (GPR) spot measurements performed along two transects on 3 August 2018. **[b, c]** Ice surface elevation change between 1959 (light grey) and 2018 (dark grey) along two GPR transects: north-south along the glacier centreline [b] , and east-west across the top of the main ice mass [c]. The black dashed line represents the approximate bed elevation along each transect interpolated between ice thickness measurements (black dots).

m^{-3} (Huss, 2013), and calculate a total loss of 0.036 ± 0.008 Gt. To compensate for glacier retreat over the 59 year period, we take the average ice area calculated for 1959 and 2018 (1.78 km^2) and determine a glacier-wide average thickness change of -22.7 ± 4.7 m. This corresponds to a total of -20.5 ± 4.2 m w.e., and an average of -347.0 ± 71.4 mm w.e. a^{-1} over the 1959–2018 period.

4.4.3 Surface mass balance

Modelled monthly surface mass balance data for 1958–2019 show a cumulative loss of 24.56 m w.e., with a noted increase in the rate of mass loss in the last two decades (Fig. 4.10). Average losses more than doubled between 1958–99 and 2000–19, increasing from 279 mm w.e. a^{-1} ($\sigma = 329$ mm w.e. a^{-1}) in the first period, to 642 mm w.e. a^{-1} ($\sigma = 401$ mm w.e. a^{-1}) in the second (Table 4.2). While most years have been negative, the frequency of positive net balance years decreased from an average of 2.5 per decade prior to 2000, to none since then, and four out of the five most negative years occurred in the last decade. With a few exceptions, there is overall little variability in winter balance over the study period ($\sigma = 40$ mm w.e. a^{-1}), with a fairly constant accumulation pattern and mean winter balance values decreasing slightly after 2000 ($\sim$20% decrease, from 142 to 117 mm w.e. a^{-1}). In contrast, there is a marked variability in summer balance ($\sigma = 365$ mm w.e. a^{-1}) associated with enhanced melt rates in warmer summers. Average summer losses increased from 422 mm w.e. a^{-1} in 1958–99 to 759 mm w.e. a^{-1} in 2000–19, corresponding to an $\sim$80% increase since the start of the 21st century (Fig. 4.10).

Decade	Net		Winter		Summer		Net		Winter		Summer	
	$\overline{x}$	σ	$\overline{x}$	σ	$\overline{x}$	σ	$\overline{x}$	σ	$\overline{x}$	σ	$\overline{x}$	σ
1960s	-394	404	134	37	-528	378						
1970s	-146	299	152	46	-298	270	-279	329	142	41	-422	301
1980s	-262	306	160	45	-422	270						
1990s	-291	272	126	35	-417	246						
2000s	-574	344	111	28	-685	327	-642	401	117	32	-759	388
2010s	-709	459	123	35	-832	446						
1958–2019	-396	390	134	40	-530	365						

Table 4.2. Net, winter, and summer surface mass balance for Bowman Glacier over the 1958–2019 period, derived from the regional climate model RACMO2.3. Decadal averages ($\overline{x}$) and standard deviation (σ) in units of mm w.e. a^{-1}.

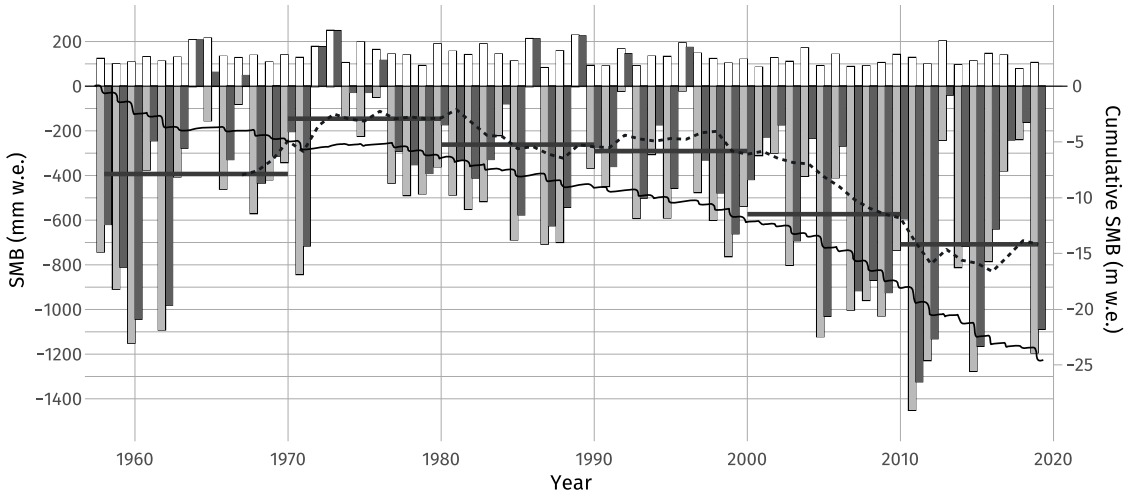

Figure 4.10. Winter (white), summer (light grey), and net annual (dark grey) surface mass balance (SMB) for 1958–2019, with ten year running mean (dotted line) and decadal averages (thick horizontal lines). Cumulative total SMB (solid line) is shown on secondary axis. SMB data derived from the regional climate model RACMO2.3 downscaled to 1 km resolution, and values determined over a 1 km^2 grid cell centred over Bowman Glacier.

4.5 DISCUSSION

Between 1959 and 2020 Bowman Glacier shrank by 2.15 km^2, losing 78% of its original extent, leaving it with an area of only 0.61 km^2. The majority of this loss, some 1.26 km^2, occurred in the last two decades, at a rate almost three times higher than before 2000. Overall, there are few studies on small ice masses in the northern CAA, although there are mass balance measurements from two pairs of small ice caps on the Hazen Plateau, the Murray and Simmons and St. Patrick Bay ice caps, 100–200 km east of Bowman Glacier (Bradley and Serreze, 1987; Braun et al., 2004; Serreze et al., 2017). In 2016, the four ice caps had lost between 61–95% of their 1959 extents (2.94–7.45 km^2). With the smaller of the two then only covering 0.15 km^2, Serreze et al. (2017) predicted that both St. Patrick Bay ice caps would be gone within five years; satellite imagery from 2020 indeed shows both glaciers have now completely disappeared. Using remote sensing data, Curley et al. (2021) reconstructed the evolution of eight land-terminating glaciers in Alexandra Fiord, 280 km south of Bowman Glacier on the east coast of Ellesmere Island, and found average annual area loss rates to have doubled between the 1959–2001 and 2001–19 periods. The smallest of the eight glaciers shrank by $\sim$50% since 1959 (from 1.81 km^2 to 0.88 km^2), compared to a total area loss of $\sim$12% over the same period when including all eight glaciers (of which seven were $>$5 km^2 in 2019).

On a regional scale, small ice masses have been experiencing the highest relative area losses, at least for the last six decades (Sharp et al., 2014; White and Copland, 2018). In the only recent assessment of regional changes in glacier ice extent over Northern Ellesmere Island, White and Copland (2018) found that, between 1999–2015, the rate of area change for small land-terminating glaciers <1 km^2 in size averaged -30.4% decade^{-1}, compared to -0.4% decade^{-1} for larger glaciers >1000 km^2. In comparison, between 1959/60 and 2000/01, ice masses <1 km^2 decreased in area by an average of 29.2% (7.3% decade^{-1}) and those in the size class above (1–5 km^2) by 25.6% (6.4% decade^{-1}) (Sharp et al., 2014). Averaged over the same periods, the rate of area change on Bowman Glacier increased from -7.9% decade^{-1} between 1959–2000 to -36.3% decade^{-1} between 2000–15, which is comparable to the regional average for ice masses in similar size classes (Sharp et al., 2014; White and Copland, 2018). Besides glacier size, White and Copland (2018) also identified elevation and glacier flow length as the main controls on area changes, with smaller and shorter glaciers at lower altitudes experiencing highest relative area losses. This is similar to findings from Alexandra Fiord where, among the eight studied glaciers, the two with the smallest elevation range, and with most of their area concentrated at lower elevations, lost the greatest proportion of their original extent, shrinking by $\sim$51% and $\sim$34% between 1959–2019 (Curley et al., 2021).

4.5.1 Thinning and mass loss

Our results for Bowman Glacier show a glacier-wide ice surface lowering of 22.7 ± 4.7 m between 1959 and 2018, giving average thinning rates of 0.39 ± 0.08 m a^{-1}. This is comparable to results from the only available regional assessment of ice thickness change in the northern CAA, where Hugonnet et al. (2021) reported average thinning rates on land-terminating glaciers of 0.39 ± 0.03 m a^{-1} for the 2000–19 period, including a 38% increase in the rate of change between 2000–04 and 2015–19. Although comparable, the surface lowering rates determined for Bowman Glacier are averaged over a considerably longer period (1959–2018), which includes a few years of positive mass balance in the 1960s to 1990s (Fig. 4.10). Considering only the last two decades, modelled SMB on Bowman Glacier shows average surface lowering of 0.71 m a^{-1}, and a 90% increase in rate of thinning between 2000–04 and 2015–19, meaning that both overall annual losses and interannual thinning rates are greater than the regional average for land-terminating glaciers determined in Hugonnet et al. (2021).

Differencing the 1959 and 2018 reconstructed surfaces for Bowman Glacier yields a total volume loss of 0.036 ± 0.008 Gt, and a glacier-wide average elevation change of -20.5 ± 4.2 m w.e., at a mean specific rate of -347.0 ± 71.4 mm w.e. a^{-1}. In comparison, modelling results from RACMO2.3 averaged over the same period (September 1959 to July 2018 inclusively) show a net SMB of -22.0 m w.e. and a mean specific rate of -372.8 mm w.e. a^{-1}, equating to a 7.4% difference from our estimates, well within the error margin. Total volume losses for the 1 km RACMO grid cell sum to 0.022 Gt. When scaled to the mean area of Bowman Glacier of 1.78 km^2, this amounts to 0.039 Gt, which is in close agreement with the 0.036 ± 0.008 Gt total mass loss determined from differencing the 1959 and 2018 point clouds.

The reconstructed hypsometry at Bowman Glacier for 1959 and 2018 shows net area losses and ice surface lowering at all elevations (Fig. 4.8). Geodetic mass balance measurements for 1960–2014 at White Glacier, a 14 km long valley glacier on western Axel Heiberg Island, 340 km south-west of Bowman Glacier, show overall thinning at elevations below 1400 m a.s.l., with maximum losses of around 40 m near the terminus (Thomson et al., 2017).

Between 900–1300 m a.s.l., roughly the elevation range of Bowman Glacier, ice thickness losses at White Glacier ranged between 10 m and 23 m over the period 1960–2014, which is comparable to the thinning values computed for the equivalent elevation bands at Bowman Glacier of 13 to 21 m (Fig. 4.8).

At White Glacier, the mean geodetic mass balance for 1960–2014 averaged over a glaciated area of 39.81 km^2 is -9.61 m w.e., or -178 ± 16 mm w.e. a^{-1} (Thomson et al., 2017), about half the losses determined at Bowman Glacier in this study. There are notable differences between the two glaciers, including their length, elevation span, and the fact that, unlike Bowman Glacier, White Glacier still has an accumulation area which offsets some of the ice loss observed at lower elevations. Bowman Glacier now measures <1 km along its main axis, covers an elevation range of only 350 m (between 900–1250 m a.s.l.), and is entirely in the ablation area. In contrast, White Glacier is 14 km long and spans an elevation range of 1700 m, with the terminus descending to nearly sea level and a 5 km wide accumulation area reaching 1780 m a.s.l. (Thomson et al., 2017).

4.5.2 Connections between mass loss, hypsometry, and regional equilibrium line altitude

Aerial photos from late August 1959 (Figs 4.3a and 4.6a) show bare ice over the entire extent of Bowman Glacier, with the snowline only visible on the much larger ice cap 2 km to the south, at an altitude of $\sim$1250 m. Regional reconstructions of the lowest equilibrium line altitude (ELA) over the northern CAA in 1960 show it reaching 1200 m over the Northern Ellesmere Icefields to the north of Tanquary Fiord, and 1000–1100 m over the Hazen Plateau to the east (Miller et al., 1975; Wolken et al., 2008), which would place the summit of Bowman Glacier either at the limit, or just below, the local ELA at that time.

With the exception of a period of cooler conditions in the 1970s, a number of studies point to a general increase in ELA since the 1960s across the northern CAA. For example, on the eight glaciers in Alexandra Fiord, the mean end of summer snowline elevation (assumed to represent the ELA) increased by 77 m between 1974–82 and 2014–19 (Curley et al., 2021). Field measurements at White Glacier and on Meighen, Agassiz, and Devon ice caps, show the average decadal ELA to have increased by $\sim$330 m between the 1980s and 2010s (Thomson et al., 2017; Burgess and Danielson, 2022). White and Copland (2018) demonstrated the impact of rising ELA on the ice masses of northern Ellesmere Island and showed that a 100 m rise above the 1960 regional ELA would cause the ratio of ice in the ablation zone to increase from 35.2% to 47.1%. For a 300 m rise, the ratio would increase to 72.3% and $>$50% of all glaciers in the region would be entirely below the ELA (White and Copland, 2018). Glaciers at relatively low elevations, and those in areas with relatively flat topography with the bulk of ice within a narrow elevation band (e.g. small glaciers on plateaus, such as Bowman Glacier), are particularly sensitive to changes in regional climate, particularly when the ELA rises above their summit elevation. For example, of the four small ice caps on the Hazen Plateau, the two that recently disappeared were located 200–300 m lower in elevation than the nearby Murray and Simmons ice caps, which still survive (Bradley and Serreze, 1987; Braun et al., 2004; Serreze et al., 2017). However, similar to Bowman Glacier, the Murray and Simmons ice caps were already at the limit of the local ELA estimated at 1000–1100 m a.s.l. in 1960 (Miller et al., 1975; Wolken et al., 2008), and so their loss is inevitable under the current climate. The rapid shrinkage of small glaciers at lower altitudes in the study region (Sharp et al., 2014; Serreze et al., 2017; White and Copland, 2018) highlights the importance of glacier hypsometry in connection to regional ELA, and its role in determining mass balance sensitivity to changes in climatic conditions.

Melt rates are expected to increase in the following decades due to continued warming and lengthening of the melt season (IPCC, 2022). Albedo feedback processes will enhance these losses, particularly on small glaciers, due to the exposure of dirt layers and darkening of the ice surface and to increased heat advection from exposure of surrounding bedrock as the ice cover shrinks (Sharp et al., 2011; Serreze et al., 2017). Models predict rising surface air temperatures accompanied by increased mean precipitation, but with a higher fraction falling as rain (IPCC, 2022), this also contributes to ablation and lowers albedo.

4.5.3 Changes in regional climate

The regional climate in the northern CAA is characterised by relatively low annual precipitation (<400 mm a^{-1}), with some variability depending on the combined effect of topography and distance to a moisture source (Koerner, 1979). Precipitation is highest along coastlines facing Baffin Bay and the Arctic Ocean, and decreases with elevation and distance inland. These precipitation gradients in part explain the difference in local ELA between Alexandra Fiord (∼670 m a.s.l.), White Glacier (∼1075 m a.s.l.), and Bowman Glacier (∼1200 m a.s.l.). The 1950–2020 instrumental record at the two nearest weather stations, Eureka and Alert, 200 km southwest and 250 km northeast of Bowman Glacier, respectively, shows average annual air temperatures of −18.9ºC and −17.4ºC, and mean total annual precipitation of 72 mm and 156 mm. Both stations recorded an average warming of >1.5ºC between 1950–99 and 2000–20 (Fig. 4.11a), with winter and autumn temperatures showing the largest increase (>2ºC) between the two periods (Fig. 4.12b).

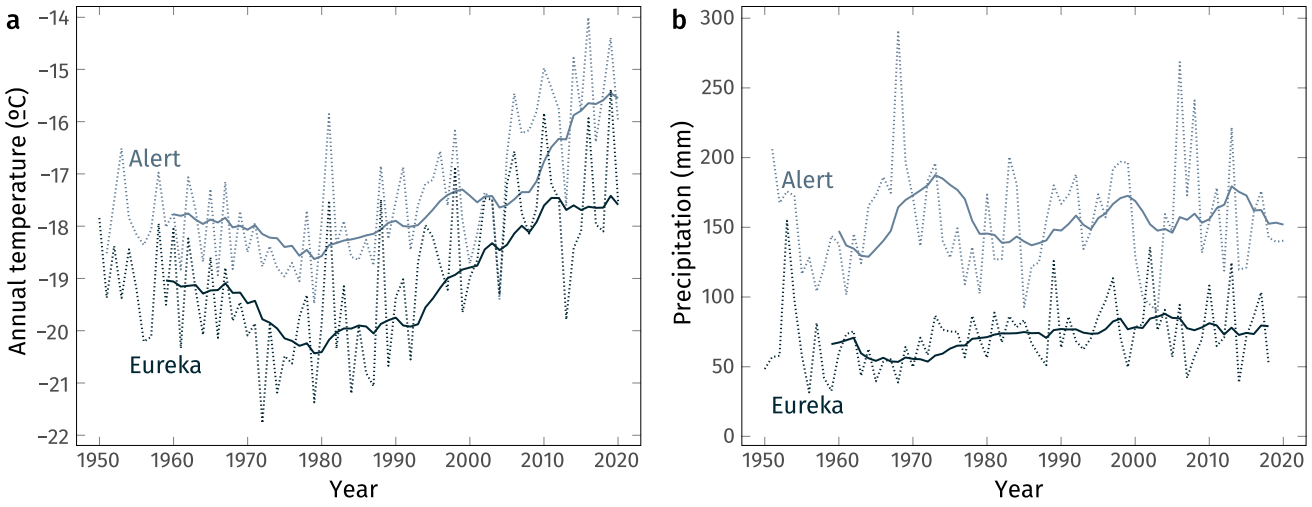

Figure 4.11. **[a]** Mean annual air temperature and **[b]** total annual precipitation for Eureka (black) and Alert (grey) weather stations. Annual values (dotted lines) and ten year running mean (solid lines) for 1950–2020. Source: https://climatedata.ca.

The annual mass balance of glaciers and ice caps in the CAA mainly depends on summer melt rates rather than any changes in winter accumulation (Koerner, 2005), and the accelerated mass loss in the last two decades has been shown to coincide with an increase in summer (June, July, August) air temperatures (Sharp et al., 2011; Mortimer et al., 2016). At Bowman Glacier, there is a strong positive correlation (R^2=0.99, p-value=2.22×10^{-16}) between yearly summer losses and net balance, indicating that the increasingly negative mass budget is in direct response to enhanced summer melt due to warmer summer temperatures. At Eureka, total annual precipitation increased by

$\sim$30% since 1950 ($\sim$4% decade^{-1}), but there is no significant trend in the precipitation record at Alert (Fig. 4.11b). However, there is little interannual variability in winter mass balance over Bowman Glacier (Fig. 4.10), suggesting that any potential increase in total precipitation is not enough to offset losses from warming temperatures.

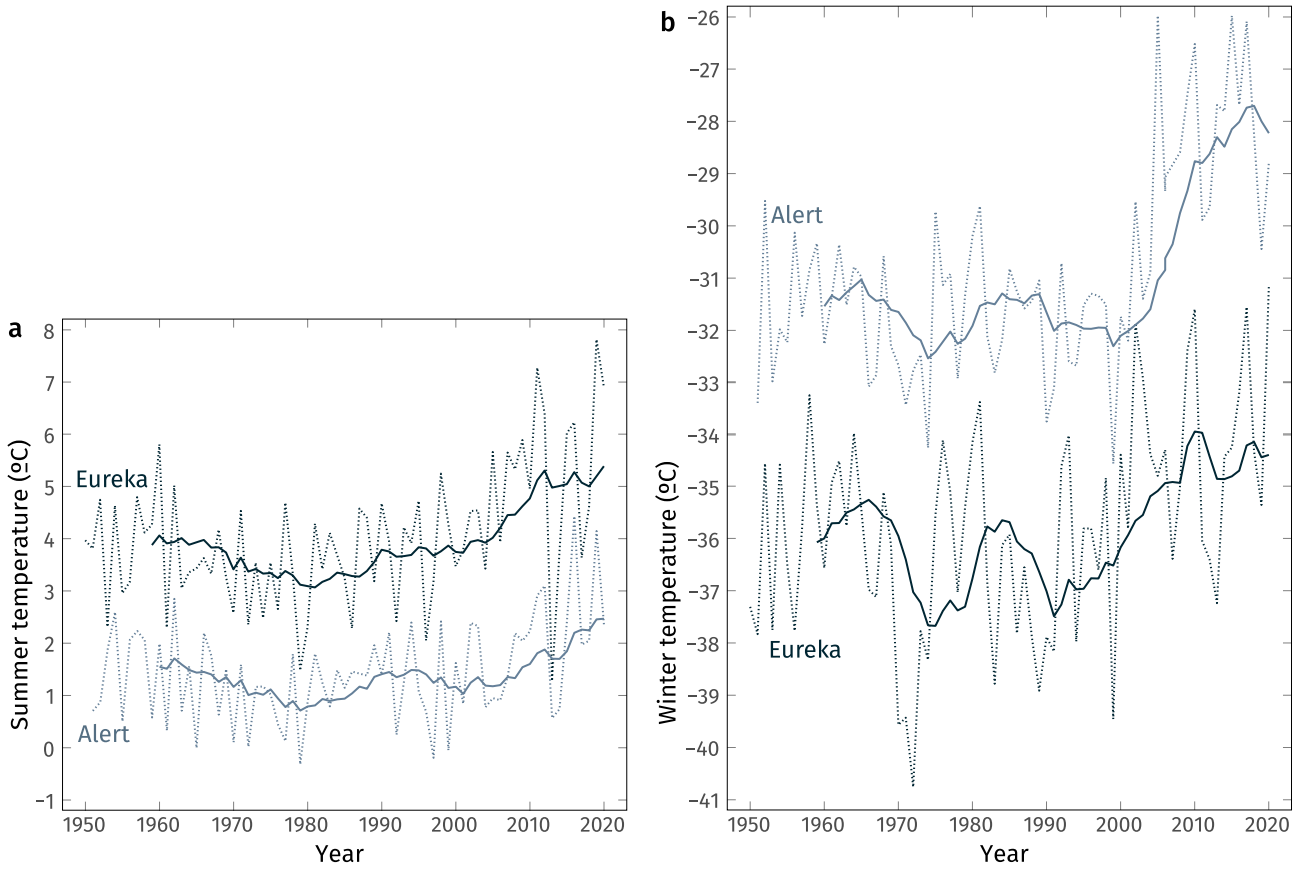

Figure 4.12. **[a]** Mean summer and **[b]** winter air temperature for Eureka (black) and Alert (grey) weather stations. Annual values (dotted lines) and ten year running mean (solid lines) for 1950–2020. Source: https://climatedata.ca.

4.5.4 Future projections

Given that Bowman Glacier has lost nearly 80% of its area over the past 60 years, and that the entire glacier now sits within the ablation zone, the ice mass is expected to completely disappear over the coming decades. The predicted timing of its demise varies depending on the parameter used as a basis for the calculations, namely:

1. Volume-area scaling: taking the 2018 glacier area (0.82 km^2) and the average measured ice thickness along the two GPR transects (34.1 m), gives a total remaining ice volume of 0.028 km^3, or 0.025 Gt. Based on our estimates, the glacier lost 0.041 $\pm$ 0.008 km^3, or around 60% of its volume since 1959. Projecting the average rate of volume change determined for 1959–2018 ($-$0.0069 km^3 decade^{-1}) into the future suggests that the glacier will completely disappear in just under four decades, by $\sim$2060.
2. Surface mass balance: from the modelled SMB data, the average thinning rate for the last decade was 709.2 mm w.e. a^{-1}. Taking the average ice thickness measured in 2018 (34.1 m of ice, 30.69 m w.e.), and assuming that this rate continues into the future, suggests that the disappearance might occur by $\sim$2060.

3. Area change: in 2020, the last year of our study period, Bowman Glacier covered only 0.61 km^2. Projecting the average rate of change in ice extent from the last decade (-0.057 km^2 a^{-1}) beyond 2020, suggests Bowman Glacier will have completely disappeared by ∼2030 (Fig. 4.13).

The above projections likely bound the lower and upper limits for the complete disappearance of Bowman Glacier, sometime between 2030–60, provided that regional warming trends remain similar in the future. However, given that the most recent Intergovernmental Panel on Climate Change (IPCC, 2022) projections suggest that an increase in the rate of Arctic warming is plausible, Bowman Glacier might not even survive that long.

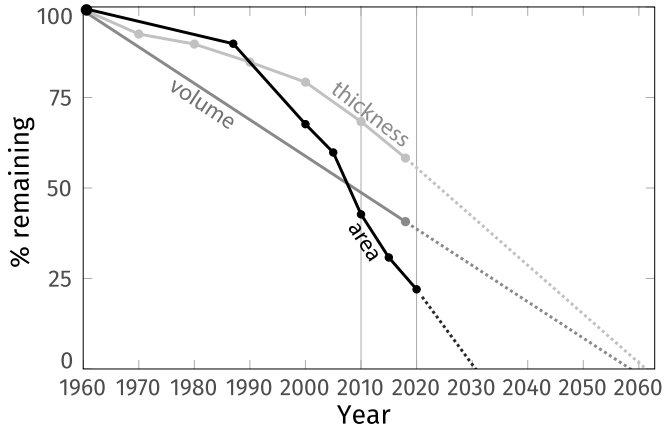

Figure 4.13. Change in ice extent (black), volume (dark grey), and average thickness (light grey) of Bowman Glacier for 1959–2020 (solid lines) and projected rate of change (dotted lines), represented as remaining percentage in reference to 1959. Volume projections are based on the 1959–2018 average, while area and thickness change are based on the 2010–20 trend.

4.5.5 Hydrological implications

The reduction in extent of Bowman Glacier has had a direct impact on the water supply for the Parks Canada basecamp at Tanquary Fiord. Aerial photography and satellite imagery show the presence of glacier ice in the western drainage basin, which drains into May Creek and provides meltwater to the camp, up until about 2005 (Figs 4.3 and 4.7). Since then, streamflow in May Creek has been mainly fed by snowmelt together with active layer and permafrost thaw. Satellite imagery since 2000 shows that in some summers (e.g., 2011, 2015, 2020), both the glacier surface and its three drainage basins become entirely free of snow (Fig. 4.3). In other years, including at the time of the air photo survey in 2018, seasonal snow patches persisted throughout the melt season, particularly in narrow depressions at higher elevations where drifting snow tends to accumulate.

In glacierized catchments surface hydrology is modulated by water storage within the glacier system which acts as a buffer, delaying peak seasonal runoff and contributing to streamflow throughout the melt season. Since the loss of glacier ice, the flow regime in May Creek has become dominated by snowmelt, which typically means a shift in the timing of peak discharge, shorter duration of high meltwater input, and increased interannual variability in total runoff. With maximum runoff occurring over a shorter timespan earlier in the melt season than before, the rest of the summer is likely to see diminished streamflow and increased influence of rainfall events (Fountain and Tangborn, 1985). May Creek may therefore not remain a reliable source of freshwater for Tanquary Camp in the future. A higher relative contribution of melting ground ice from permafrost degradation is in turn likely to result in more turbid streamflow due to higher sediment, particulate, and solute content (IPCC, 2022).

4.6 CONCLUSION

In this study, SfM-MVS photogrammetry techniques were applied to historical aerial photography from 1959 to create a detailed reconstruction of the surface topography of Bowman Glacier. This enabled direct cloud-to-cloud comparison with recent reconstructions of the glacier generated from aerial photographs acquired in 2018, and calculation of ice surface elevation change and geodetic mass balance spanning six decades. To our knowledge, this study is the first to use historical aerial photography in this way in the Canadian Arctic, allowing for an important gap to be filled concerning changes in glacier surface elevation prior to the satellite record. Although demonstrated here on a single small glacier, the same method can be applied to significantly larger ice masses and on a regional scale.

Over the last six decades, Bowman Glacier lost most of its area ($\sim$78% loss between 1959–2020) and volume ($\sim$60% loss between 1959–2018). In 2018, the glacier occupied an area of 0.82 km^2 and had an average ice thickness of 34.1 m. Projecting the rates of change in ice extent and surface mass balance observed over the last decade suggests that the glacier will disappear entirely between 2030 and 2060, or perhaps even sooner. This highlights the importance of ice thickness and volume datasets for documenting past glacier fluctuations and for predicting future changes on a regional basis in the CAA.

Modelling results show the interannual mass balance variability to be dominated by summer balance, meaning that the primary driver for the rapid demise of Bowman Glacier is sensitivity to increased summer melt due to warmer air temperatures, rather than changes in winter accumulation. Given projections of continued warming across the Arctic, the ongoing trend of rising ELAs is expected to continue, expanding the ablation area of glaciers in the region and leading to increased mass loss. Small ice masses at lower elevations covering narrow elevation spans are particularly sensitive, as even slight changes in ELA can shift entire glaciers into the ablation zone. Those glaciers are clearly out of equilibrium with current climate and, similar to Bowman Glacier, are destined to disappear in the future.

5

Conclusion

This thesis presents detailed reconstructions of the long-term response (since the 1950s) of two individual glacier systems with opposing behaviours: Good Friday Glacier, a large marine-terminating outlet on western Axel Heiberg Island, and Bowman Glacier, a small mountain glacier on northern Ellesmere Island. This work demonstrates the potential of digital photogrammetry techniques for deriving high-resolution topographic reconstructions from both recent and historical aerial photography, enabling change detection and calculation of geodetic mass balance over decadal timescales.

5.1 SUMMARY

Observations on Good Friday Glacier show a continuous advance of 9 km over the last seven decades, corresponding to a 5% increase in ice cover compared to a total basin size of 800 km^2. The evolution of flow rates and glacier geometry patterns throughout the advance underlines the role of small-scale bedrock features at the glacier front, including topographic highs and overdeepenings, in modulating spatial patterns of ice motion in the terminus region. However, variations in basal topography at the terminus cannot explain the sustained mass flux and resulting long-term advance in the present climate. Possible explanations involve a delayed response to past positive mass balance conditions, or a dynamic instability such as surging. With no convincing evidence of periodic oscillations in flow regimes characteristic of surging, and without long-term observations of ice surface elevation change able to detect rapid and/or irregular mass redistribution patterns indicative of ice flow instabilities, there is insufficient evidence to determine whether the behaviour of Good Friday Glacier deviates from steady-state flow conditions.

This thesis demonstrates the potential of aerial photography surveys and computer-based photogrammetry processing for the acquisition of topographic data over individual ice masses in the NCAA without the requirement of ground control points. The full workflow, from data acquisition in the field to the structure from motion (SfM) and multiview stereo (MVS) processing is presented using two case studies. Air photo surveys were conducted on Bowman Glacier (August 2018) and Adams Icefield (July 2019), two field sites representative of some of the challenging conditions often encountered when surveying glaciers and ice caps in remote arctic locations. With a focus on optimising the quantity and quality of source data, and the reliability of final outputs, this work provides recommendations on hardware selection and flexible survey design, and outlines steps for enhancing raw image

data and calculating camera positions from positioning measurements. Results include centimetre resolution digital elevation models and orthomosaics of Adams Icefield, Bowman Glacier, and surrounding areas, with a maximum 3D accuracy estimate of <1 m.

Similar to other small ice masses in the region, Bowman Glacier is currently undergoing rapid mass loss. Since 1959, the glacier lost 78% of its area and 60% of its volume, and currently covers only 0.61 km^2. All of Bowman Glacier has been below the local ELA for most of the last six decades, and is destined to eventually disappear even if current climatic conditions stabilise. Projecting the trend in ice extent and surface thinning observed over the last decade indicates that Bowman Glacier will likely disappear entirely sometime between 2030–60. This study demonstrates the first use of SfM-MVS processing techniques for deriving elevation products from historical aerial photographs of a glacier in the NCAA. Direct comparison of topographic reconstructions from 1959 and 2018 (derived from the 2018 air photo survey of Bowman Glacier detailed in Chapter 3), enabled determination of ice volume change and geodetic mass balance over a 60-year period.

5.2 CONTRIBUTIONS & LIMITATIONS

This thesis highlights an important knowledge gap in terms of ice volume change and geodetic mass balance in the CAA, primarily due to limited observations of ice surface elevation, particularly before the start of the satellite record. Data on ice extent and glacier length is more readily available, but fluctuations in terminus position represent only part of a glacier's response to changes in climate. Terminus advance/retreat itself is a consequence of changes in ice flux due to thickening/thinning, and mass (re)distribution patterns along the glacier profile. A sufficiently long dataset of ice thickness change spanning multiple decades is crucial for monitoring the evolution of glacier hypsometry and detecting trends in geodetic mass balance in response to changes in climate. Reconstruction of the 1959 surface topography of Bowman Glacier using SfM-MVS techniques shows the potential of extracting elevation information from an extensive collection of historical aerial photography acquired over the Canadian Arctic since the 1950s, now (mainly) archived at the National Air Photo Library, Ottawa. The dataset, however, contains photographs of variable quality which may limit the use of the technique, especially over accumulation areas and the top of ice caps where the brightness of the snowpack causes some of the photos to be overexposed, and there are few distinctive features to match. Additional issues with the quality of the prints and the scanning process can introduce artefacts (e.g., banding, noise). Despite such limitations, the SfM-MVS workflow developed here creates the potential to extend observations of ice elevation and glacier volume change by several decades earlier than at present, and to better constrain the long-term geodetic mass balance of individual glaciers and, eventually, at a regional scale.

Ice surface elevation data are also required for determining the drivers of temporal and spatial variability in ice motion, specifically thinning/thickening patterns related to changes in flow regimes and unstable behaviour. Data gaps and the limited timespan covered by currently available records, combined with the relatively long response time (and long surge cycles) of large outlets and ice caps in the NCAA, introduces an observational bias and poses a challenge for understanding current trends of glacier change in a longer-term context. This is one of the limiting factors for interpreting the asynchronous behaviour of Good Friday Glacier and other seemingly unstable glacier responses. The techniques presented in this thesis provide a method to monitor rapid changes in glacier geometry

related to dynamic instabilities using SfM-MVS processing, and to determine high-resolution topographic data from repeat aerial photo surveys conducted over individual glaciers. The accessibility and flexibility of the technique makes it suitable for a wide range of applications, and data acquisition can be adapted to fit the specific requirements of different studies. With an understanding of the various sources and effects of measurement errors, and careful consideration of the factors most likely to degrade source data quality, efforts can be made to minimise the impact of adverse field conditions on the accuracy of the final product. The two case studies of Adams Icefield and Bowman Glacier illustrate the potential of deriving centimetre resolution topographic data of sufficient quality and accuracy to enable change detection. Coupled with systematic measurements of ice surface velocities, detailed topographic reconstructions derived from successive surveys would enable process-based studies on the mechanisms driving rapid changes and unstable flow behaviour on individual glaciers. This would provide an improved understanding of the periodic oscillations in flow regimes attributed to surging, and the pulse-type events related to calving dynamics.

5.3 SYNTHESIS

Interannual variations in glacier mass balance occur in direct response to seasonal climatic conditions in a given year, but more time is required for a glacier to adjust its geometry. Glacier response time, defined as the lag between an initial perturbation and a glacier reaching a new equilibrium, is a useful theoretical concept for providing a rough estimate of the timescales over which different glaciers are expected to adjust their geometry to a shift in mass balance (Bahr et al., 1998; Oerlemans et al., 1998; Raper and Braithwaite, 2009). In reality, however, climate is changing continuously, and evolving glacier dynamics additionally modify hypsometry and mass balance patterns through a series of feedback mechanisms. Therefore, glaciers with long response times can lag far behind and be significantly out of equilibrium with current climatic conditions. This implies that, at any given time, individual glaciers might be responding to a previous climate (Marzeion et al., 2014b; Christian et al., 2018; Roe et al., 2021).

Volume scaling gives an approximation of response time based on the ratio of ice thickness to ablation at the terminus (Jóhannesson et al., 1989). Taking Good Friday Glacier, for example, with a maximum ice thickness of $\sim$500 m (Chapter 2) and average ablation rates for 1996–2015 of nearly 2 m a^{-1} at the terminus (Noël, 2017), the theoretical response time based on present-day conditions is around 250 years. With response times on the order of centuries, observational records spanning a few decades may be dominated by short-term fluctuations and consequently be insufficient to properly resolve long-term trends. Based on partial information, a glacier can therefore be incorrectly assumed to be retreating, while the overall response is one of terminus advance, and vice versa (Roe et al., 2017). Assuming that the warming trend in the NCAA started around 1900, at the end of the Little Ice Age (Koerner, 1977, 2005; Dowdeswell, 1995), the asynchronous behaviour of Good Friday Glacier may indeed be related to a previous climate. In this perspective, it might be appropriate to reconsider the ongoing advance of Airdrop Glacier on western Axel Heiberg Island (Van Wychen et al., 2021), and until recently nearby Thompson Glacier (Cogley et al., 2011), as part of a response to centennial scale climate variations, rather than the result of surging behaviour as previously suggested (Copland et al., 2003; Van Wychen et al., 2016, 2021). Glaciers identified as surging are typically considered as being decoupled from climate, but, if misclassified, excluding them from the regular glacier

population can significantly skew regional assessments of glacier change (Thomson et al., 2011). Especially given the accelerated warming of the Arctic, once the few advancing glaciers reverse direction and start retreating, omitting their contribution will underestimate regional mass loss and influence projections of future change.

At the other end of the spectrum are small glaciers with characteristic response times on the order of a few decades or less. There, the lag is significantly shorter, and the overwhelming trend is one of sustained mass loss with an increase in recent decades in direct response to warming air temperatures. Small glaciers and ice caps remain underrepresented in many glacier inventories, but given their widespread distribution and large numbers, omitting their contribution can significantly underestimate regional and global assessments of glacier mass loss and equivalent potential sea level rise (Bahr and Radić, 2012; Parkes and Marzeion, 2018). Glaciers where the accumulation area is small and/or covers a narrow elevation range tend to respond quickly to a relatively small rise in ELA, particularly once it migrates above the summit elevation. Once ice extent decreases below a certain size, glaciers tend to decouple from atmospheric forcing due to the increased influence of local topographic factors (e.g., slope and aspect). In the case of Bowman Glacier, increased albedo from darkening of the ice surface and from longwave radiation from surrounding ice-free terrain is expected to enhance mass loss (Hock, 2005; Noël et al., 2018). In other cases, for example where glaciers retreat to higher elevation in mountainous terrain, the shading effect from adjacent slopes will rather slow surface melt and extend the lifespan of the smallest ice masses (Hock, 2005). Thus, the most sensitive glaciers currently undergoing rapid change may not have the largest impact on long-term regional mass budget, partly because some will disappear entirely, while others will retreat to higher elevations where they might temporarily stabilise. Identifying the factors responsible for the different sensitivities and response times of individual glacier systems would provide an improved understanding of the regional mass balance rate sensitivity to a given vertical shift in ELA.

5.4 OUTLOOK

While the changes on Bowman Glacier are in agreement with the dominant regional trend of accelerated mass loss and glacier retreat, the ongoing advance of Good Friday Glacier is clearly out of sync with most other glaciers in the NCAA. Both glaciers are out of balance with current climate, but their response is occurring at very different timescales. Still, the widespread retreat of glaciers with different response times (very short and very long) indicates that these changes are related to a common environmental forcing. With arctic warming surpassing the global average over the 21st century (IPCC, 2022), arctic glaciers and ice caps have experienced a rapid increase in mass loss, with some of the largest changes occurring in the NCAA (Hugonnet et al., 2021). While total precipitation is expected to increase in a warming climate, with a larger fraction falling as rain instead of snow, this will do little to offset any increase in mass loss from warming (Marzeion et al., 2014b; IPCC, 2022). These glaciers are expected to be among the largest contributors to global sea level rise for the 21st century (Lenaerts et al., 2013; Hock et al., 2019; Zemp et al., 2019).

The variability in ice motion observed in the CAA, with sometimes neighbouring glacier systems exhibiting contrasting behaviours, can be attributed to a number of related factors, including hypsometry and mass balance gradient which determine glacier response time, and various dynamic processes related to calving, surging, or other instabilities. Accounting for the variable response of different ice masses is crucial for accurate regional assess-

ments of past glacier change. Because of the delayed response of glaciers and ice caps to climate forcing, and the added effects of mass balance elevation feedbacks, reconstructions of ice extent and glacier length are insufficient to properly resolve changes in glacier geometry. Long-term observations of ice surface elevation therefore remain crucial for deriving ice volume and geodetic mass balance estimates, and for quantifying past glacier change over multi-decadal timescales. This is all the more important given that our understanding of the variability in dynamics exhibited by some of the largest outlet glaciers of the NCAA remains incomplete (Van Wychen et al., 2016, 2021). It is unclear which behaviours are a direct response to climate (past or present), and to what extent that response is affected by particular topographic, hypsometric, or geometric factors. The uncertainties related to dynamic instabilities, whether surging, pulsing, or calving dynamics, and whether a certain behaviour is cyclic in nature, make differentiating between stable and unstable behaviours not always straightforward. This complicates any attempt to identify the factors and mechanisms causing some glaciers to behave out of sync with other ice masses in the region, and limits our understanding how glacier dynamics might evolve given current projections of continued mass loss.

The unprecedented mass loss of glaciers and ice caps on a global scale has been linked to current anthropogenic forcing (Marzeion et al., 2014a; Zemp et al., 2015; Roe et al., 2017, 2021). Regardless of the emission scenario considered, and even if temperatures were to stabilise, mass loss is expected to continue for several decades at least, until glaciers adjust to present-day climate (Marzeion et al., 2014b, 2018; Christian et al., 2018; Hock et al., 2019; Zemp et al., 2019; Roe et al., 2021). In the long-term, however, global climate model experiments show diverging trends for different representative concentration pathways (RCP) emission scenarios. With low-emission scenarios (RCP2.6) the rate of mass loss decreases starting in the second half of the 21st century, but continues to accelerate based on RCP8.5, as disequilibrium between climate and glacier geometry continues to grow (Marzeion et al., 2018, 2020; Hock et al., 2019). Clearly, arctic glaciers, including those in the NCAA, are already strongly out of equilibrium with present-day climate, but the timescales of glacier adjustment and the level of disequilibrium need to be better constrained in order to properly initialise modelling experiments. This will ultimately help reduce uncertainties in projections of future glacier mass change and corresponding sea level rise.

References

Abdalati W, Krabill W, Frederick E, Manizade S, Martin C, Sonntag J, Swift R, Thomas R, Yungel J, Koerner R. 2004. Elevation changes of ice caps in the Canadian Arctic Archipelago. Journal of Geophysical Research: Earth Surface 109:1–11. doi: 10.1029/2003JF000045.

Agisoft. 2020. Agisoft Metashape User Manual: Professional Edition, Version 1.6.

Allen C. 2013. Icebridge MCoRDS L3 gridded ice thickness, surface, and bottom, Version 2. Boulder, Colorado USA. NASA National Snow and Ice Data Center Distributed Active Archive Center. doi:10.5067/YP1PVPR72IHG.

Alley RB. 1991. Sedimentary processes may cause fluctuations of tidewater glaciers. Annals of Glaciology 15:119–124. doi:10.3189/1991AoG15-1-115-121.

Amundson JM, Fahnestock M, Truffer M, Brown J, Lüthi MP, Motyka RJ. 2010. Ice mélange dynamics and implications for terminus stability, Jakobshavn Isbræ, Greenland. Journal of Geophysical Research: Earth Surface 115:F01005. doi: 10.1029/2009JF001405.

Anderson K, Westoby MJ, James MR. 2019. Low-budget topographic surveying comes of age: Structure from motion photogrammetry in geography and the geosciences. Progress in Physical Geography: Earth and Environment 43:163–173. doi:10.1177/0309133319837454.

Bahr DB, Pfeffer WT, Sassolas C, Meier MF. 1998. Response time of glaciers as a function of size and mass balance: 1. Theory. Journal of Geophysical Research: Solid Earth 103:9777–9782. doi:10.1029/98JB00507.

Bahr DB, Radić V. 2012. Significant contribution to total mass from very small glaciers. The Cryosphere 6:763–770. doi: 10.5194/tc-6-763-2012.

Bartholomaus TC, Stearns LA, Sutherland DA, Shroyer EL, Nash JD, Walker RT, Catania G, Felikson D, Carroll D, Fried MJ, Noël BPY, van den Broeke MR. 2016. Contrasts in the response of adjacent fjords and glaciers to ice-sheet surface melt in West Greenland. Annals of Glaciology 57:25–38. doi:10.1017/aog.2016.19.

Bash EA, Moorman BJ, Gunther A. 2018. Detecting short-term surface melt on an arctic glacier using UAV surveys. Remote Sensing 10:1547. doi:10.3390/rs10101547.

Benn DI, Warren CR, Mottram RH. 2007. Calving processes and the dynamics of calving glaciers. Earth Science Reviews 82:143–179. doi:10.1016/j.earscirev.2007.02.002.

Box JE, Colgan WT, Wouters B, Burgess DO, O'Neel S, Thomson LI, Mernild SH. 2018. Global sea-level contribution from arctic land ice: 1971–2017. Environmental Research Letters 13:125012. doi:10.1088/1748-9326/aaf2ed.

Bradley RS, Serreze MC. 1987. Mass balance of two high arctic plateau ice caps. Journal of Glaciology 33:123–128. doi: 10.3189/S0022143000005438.

Braun C, Hardy DR, Bradley RS. 2004. Mass balance and area changes of four high arctic plateau ice caps, 1959–2002. Geografiska Annaler: Series A, Physical Geography 86:43–52. doi:10.1111/j.0435-3676.2004.00212.x.

Brinkerhoff D, Truffer M, Aschwanden A. 2017. Sediment transport drives tidewater glacier periodicity. Nature Communications 8:90. doi:10.1038/s41467-017-00095-5.

Brown D. 1971. Close-range camera calibration. Photogrammetric Engineering 37:855–866.

Burgess D, Sharp MJ. 2008. Recent changes in thickness of the Devon Island ice cap, Canada. Journal of Geophysical Research 113:B07204. doi:10.1029/2007JB005238.

Burgess DO, Danielson BD. 2022. Meighen Ice Cap: changes in geometry, mass, and climatic response since 1959. Canadian Journal of Earth Sciences .

Burgess DO, Sharp MJ. 2004. Recent changes in areal extent of the Devon Ice Cap, Nunavut, Canada. Arctic, Antarctic, and Alpine Research 36:261–271. doi:10.1657/1523-0430(2004)036[0261:RCIAEO]2.0.CO;2.

Carbonneau PE, Dietrich JT. 2017. Cost-effective non-metric photogrammetry from consumer-grade sUAS: implications for direct georeferencing of structure from motion photogrammetry. Earth Surface Processes and Landforms 42:473–486. doi:10.1002/esp.4012.

Carr JR, Vieli A, Stokes CR, Jamieson SSR, Palmer SJ, Christoffersen P, Dowdeswell JA, Nick FM, Blankenship DD, Young DA. 2015. Basal topographic controls on rapid retreat of Humboldt Glacier, northern Greenland. Journal of Glaciology 61:137–150. doi:10.3189/2015JoG14J128.

Cassotto R, Fahnestock M, Amundson JM, Truffer M, Joughin I. 2015. Seasonal and interannual variations in ice mélange and its impact on terminus stability, Jakobshavn Isbræ, Greenland. Journal of Glaciology 61:76–88. doi:10.3189/2015JoG13J235.

Catania GA, Stearns LA, Sutherland DA, Fried MJ, Bartholomaus TC, Morlighem M, Shroyer E, Nash J. 2018. Geometric controls on tidewater glacier retreat in central western Greenland. Journal of Geophysical Research: Earth Surface 123:2024–2038. doi:10.1029/2017JF004499.

Christian JE, Koutnik M, Roe G. 2018. Committed retreat: controls on glacier disequilibrium in a warming climate. Journal of Glaciology 64:675–688. doi:10.1017/jog.2018.57.

Chudley TR, Christoffersen P, Doyle SH, Abellan A, Snooke N. 2019. High-accuracy UAV photogrammetry of ice sheet dynamics with no ground control. The Cryosphere 13:955–968. doi:10.5194/tc-13-955-2019.

Ciracì E, Velicogna I, Swenson S. 2020. Continuity of the mass loss of the world's glaciers and ice caps from the GRACE and GRACE follow-on missions. Geophysical Research Letters 47:e2019GL086926. doi:10.1029/2019gl086926.

Clarke GKC. 1987. Fast glacier flow: Ice streams, surging, and tidewater glaciers. Journal of Geophysical Research: Solid Earth 92:8835–8841. doi:10.1029/JB092iB09p08835.

Cogley JG, Adams WP. 2000. Remote-sensing resources for monitoring glacier fluctuations on Axel Heiberg Island. Arctic 53:248–259. doi:10.14430/arctic856.

Cogley JG, Adams WP, Ecclestone MA. 2011. Half a century of measurements of glaciers on Axel Heiberg Island, Nunavut, Canada. Arctic 64:371–375. doi:10.14430/arctic4127.

Cogley JG, Jung-Rothenhäusler F. 2004. Uncertainty in digital elevation models of Axel Heiberg Island, Arctic Canada. Arctic, Antarctic, and Alpine Research 36:249–260. doi:10.1657/1523-0430(2004)036[0249:UIDEMO]2.0.CO;2.

Colgan W, Rajaram H, Abdalati W, McCutchan C, Mottram R, Moussavi MS, Grigsby S. 2016. Glacier crevasses: Observations, models, and mass balance implications. Reviews of Geophysics 54:119–161. doi:10.1002/2015RG000504.

Collinson RPG. 2011. Introduction to Avionics Systems. 3rd edition. Springer.

Cook AJ, Copland L, Noël BPY, Stokes CR, Bentley MJ, Sharp MJ, Bingham RG, van den Broeke MR. 2019. Atmospheric forcing of rapid marine-terminating glacier retreat in the Canadian Arctic Archipelago. Science Advances 5:eaau8507. doi:10.1126/sciadv.aau8507.

Copland L, Sharp M. 2000. Radio-echo sounding determination of polythermal glacier hydrology. In: DA Noon, GF Stickley, D Longstaff, editors. Eighth International Conference on Ground Penetrating Radar. volume 4084. International Society for Optics and Photonics. SPIE. p. 59–64. doi:10.1117/12.383498.

Copland L, Sharp MJ, Dowdeswell JA. 2003. The distribution and flow characteristics of surge-type glaciers in the Canadian High Arctic. Annals of Glaciology 36:73–81. doi:10.3189/172756403781816301.

Copland L, Sylvestre T, Bishop MP, Shroder JF, Seong YB, Owen LA, Bush A, Kamp U. 2011. Expanded and recently increased glacier surging in the Karakoram. Arctic, Antarctic, and Alpine Research 43:503–516. doi:10.1657/1938-4246-43.4.503.

CReSIS. 2016. Multichannel Coherent Depth Sounder (MCoRDS) L3 Gridded Data. Digital Media http://data.cresis.ku.edu/.

Cuffey KM, Paterson WSB. 2010. The physics of glaciers. Elsevier.

Curley AN, Kochtitzky WH, Edwards BR, Copland L. 2021. Glacier changes over the past 144 years at Alexandra Fiord, Ellesmere Island, Canada. Journal of Glaciology 67:511–522. doi:10.1017/jog.2021.4.

Dalton A, Van Wychen W, Copland L, Gray L, Burgess D. 2022. Seasonal and multiyear flow variability on the Prince of Wales Icefield, Ellesmere Island: 2009–2019. Journal of Geophysical Research: Earth Surface 127:e2021JF006501. doi: 10.1029/2021JF006501.

Dowdeswell JA. 1995. Glaciers in the High Arctic and recent environmental change. Philosophical Transactions: Physical Sciences and Engineering 352:321–334. doi:10.1098/rsta.1995.0073.

Dowdeswell JA, Hamilton GS, Hagen JO. 1991. The duration of the active phase on surge-type glaciers: contrasts between Svalbard and other regions. Journal of Glaciology 37:388–400. doi:10.3189/S0022143000005827.

Eisen O, Harrison WD, Raymond CF. 2001. The surges of Variegated Glacier, Alaska, USA, and their connection to climate and mass balance. Journal of Glaciology 47:351–358. doi:10.3189/172756501781832179.

Eltner A, Kaiser A, Castillo C, Rock G, Neugirg F, Abellán A. 2016. Image-based surface reconstruction in geomorphometry – merits, limits and developments. Earth Surface Dynamics 4:359–389. doi:10.5194/esurf-4-359-2016.

Enderlin EM, Howat IM, Vieli A. 2013. High sensitivity of tidewater outlet glacier dynamics to shape. The Cryosphere 7:1007–1015. doi:10.5194/tc-7-1007-2013.

Farrell JA, Wendel J. 2017. GNSS/INS integration. In: PJG Teunissen, O Montenbruck, editors. Springer Handbook of Global Navigation Satellite Systems. Springer International. p. 811–840.

Fonstad MA, Dietrich JT, Courville BC, Jensen JL, Carbonneau PE. 2013. Topographic structure from motion: a new development in photogrammetric measurement. Earth Surface Processes and Landforms 38:421–430. doi:10.1002/esp.3366.

Fountain AG, Tangborn WV. 1985. The effect of glaciers on streamflow variations. Water Resources Research 21:579–586. doi:10.1029/WR021i004p00579.

Frank T, Åkesson H, de Fleurian B, Morlighem M, Nisancioglu KH. 2022. Geometric controls of tidewater glacier dynamics. The Cryosphere 16:581–601. doi:10.5194/tc-16-581-2022.

Fraser CS. 1997. Digital camera self-calibration. ISPRS Journal of Photogrammetry and Remote Sensing 52:149–159. doi: 10.1016/S0924-2716(97)00005-1.

Fraser CS. 2013. Automatic camera calibration in close range photogrammetry. Photogrammetric Engineering & Remote Sensing 79:381–388. doi:10.14358/PERS.79.4.381.

Furbish DJ, Andrews JT. 1984. The use of hypsometry to indicate long-term stability and response of valley glaciers to changes in mass transfer. Journal of Glaciology 30:199–211. doi:10.3189/S0022143000005931.

Gaffey C, Bhardwaj A. 2020. Applications of unmanned aerial vehicles in cryosphere: Latest advances and prospects. Remote Sensing 12:948. doi:10.3390/rs12060948.

Gardner AS, Moholdt G, Cogley JG, Wouters B, Arendt AA, Wahr J, Berthier E, Hock R, Pfeffer WT, Kaser G, Ligtenberg SRM, Bolch T, Sharp MJ, Hagen JO, van den Broeke MR, Paul F. 2013. A reconciled estimate of glacier contributions to sea level rise: 2003 to 2009. Science 340:852–857. doi:10.1126/science.1234532.

Gardner AS, Moholdt G, Wouters B, Wolken GJ, Burgess DO, Sharp MJ, Cogley JG, Braun C, Labine C. 2011. Sharply increased mass loss from glaciers and ice caps in the Canadian Arctic Archipelago. Nature 473:357–360. doi:10.1038/nature10089.

Gräler B, Pebesma E, Heuvelink G. 2016. Spatio-Temporal Interpolation using gstat. The R Journal 8:204–218.

Granshaw FD, Fountain AG. 2006. Glacier change (1958–1998) in the North Cascades National Park Complex, Washington, USA. Journal of Glaciology 52:251–256. doi:10.3189/172756506781828782.

Gudmundsson GH. 2003. Transmission of basal variability to a glacier surface. Journal of Geophysical Research: Solid Earth 108:2253. doi:10.1029/2002JB002107.

Gudmundsson GH, Krug J, Durand G, Favier L, Gagliardini O. 2012. The stability of grounding lines on retrograde slopes.

The Cryosphere 6:1497–1505. doi:10.5194/tc-6-1497-2012.

Hambrey MJ, Lawson W. 2000. Structural styles and deformation fields in glaciers: a review. Geological Society, London, Special Publications 176:59–83. doi:10.1144/GSL.SP.2000.176.01.06.

Harcourt WD, Palmer SJ, Mansell DT, Le Brocq A, Bartlett O, Gourmelen N, Tepes P, Dowdeswell JA, Blankenship DD, Young DA. 2020. Subglacial controls on dynamic thinning at Trinity-Wykeham Glacier, Prince of Wales Ice Field, Canadian Arctic. International Journal of Remote Sensing 41:1191–1213. doi:10.1080/01431161.2019.1658238.

Hattersley-Smith G. 1969a. Glacial features of Tanquary Fiord and adjoining areas of northern Ellesmere Island, N.W.T. Journal of Glaciology 8:23–50. doi:10.3189/S002214300002075X.

Hattersley-Smith G. 1969b. Recent observations on the surging Otto Glacier, Ellesmere Island. Canadian Journal of Earth Science 6:883–889. doi:10.1139/e69-090.

Hattersley-Smith G, Oliver DR. 1967. Canadian Operation "Hazen-Tanquary", 1965 and 1966. Polar Record 13:607–610. doi:10.1017/S0032247400058186.

Heid T, Kääb A. 2012a. Evaluation of existing image matching methods for deriving glacier surface displacements globally from optical satellite imagery. Remote Sensing of Environment 118:339–355. doi:10.1016/j.rse.2011.11.024.

Heid T, Kääb A. 2012b. Repeat optical satellite images reveal widespread and long term decrease in land-terminating glacier speeds. The Cryosphere 6:467–478. doi:10.5194/tc-6-467-2012.

Hijmans RJ. 2017. raster: Geographic Data Analysis and Modeling. R package version 2.6-7.

Hock R. 2005. Glacier melt: a review of processes and their modelling. Progress in Physical Geography: Earth and Environment 29:362–391. doi:10.1191/0309133305pp453ra.

Hock R, Bliss A, Marzeion B, Giesen RH, Hirabayashi Y, Huss M, Radíc V, Slangen ABA. 2019. GlacierMIP – A model intercomparison of global-scale glacier mass-balance models and projections. Journal of Glaciology 65:453–467. doi:10.1017/jog.2019.22.

Howat IM, Box JE, Ahn Y, Herrington A, McFadden EM. 2010. Seasonal variability in the dynamics of marine-terminating outlet glaciers in Greenland. Journal of Glaciology 56:601–613. doi:10.3189/002214310793146232.

Hudleston PJ. 2015. Structures and fabrics in glacial ice: A review. Journal of Structural Geology 81:1–27. doi:10.1016/j.jsg.2015.09.003.

Hugentobler U, Montenbruck O. 2017. Satellite orbits and attitude. In: PJG Teunissen, O Montenbruck, editors. Springer Handbook of Global Navigation Satellite Systems. Springer International. p. 59–90.

Hugonnet R, McNabb R, Berthier E, Menounos B, Nuth C, Girod L, Farinotti D, Huss M, Dussaillant I, Brun F, Kääb A. 2021. Accelerated global glacier mass loss in the early twenty-first century. Nature 592:726–731. doi:10.1038/s41586-021-03436-z.

Huss M. 2013. Density assumptions for converting geodetic glacier volume change to mass change. The Cryosphere 7:877–887. doi:10.5194/tc-7-877-2013.

Immerzeel W, Kraaijenbrink P, Shea J, Shrestha A, Pellicciotti F, Bierkens M, de Jong S. 2014. High-resolution monitoring of Himalayan glacier dynamics using unmanned aerial vehicles. Remote Sensing of Environment 150:93–103. doi:10.1016/j.rse.2014.04.025.

IPCC. 2022. The ocean and cryosphere in a changing climate: Special report of the Intergovernmental Panel on Climate Change. Cambridge University Press. doi:10.1017/9781009157964.

James MR, Chandler JH, Eltner A, Fraser C, Miller PE, Mills JP, Noble T, Robson S, Lane SN. 2019. Guidelines on the use of structure-from-motion photogrammetry in geomorphic research. Earth Surface Processes and Landforms 44:2081–2084. doi:10.1002/esp.4637.

James MR, Robson S. 2014. Mitigating systematic error in topographic models derived from UAV and ground-based image networks. Earth Surface Processes and Landforms 39:1413–1420. doi:10.1002/esp.3609.

Jamieson SSR, Vieli A, Livingstone SJ, Cofaigh CÓ, Stokes C, Hillenbrand CD, Dowdeswell JA. 2012. Ice-stream stability on a reverse bed slope. Nature Geoscience 5:799. doi:10.1038/ngeo1600.

Jezek K, Wu X, Paden J, Leuschen C. 2013. Radar mapping of Isunnguata Sermia, Greenland. Journal of Glaciology 59:1135–1146. doi:10.3189/2013JoG12J248.

Jouvet G, Weidmann Y, Seguinot J, Funk M, Abe T, Sakakibara D, Seddik H, Sugiyama S. 2017. Initiation of a major calving event on the Bowdoin Glacier captured by UAV photogrammetry. The Cryosphere 11:911–921. doi:10.5194/tc-11-911-2017.

Jouvet G, Weidmann Y, van Dongen E, Lüthi MP, Vieli A, Ryan JC. 2019. High-endurance UAV for monitoring calving glaciers: Application to the Inglefield Bredning and Eqip Sermia, Greenland. Frontiers in Earth Science 7. doi:10.3389/feart.2019.00206.

Jóhannesson T, Raymond C, Waddington E. 1989. Time–scale for adjustment of glaciers to changes in mass balance. Journal of Glaciology 35:355–369. doi:10.3189/S002214300000928X.

Kääb A, Vollmer M. 2000. Surface geometry, thickness changes and flow fields on creeping mountain permafrost: automatic extraction by digital image analysis. Permafrost and Periglacial Processes 11:315–326. doi:10.1002/1099-1530(200012)11:4<315::AID-PPP365>3.0.CO;2-J.

Kamb B, Raymond CF, Harrison WD, Engelhardt H, Echelmeyer KA, Humphrey N, Brugman MM, Pfeffer T. 1985. Glacier surge mechanism: 1982-1983 surge of Variegated Glacier, Alaska. Science 227:469–479. doi:10.1126/science.227.4686.469.

Kochtitzky W, Copland L. 2022. Retreat of Northern Hemisphere marine-terminating glaciers, 2000–2020. Geophysical Research Letters 49:e2021GL096501. doi:10.1029/2021GL096501.

Koerner RM. 1977. Devon Island ice cap: core stratigraphy and paleoclimate. Science 196:15–18. doi:10.1126/science.196.4285.15.

Koerner RM. 1979. Accumulation, ablation, and oxygen isotope variations on the Queen Elizabeth Islands ice caps, Canada. Journal of Glaciology 22:25–41. doi:10.3189/S0022143000014039.

Koerner RM. 2005. Mass balance of glaciers in the Queen Elizabeth Islands, Nunavut, Canada. Annals of Glaciology 42:417–423. doi:10.3189/172756405781813122.

Kouba J, Héroux P. 2001. Precise Point Positioning using IGS orbit and clock products. GPS Solutions 5:12–28.

Kouba J, Lahaye F, Tétreault P. 2017. Precise point positioning. In: PJG Teunissen, O Montenbruck, editors. Springer Handbook of Global Navigation Satellite Systems. Springer International. p. 723–751.

Koyama T. 2006. Optics in digital still cameras. In: J Nakamura, editor. Image sensors and signal processing for digital still cameras. CRC Press. p. 21–51.

Kraaijenbrink P, Shea J, Pellicciotti F, de Jong S, Immerzeel W. 2016. Object-based analysis of unmanned aerial vehicle imagery to map and characterise surface features on a debris-covered glacier. Remote Sensing of Environment 186:581–595. doi:10.1016/j.rse.2016.09.013.

Kraaijenbrink PDA, Shea JM, Litt M, Steiner JF, Treichler D, Koch I, Immerzeel WW. 2018. Mapping surface temperatures on a debris-covered glacier with an unmanned aerial vehicle. Frontiers in Earth Science 6. doi:10.3389/feart.2018.00064.

Krug J, Durand G, Gagliardini O, Weiss J. 2015. Modelling the impact of submarine frontal melting and ice mélange on glacier dynamics. The Cryosphere 9:989–1003. doi:10.5194/tc-9-989-2015.

Lague D, Brodu N, Leroux J. 2013. Accurate 3D comparison of complex topography with terrestrial laser scanner: Application to the Rangitikei canyon (N-Z). ISPRS Journal of Photogrammetry and Remote Sensing 82:10–26. doi:10.1016/j.isprsjprs.2013.04.009.

Langley RB, Teunissen PJG, Montenbruck O. 2017. Introduction to GNSS. In: PJG Teunissen, O Montenbruck, editors. Springer Handbook of Global Navigation Satellite Systems. Springer International. p. 3–23.

Lawson WJ, Sharp MJ, Hambrey MJ. 1994. The structural geology of a surge-type glacier. Journal of Structural Geology 16:1447–1462. doi:10.1016/0191-8141(94)90008-6.

Leclercq PW, Oerlemans J. 2012. Global and hemispheric temperature reconstruction from glacier length fluctuations. Climate Dynamics 38:1065–1079. doi:10.1007/s00382-011-1145-7.

Leick A, Rapoport L, Tatarnikov D. 2015. GPS Satellite Surveying. 4th edition. John Wiley & Sons.

Lenaerts JTM, van Angelen JH, van den Broeke MR, Gardner AS, Wouters B, van Meijgaard E. 2013. Irreversible mass loss of Canadian Arctic Archipelago glaciers. Geophysical Research Letters 40:870–874. doi:10.1002/grl.50214.

Lowe DG. 1999. Object recognition from local scale-invariant features. In: Proceedings of the Seventh IEEE International Conference on Computer Vision. volume 2. p. 1150–1157. doi:10.1109/ICCV.1999.790410.

Lowe DG. 2004. Distinctive image features from scale-invariant keypoints. International Journal of Computer Vision 60:91–110. doi:10.1023/B:VISI.0000029664.99615.94.

Mano MM, Ciletti MD. 2013. Digital design. 5th edition. Pearson.

Marzeion B, Cogley JG, Richter K, Parkes D. 2014a. Attribution of global glacier mass loss to anthropogenic and natural causes. Science 345:919–921. doi:10.1126/science.1254702.

Marzeion B, Hock R, Anderson B, Bliss A, Champollion N, Fujita K, Huss M, Immerzeel WW, Kraaijenbrink P, Malles JH, Maussion F, Radić V, Rounce DR, Sakai A, Shannon S, van de Wal R, Zekollari H. 2020. Partitioning the uncertainty of ensemble projections of global glacier mass change. Earth's Future 8:e2019EF001470. doi:10.1029/2019EF001470.

Marzeion B, Jarosch AH, Gregory JM. 2014b. Feedbacks and mechanisms affecting the global sensitivity of glaciers to climate change. The Cryosphere 8:59–71. doi:10.5194/tc-8-59-2014.

Marzeion B, Kaser G, Maussion F, Champollion N. 2018. Limited influence of climate change mitigation on short-term glacier mass loss. Nature Climate Change 8:305–308. doi:10.1038/s41558-018-0093-1.

Meier MF, Post A. 1969. What are glacier surges? Canadian Journal of Earth Science 6:807–817. doi:10.1139/e69-081.

Meier MF, Post A. 1987. Fast tidewater glaciers. Journal of Geophysical Research: Solid Earth 92:9051–9058. doi:10.1029/JB092iB09p09051.

Millan R, Mouginot J, Rignot E. 2017. Mass budget of the glaciers and ice caps of the Queen Elizabeth Islands, Canada, from 1991 to 2015. Environmental Research Letters 12:024016. doi:10.1088/1748-9326/aa5b04.

Miller GH, Bradley RS, Andrews JT. 1975. The glaciation level and lowest equilibrium line altitude in the High Canadian Arctic: Maps and climatic interpretation. Arctic and Alpine Research 7:155–168. doi:10.1080/00040851.1975.12003819.

Mortimer CA, Sharp M, Van Wychen W. 2018. Influence of recent warming and ice dynamics on glacier surface elevations in the Canadian High Arctic, 1995–2014. Journal of Glaciology 64:450–464. doi:10.1017/jog.2018.37.

Mortimer CA, Sharp M, Wouters B. 2016. Glacier surface temperatures in the Canadian High Arctic, 2000–15. Journal of Glaciology 62:963–975. doi:0.1017/jog.2016.80.

Mosbrucker AR, Major JJ, Spicer KR, Pitlick J. 2017. Camera system considerations for geomorphic applications of SfM photogrammetry. Earth Surface Processes and Landforms 42:969–986. doi:10.1002/esp.4066.

Müller F. 1969. Was the Good Friday Glacier on Axel Heiberg Island surging? Canadian Journal of Earth Science 6:891–894. doi:10.1139/e69-091.

Murray T, Dowdeswell JA, Drewry DJ, Frearson I. 1998. Geometric evolution and ice dynamics during a surge of Bakaninbreen, Svalbard. Journal of Glaciology 44:263–272. doi:10.3189/S0022143000002604.

Murray T, Strozzi T, Luckman A, Jiskoot H, Christakos P. 2003. Is there a single surge mechanism? Contrasts in dynamics between glacier surges in Svalbard and other regions. Journal of Geophysical Research: Solid Earth 108:2237. doi:10.1029/2009JF001405.

Mölg N, Bolch T. 2017. Structure-from-Motion using historical aerial images to analyse changes in glacier surface elevation. Remote Sensing 9:1021. doi:10.3390/rs9101021.

Nakamura J. 2006. Basics of image sensors. In: J Nakamura, editor. Image sensors and signal processing for digital still cameras. CRC Press. p. 53–93.

Narod BB, Clarke GKC. 1994. Miniature high-power impulse transmitter for radio-echo sounding. Journal of Glaciology 40:190–194. doi:10.3189/S002214300000397X.

National Geospatial Intelligence Agency. 2019. The American Practical Navigator: An Epitome of Navigation. US National Geospatial Intelligence Agency.

Nesbit PR, Hugenholtz CH. 2019. Enhancing UAV–SfM 3D model accuracy in high-relief landscapes by incorporating oblique images. Remote Sensing 11:239. doi:10.3390/rs11030239.

Nick FM, Vieli A, Howat IM, Joughin I. 2009. Large-scale changes in Greenland outlet glacier dynamics triggered at the terminus. Nature Geoscience 2:110. doi:10.1038/ngeo394.

Noh MJ, Howat IM. 2015. Automated stereo-photogrammetric DEM generation at high latitudes: Surface Extraction with TIN-based Search-space Minimization (SETSM) validation and demonstration over glaciated regions. GIScience & Remote Sensing 52:198–217. doi:10.1080/15481603.2015.1008621.

Nolan M, Larsen C, Sturm M. 2015. Mapping snow depth from manned aircraft on landscape scales at centimeter resolution using structure-from-motion photogrammetry. The Cryosphere 9:1445–1463. doi:10.5194/tc-9-1445-2015.

Noël B. 2017. Average surface mass balance (SMB) components at 1 km for the Canadian Arctic Archipelago (1958–1995 and 1996–2015), links to RACMO2.3 model results in NetCDF format. Digital Media https://doi.org/10.1594/PANGAEA.881315. doi:10.1594/PANGAEA.881315.

Noël B, van de Berg WJ, Lhermitte S, Wouters B, Schaffer N, van den Broeke MR. 2018. Six decades of glacial mass loss in the Canadian Arctic Archipelago. Journal of Geophysical Research: Earth Surface 123:1430–1449. doi:10.1029/2017JF004304.

Oerlemans J. 2005. Extracting a climate signal from 169 glacier records. Science 308:675–677. doi:10.1126/science.1107046.

Oerlemans J, Anderson B, Hubbard A, Huybrechts P, Jóhannesson T, Knap WH, Schmeits M, Stroven AP, van de Wal RSW, Wallinga J, Zuo Z. 1998. Modelling the response of glaciers to climate warming. Climate Dynamics 14:267–274. doi:10.1007/s003820050222.

Ohta J. 2020. Smart CMOS Image Sensors and Applications. 2nd edition. Taylor & Francis. doi:10.1201/9781315156255.

Ommanney CSL. 1969. A study in glacier inventory: The ice masses of Axel Heiberg Island, Canadian Arctic Archipelago. Axel Heiberg Island Research Reports: Glaciology No. 3. McGill University, Montréal.

Paden J, Akins T, Dunson D, Allen C, Gogineni P. 2010. Ice-sheet bed 3-D tomography. Journal of Glaciology 56:3–11. doi:10.3189/002214310791190811.

Palum R. 2009. Optical antialiasing filters. In: R Lukac, editor. Single-sensor imaging: Methods and applications for digital cameras. Taylor & Francis. p. 105–135. doi:10.1201/9781315219363.

Parkes D, Marzeion B. 2018. Twentieth-century contribution to sea-level rise from uncharted glaciers. Nature 563:551–554. doi:10.1038/s41586-018-0687-9.

Paul F, Barrand NE, Baumann S, Berthier E, Bolch T, Casey K, Frey H, Joshi S, Konovalov V, Le Bris R, Molg N, Nosenko G, Nuth C, Pope A, Racoviteanu A, Rastner P, Raup B, Scharrer K, Steffen S, Winsvold S. 2013. On the accuracy of glacier outlines derived from remote-sensing data. Annals of Glaciology 54:171–182. doi:10.3189/2013AoG63A296.

Paul F, Bolch T, Kääb A, Nagler T, Nuth C, Scharrer K, Shepherd A, Strozzi T, Ticconi F, Bhambri R, Berthier E, Bevan S, Gourmelen N, Heid T, Jeong S, Kunz M, Lauknes TR, Luckman A, Merryman Boncori JP, Moholdt G, Muir A, Neelmeijer J, Rankl M, Van Looy J, Van Niel T. 2015. The glaciers climate change initiative: Methods for creating glacier area, elevation change and velocity products. Remote Sensing of Environment 162:408–426. doi:10.1016/j.rse.2013.07.043.

Pfeffer WT. 2007. A simple mechanism for irreversible tidewater glacier retreat. Journal of Geophysical Research: Earth Surface 112:F03011. doi:10.1029/2006JF000590.

Porter C, Morin P, Howat I, Noh MJ, Bates B, Peterman K, Keesey S, Schlenk M, Gardiner J, Tomko K, Willis M, Kelleher C, Cloutier M, Husby E, Foga S, Nakamura H, Platson M, Wethington J Michael, Williamson C, Bauer G, Enos J, Arnold G, Kramer W, Becker P, Doshi A, D'Souza C, Cummens P, Laurier F, Bojesen M. 2018. ArcticDEM. Digital Media https://doi.org/10.7910/DVN/OHHUKH.

QGIS Development Team. 2017. QGIS Geographic Information System. Open Source Geospatial Foundation Project http://qgis.osgeo.org.

R Core Team. 2017. R: A Language and Environment for Statistical Computing. R Foundation for Statistical Computing, Vienna, Austria https://www.R-project.org/.

Raper SCB, Braithwaite RJ. 2009. Glacier volume response time and its links to climate and topography based on a conceptual model of glacier hypsometry. The Cryosphere 3:183–194. doi:10.5194/tc-3-183-2009.

Ray SF. 2002. Applied Photographic Optics: Lenses and optical systems for photography, film, video, electronic and digital imaging. 3rd edition. Focal Press: Elsevier Science. doi:10.4324/9780080499253.

Raymond CF. 1987. How do glaciers surge? A review. Journal of Geophysical Research: Solid Earth 92:9121–9134. doi: 10.1029/JB092iB09p09121.

Raymond MJ, Gudmundsson GH. 2005. On the relationship between surface and basal properties on glaciers, ice sheets, and ice streams. Journal of Geophysical Research: Solid Earth 110:B08411. doi:10.1029/2005JB003681.

RGI Consortium. 2017. Randolph Glacier Inventory – A dataset of global glacier outlines: Version 6.0. GLIMS Technical Report. Boulder, Colorado, USA: NSIDC: National Snow and Ice Data Center. doi:10.7265/4m1f-gd79.

Rippin DM, Pomfret A, King N. 2015. High resolution mapping of supra-glacial drainage pathways reveals link between micro-channel drainage density, surface roughness and surface reflectance. Earth Surface Processes and Landforms 40:1279–1290. doi:10.1002/esp.3719.

Roe GH, Baker MB, Herla F. 2017. Centennial glacier retreat as categorical evidence of regional climate change. Nature Geoscience 10:95–99. doi:10.1038/ngeo2863.

Roe GH, Christian JE, Marzeion B. 2021. On the attribution of industrial-era glacier mass loss to anthropogenic climate change. The Cryosphere 15:1889–1905. doi:10.5194/tc-15-1889-2021.

Rowlands A. 2017. Physics of Digital Photography. 2053–2563. IOP Publishing. doi:10.1088/978-0-7503-1242-4.

Ryan JC, Hubbard AL, Box JE, Todd J, Christoffersen P, Carr JR, Holt TO, Snooke N. 2015. UAV photogrammetry and structure from motion to assess calving dynamics at Store Glacier, a large outlet draining the Greenland ice sheet. The Cryosphere 9:1–11. doi:10.5194/tc-9-1-2015.

Sanz-Ablanedo E, Chandler JH, Wackrow R. 2012. Parameterising internal camera geometry with focusing distance. The Photogrammetric Record 27:210–226. doi:10.1111/j.1477-9730.2012.00677.x.

Schaffer N, Copland L, Zdanowicz C. 2017. Ice velocity changes on Penny Ice Cap, Baffin Island, since the 1950s. Journal of Glaciology 63:716–730. doi:10.1017/jog.2017.40.

Schellenberger T, Van Wychen W, Copland L, Kääb A, Gray L. 2016. An inter-comparison of techniques for determining velocities of maritime Arctic glaciers, Svalbard, using Radarsat-2 Wide Fine mode data. Remote Sensing 8:785. doi: 10.3390/rs8090785.

Sergienko O. 2012. The effects of transverse bed topography variations in ice-flow models. Journal of Geophysical Research: Earth Surface 117:F03011. doi:10.1029/2011JF002203.

Serreze MC, Raup B, Braun C, Hardy DR, Bradley RS. 2017. Rapid wastage of the Hazen Plateau ice caps, northeastern Ellesmere Island, Nunavut, Canada. The Cryosphere 11:169–177. doi:10.5194/tc-11-169-2017.

Sevestre H, Benn DI. 2015. Climatic and geometric controls on the global distribution of surge-type glaciers: implications for a unifying model of surging. Journal of Glaciology 61:646–662. doi:10.3189/2015JoG14J136.

Sevestre H, Benn DI, Luckman A, Nuth C, Kohler J, Lindbäck K, Pettersson R. 2018. Tidewater glacier surges initiated at the terminus. Journal of Geophysical Research: Earth Surface 123:1035–1051. doi:10.1029/2017JF004358.

Shannon RR. 1995. Optical specifications. In: M Bass, EW van Stryland, DR Williams, WL Wolfe, editors. Handbook of Optics Volume 1: Fundamentals, Techniques, and Design. McGraw-Hill. p. 35.1–35.12. doi:10.1201/9781315219363.

Sharp M, Burgess DO, Cawkwell F, Copland L, Davis JA, Dowdeswell EK, Dowdeswell JA, Gardner AS, Mair D, Wang L, Williamson SN, Wolken GJ, Wyatt F. 2014. Remote sensing of recent glacier changes in the Canadian Arctic. In: JS Kargel, GJ Leonard, MP Bishop, A Kääb, BH Raup, editors. Global Land Ice Measurements from Space. Springer Berlin Heidelberg. p. 205–228. doi:10.1007/978-3-540-79818-7_9.

Sharp M, Burgess DO, Cogley JG, Ecclestone M, Labine C, Wolken GJ. 2011. Extreme melt on Canada's Arctic ice caps in the 21st century. Geophysical Research Letters 38:1–5. doi:10.1029/2011GL047381.

Short NH, Gray AL. 2005. Glacier dynamics in the Canadian High Arctic from RADARSAT-1 speckle tracking. Canadian

Journal of Remote Sensing 31:225–239. doi:10.5589/m05-010.

Smith M, Carrivick J, Quincey D. 2016a. Structure from motion photogrammetry in physical geography. Progress in Physical Geography: Earth and Environment 40:247–275. doi:10.1177/0309133315615805.

Smith MW, Quincey DJ, Dixon T, Bingham RG, Carrivick JL, Irvine-Fynn TDL, Rippin DM. 2016b. Aerodynamic roughness of glacial ice surfaces derived from high-resolution topographic data. Journal of Geophysical Research: Earth Surface 121:748–766. doi:10.1002/2015JF003759.

Straneo F, Heimbach P, Sergienko O, Hamilton G, Catania G, Griffies S, Hallberg R, Jenkins A, Joughin I, Motyka R, Pfeffer WT, Price SF, Rignot E, Scambos T, Truffer M, Vieli A. 2013. Challenges to understanding the dynamic response of Greenland's marine terminating glaciers to oceanic and atmospheric forcing. Bulletin of the American Meteorological Society 94:1131–1144. doi:10.1175/BAMS-D-12-00100.1.

Strozzi T, Paul F, Wiesmann A, Schellenberger T, Kääb A. 2017. Circum-Arctic changes in the flow of glaciers and ice caps from satellite SAR data between the 1990s and 2017. Remote Sensing 9:947. doi:10.3390/rs9090947.

Szeliski R. 2011. Computer Vision: Algorithms and Applications. Springer-Verlag. doi:10.1007/978-1-84882-935-0.

Thomson L, Copland L. 2016. White glacier 2014, axel heiberg island, nunavut: mapped using structure from motion methods. Journal of Maps 12:1063–1071. doi:10.1080/17445647.2015.1124057.

Thomson LI, Copland L. 2017. Multi-decadal reduction in glacier velocities and mechanisms driving deceleration at polythermal White Glacier, Arctic Canada .

Thomson LI, Osinski GR, Ommanney CSL. 2011. Glacier change on Axel Heiberg Island, Nunavut, Canada. Journal of Glaciology 57:1079–1086. doi:10.3189/002214311798843287.

Thomson LI, Zemp M, Copland L, Cogley JG, Ecclestone MA. 2017. Comparison of geodetic and glaciological mass budgets for White Glacier, Axel Heiberg Island, Canada .

Trimble. 2009. Trimble R7 GNSS and R5 GPS Receivers: User Guide.

Turrin JB, Forster RR, Sauber JM, Hall DK, Bruhn RL. 2014. Effects of bedrock lithology and subglacial till on the motion of Ruth Glacier, Alaska, deduced from five pulses from 1973 to 2012. Journal of Glaciology 60:771–781. doi:10.3189/2014JoG13J182.

Van Wychen W, Burgess D, Kochtitzky W, Nikolic N, Copland L, Gray L. 2021. RADARSAT-2 derived glacier velocities and dynamic discharge estimates for the Canadian High Arctic: 2015–2020. Canadian Journal of Remote Sensing 46:695–714. doi:10.1080/07038992.2020.1859359.

Van Wychen W, Burgess DO, Gray L, Copland L, Sharp M, Dowdeswell JA, Benham TJ. 2014. Glacier velocities and dynamic ice discharge from the Queen Elizabeth Islands, Nunavut, Canada. Geophysical Research Letters 41:484–490. doi:10.1002/2013GL058558.

Van Wychen W, Davis J, Burgess DO, Copland L, Gray L, Sharp M, Mortimer C. 2016. Characterizing interannual variability of glacier dynamics and dynamic discharge (1999–2015) for the ice masses of Ellesmere and Axel Heiberg Islands, Nunavut, Canada. Journal of Geophysical Research: Earth Surface 121:39–63. doi:10.1002/2015JF003708.

Walter JI, Box JE, Tulaczyk S, Brodsky EE, Howat IM, Ahn Y, Brown A. 2012. Oceanic mechanical forcing of a marine-terminating Greenland glacier. Annals of Glaciology 53:181–192. doi:10.3189/2012AoG60A083.

Westoby M, Brasington J, Glasser N, Hambrey M, Reynolds J. 2012. 'Structure-from-Motion' photogrammetry: A low-cost, effective tool for geoscience applications. Geomorphology 179:300–314. doi:10.1016/j.geomorph.2012.08.021.

WGMS. 2021. Global Glacier Change Bulletin No. 4 (2018–2019). Zemp M, Nussbaumer SU, Gärtner-Roer I, Bannwart J, Paul F, Hoelzle M, editors, ISC(WDS)/IUGG(IACS)/UNEP/UNESCO/WMO, World Glacier Monitoring Service, Zurich, Switzerland, 278 pp. Based on database version: doi:10.5904/wgms-fog-2021-05.

White A, Copland L. 2018. Area change of glaciers across Northern Ellesmere Island, Nunavut, between ∼1999 and ∼2015. Journal of Glaciology 64:609–623. doi:10.1017/jog.2018.49.

White A, Copland L. 2019. Loss of floating glacier tongues from the Yelverton Bay region, Ellesmere Island, Canada. Journal of Glaciology 65:376–394. doi:10.1017/jog.2019.15.

White A, Copland L, Mueller D, Van Wychen W. 2015. Assessment of historical changes (1959–2012) and the causes of recent break-ups of the Petersen ice shelf, Nunavut, Canada. Annals of Glaciology 56:65–76. doi:10.3189/2015AoG69A687.

Wolken GJ, England JH, Dyke AS. 2008. Changes in late-Neoglacial perennial snow/ice extent and equilibrium-line altitudes in the Queen Elizabeth Islands, Arctic Canada. The Holocene 18:615–627. doi:10.1177/0959683608089215.

Wu X, Jezek KC, Rodriguez E, Gogineni S, Rodriguez-Morales F, Freeman A. 2011. Ice sheet bed mapping with airborne SAR tomography. IEEE Transactions Geoscience and Remote Sensing 49:3791–3802. doi:10.1109/TGRS.2011.2132802.

Yoshida H. 2006. Evaluation of image quality. In: J Nakamura, editor. Image sensors and signal processing for digital still cameras. CRC Press. p. 277–303.

Zemp M, Frey H, Gärtner-Roer I, Nussbaumer SU, Hoelzle M, Paul F, Haeberli W, Denzinger F, Ahlstrøm AP, Anderson B, Bajracharya S, Baroni C, Braun LN, Cáceres BE, Casassa G, Cobos G, Dávila LR, Delgado Granados H, Demuth MN, Espizua L, Fischer A, Fujita K, Gadek B, Ghazanfar A, Hagen JO, Holmlund P, Karimi N, Li Z, Pelto M, Pitte P, Popovnin VV, Portocarrero CA, Prinz R, Sangewar CV, Severskiy I, Sigurđsson A Oddur Soruco, Usubaliev R, Vincent C. 2015. Historically unprecedented global glacier decline in the early 21st century. Journal of Glaciology 61:745–762. doi:10.3189/2015JoG15J017.

Zemp M, Huss M, Thibert E, Eckert N, McNabb R, Huber J, Barandun M, Machguth H, Nussbaumer SU, Gärtner-Roer I, Thomson L, Paul F, Maussion F, Kutuzov S, G CJ. 2019. Global glacier mass changes and their contributions to sea-level rise from 1961 to 2016. Nature 568:382–386. doi:10.1038/s41586-019-1071-0.